

OPTICAL PROPERTIES OF ULTRA-THIN MATERIALS

**A Thesis Submitted to
the Graduate School of Engineering and Sciences of
İzmir Institute of Technology
in Partial Fulfillment of the Requirements for the Degree of**

DOCTOR OF PHILOSOPHY

in Physics

**by
Cihan BACAŞIZ**

**July 2017
İZMİR**

We approve the thesis of **Cihan BACAKSIZ**

Examining Committee Members:

Prof. Dr. R. Tuğrul SENGER

Department of Physics, İzmir Institute of Technology

Assoc. Prof. Dr. Hâldun SEVİNÇLİ

Department of Materials Science and Engineering, İzmir Institute of Technology

Assoc. Prof. Dr. A. Devrim GÜÇLÜ

Department of Physics, İzmir Institute of Technology

Prof. Dr. Hamza POLAT

Department of Physics, Dokuz Eylül University

Assoc. Prof. Dr. Engin DURGUN

Department of Materials Science and Nanotechnology, Bilkent University

27 July 2017

Prof. Dr. R. Tuğrul SENGER

Supervisor, Department of Physics
İzmir Institute of Technology

Assoc. Prof. Dr. Hasan ŞAHİN

Co-Supervisor, Department of Photonics
İzmir Institute of Technology

Prof. Dr. R. Tuğrul SENGER

Head of the Department of
Physics

Prof. Dr. Aysun SOFUOĞLU

Dean of the Graduate School of
Engineering and Sciences

ACKNOWLEDGMENTS

First of all, I would like to thank my supervisor Prof. Dr. R. Tuğrul SENGER for his patient instruction, generous help and support in my studies and this thesis work.

I would like to thank my co-supervisor Assoc. Prof. Dr. Hasan ŞAHİN for his great guidance and unique assistance.

I would also like to thank my colleagues Mehmet Yağmorcukardeş and Fadıl İyikanat for their friendship and contributions during my Ph.D. studies.

Finally and most importantly, I would like to thank my lovely wife Selma Mayda Bacaksız for everything she has done for me.

This research was supported by TUBITAK with 111T318 and 114F397 project numbers.

ABSTRACT

OPTICAL PROPERTIES OF ULTRA-THIN MATERIALS

Many years of research effort, after the synthesis of graphene, have revealed that atomically thin two-dimensional materials have mechanical, electronic, and optical properties which are different from their bulk counterparts. Thus, the interest in two-dimensional materials is growing which is also fueled by fast advances in synthesis and measurement techniques. In this regard, the theoretical and computational simulations provide physical insight to the experiments in this new and demanded field; a tool for characterizing these materials; and also a reliable prediction approach to possible stable structures. The density functional theory (DFT) is one of the most powerful and commonly used methods for such theoretical investigations. The DFT-based computational determination of optical properties, as compared to other usual DFT-based calculations, is in its early stage due to high computational resource requirements and lack of established documentation. Therefore, the present thesis aims at giving the methodology and computing the optical properties of ultra-thin materials by using DFT and beyond-DFT approaches. More precisely, the thesis provides an overview of light matter interaction; basics of DFT, GW approximation for many-body effects, Bethe-Salpeter equation for excitonic effects; and several applications of these on atomically-thin systems.

ÖZET

ULTRA-İNCE MALZEMELERİN OPTİK ÖZELLİKLERİ

Grafen'in sentezlenmesinden sonra, yılar süren araştırma gayreti ortaya çıkardı ki atom inceliğinde iki-boyutlu malzemeler yığın durmunlarından farklı mekanik, elektronik ve optik özellikler göstermektedir. Dolayısıyla, iki boyutlu malzemelere olan, ölçüm ve sentezleme tekniklerindeki gelişmelerle de desteklenen, ilgi giderek artmaktadır. Bu bakımdan, teorik ve hesaplamalı simülasyonlar, deneysel gözlemlerin fiziksel içyüzünü anlamak, malzemeleri tanımlamak ve de olası yapıların güvenilir bir biçimde öngörülebilmesi için uygun bir platform sunmaktadır. Yoğunluk fonksiyoneli teorisi bu yardımı hakkıyla verebilen ve sıklıkla kullanılan bir metottur. Fakat basit yoğunluk fonksiyoneli hesaplarına kıyasla, optik özelliklerin hesaplanması yazılı kaynak yetersizliği ve hesaplama için yüksek özellikli bilgisayar gereksinimi yüzünden, daha başlangıç seviyesindedir. Halihazırdaki tez, bu sebeplerden ötürü, ultra-ince malzemelerin yoğunluk fonksiyoneli teorisi tabanlı hesaplamalarla ve ötesi yaklaşımlar kullanılarak, optik özelliklerinin belirlenmesinin metodunu vermeyi amaçlamaktadır. Daha net söylemek gerekirse, bu tez, ışık-madde etkileşimine genel teorik bir bakışla beraber, yoğunluk fonksiyoneli teorisinin, çok-parçacık etkileri için GW yaklaşımının ve eksitonik etkiler için Bethe-Salpeter denkleminin temellerini ve bunların detaylı uygulamalarını çeşitli çalışmalar içinde sunmaktadır.

... to my lovely wife ...

TABLE OF CONTENTS

LIST OF FIGURES	x
LIST OF TABLES	xvii
CHAPTER 1. INTRODUCTION	1
CHAPTER 2. THEORETICAL BACKGROUND AND METHODOLOGY	10
2.1. Light-Matter Interaction	10
2.1.1. Electromagnetic Waves in a Material	10
2.1.2. The Complex Refractive Index and Dielectric Function	13
2.1.3. Absorption	16
2.1.4. Exciton	18
2.1.5. Light Emission	19
2.1.6. Optical Measurements	19
2.2. Density Functional Theory	20
2.2.1. Hohenberg-Kohn Theorems	21
2.2.2. Hellmann-Feynman Theorem	22
2.2.3. Kohn-Sham Ansatz	22
2.2.4. Functionals of Exchange and Correlations	23
2.3. Many Body Effects and Excited States	24
2.3.1. Quasiparticle Energies	25
2.3.2. Excitonic States	26
2.4. Computational Methodology	27
CHAPTER 3. TESTS	29
3.1. Computational Resource Tests	29
3.2. Qualitative Tests for Parameters	32
3.2.1. Effect of k -point sampling	32
3.2.2. Effect of vacuum spacing	33
3.2.3. Effect of energy cut-off	34
CHAPTER 4. HEXAGONAL AIN	37

4.1. Structures of Bulk AlN.....	39
4.2. Monolayer, Bilayer and Few Layer <i>h</i> -AlN.....	41
4.3. Conclusions.....	46
CHAPTER 5. HYDROGENATION OF SINGLE LAYER PbI ₂	48
5.1. H and T Phases of Single Layer PbI ₂	49
5.2. Interaction with Single Hydrogen	51
5.3. One-side Hydrogenation	52
5.4. Full Hydrogenation.....	55
5.5. Conclusions.....	56
CHAPTER 6. ANISOTROPIC AND FLEXIBLE ULTRA-THIN ZnSe	58
6.1. Structural and Electronic Properties	58
6.2. Mechanical Properties.....	61
6.3. Conclusions.....	64
CHAPTER 7. ULTRA-THIN SnS ₂	65
7.1. Computational Details	66
7.2. H and T Phases of Single Layer SnS ₂	67
7.3. Bilayer SnS ₂	69
7.4. Conclusions.....	77
CHAPTER 8. OPTICAL PROPERTIES OF <i>h</i> -AlN	79
8.1. Computational Details	81
8.2. Results and Discussion.....	83
8.3. Conclusions.....	91
CHAPTER 9. <i>h</i> -AlN-Mg(OH) ₂ vdW BILAYER HETEROSTRUCTURE	93
9.1. Computational Details	95
9.1.1. Convergence Tests.....	96
9.1.2. Methodology for Determination of Excitonic Wave Functions .	97
9.2. Single Layer <i>h</i> -AlN and Mg(OH) ₂	99
9.3. Bilayer Heterostructure	100
9.4. Conclusions.....	104

CHAPTER 10. CONCLUSION	106
REFERENCES	108

LIST OF FIGURES

<u>Figure</u>	<u>Page</u>
Figure 1.1. (a) Photograph of a 50- μm aperture partially covered by graphene and its bilayer. (b) Transmittance spectrum of single-layer graphene (open circles) and theoretically predicted results for two-dimensional Dirac fermions. Inset shows the transmittance of white light as a function of the number of graphene layers (squares) Source: Nair <i>et al.</i> (2008).	2
Figure 1.2. (a) Optical absorption spectrum, (b) density of excited states, (c) absorbance of graphene, with and without excitonic effects included Source: Yang <i>et al.</i> (2009).	3
Figure 1.3. Imaginary part of the dielectric function, obtained by solving BSE, of MoS ₂ for several k-point meshes (Left axis). Binding energy of the exciton (E_b) as a function of the number of irreducible k -points (Right axis) Source: Molina-Sánchez <i>et al.</i> (2013).	5
Figure 1.4. (a) Absorption spectrum of MoS ₂ without (dashed red curve) and with (solid green curve) electron-hole interaction using a constant broadening of 20 meV. (b) Same data using an <i>ab initio</i> broadening based on the electron-phonon interaction. (c) Previous calculation using G ₀ W ₀ (d) Experimental data Source: Qiu <i>et al.</i> (2013).	6
Figure 3.1. The number of k -points vs the RAM usage. The red, blue and green squares represents 3- (1L-), 9- (3L-), and 15-atom (5L-) MoS ₂ systems. The grey region show the available RAM (256 GB) of the machine that is used for tests. The red and circle at the crossing of the dashed lines show the predictions of the RAM requirements when 1L MoS ₂ for k -point sampling of $18 \times 18 \times 1$ and 3L MoS ₂ for k -point sampling of $15 \times 15 \times 1$ are calculated.	31
Figure 3.2. (a) The imaginary part of the dielectric function for different k -point samplings. For simplicity the sampling of $n \times n \times 1$ is represented as single number of n . (b) The excitation energy of the first excitonic peak for different k -point. The light-red curve is for tracking the convergence.	33

Figure 3.3. (a) The imaginary part of the dielectric function for different out-of-plane vector lengths. (b) The excitation energy of the first excitonic peak for different out-of-plane vector lengths. The light-blue curve is for tracking the convergence.	34
Figure 3.4. The imaginary part of the dielectric function for different energy cutoff of the response function in GW approximation. The first peak of the spectrum is zoomed and shown in the inset.	35
Figure 3.5. (a) The electronic band structure of single-layer MoS ₂ . Black curve is the GGA result. The blue circles are the quasi particle states at given path for highest two and lowest two bands of the VB and CB, respectively. (b) Imaginary dielectric function of single-layer MoS ₂ . The black curve is our calculated result and the red curve with circle is the experimental result from report of Mak et al(Mak <i>et al.</i> , 2010).	36
Figure 4.1. Top and tilted-side views of atomic structures of bulk (a) wurtzite and (b) hexagonal AlN (top panel). Their electronic band dispersion (lower panel).	38
Figure 4.2. Phonon dispersion of bulk <i>h</i> -AlN.	40
Figure 4.3. Monolayer <i>h</i> -AlN band diagram within PBE and HSE06 (left panel), partial density of states (middle panel) and the band decomposed charge densities of the band edges (right panel). Sections of 3D charge density that represent the connection to the neighboring cells are filled with blue color.	41
Figure 4.4. (a) Possible stackings between two layers of <i>h</i> -AlN. (b) Layer-layer interaction energy for different stackings. (c) Interlayer spacing dependent band dispersion of AA' stacked two layers of <i>h</i> -AlN.	42
Figure 4.5. Evolution of electronic band dispersion of <i>N</i> -layer <i>h</i> -AlN.	44
Figure 4.6. The evolution of the bonding charge density of <i>h</i> -AlN for monolayer, bilayer, 3-layer, 8-layer and 15-layer. Sections of 3D charge density that represent the connection to the neighboring cells are filled with blue color.	46
Figure 5.1. (a) and (b) illustrate the structure of monolayer 1T and 1H PbI ₂ , respectively. (c) and (d) are the corresponding band structures where the blue and red curves represent the GGA and GGA+SOC, respectively. The Fermi level (E_F) is given by green solid line.	49

Figure 5.2. (a) and (b) show the structure of H atom adsorbed (3×3) PbI_2 from top and the side, respectively. The inset in (a) illustrates the rotation of H around the I atom. (c) is the band structure of single H atom adsorbed 3×3 PbI_2 monolayer where the blue and red curves represent the spin-different states. Inset shows the charge distribution of VBM at the Γ . (d) is the diffusion barrier plot through the given path. The Fermi level (E_F) is given by green solid line.	52
Figure 5.3. The structures in (a) and (b) for perfect hexagonal and (c), (d), and (e) for distorted forms of half-hydrogenated monolayer PbI_2 (half-H- PbI_2), respectively. View direction are given in (d) and (e). (f) and (g) are the corresponding band structures. To compare the perfect and distorted forms, 2×2 unitcells are used for both band structures. The Fermi level (E_F) is given by green solid line.	53
Figure 5.4. (a), (b), and (c) illustrate the structure of full-hydrogenated monolayer PbI_2 from top, side views with the corresponding directions, respectively. (d) is the band structure of full-hydrogenated monolayer PbI_2 . The Fermi level (E_F) is given by green solid line.	56
Figure 6.1. (a) The top and side views of monolayer ZnSe . The red vectors stands for unitcell vectors. In panel (b), the phonon band structure and phonon density of states are shown. In Phonon-DOS panel, the total and the Γ projected phonon density of states are shown as grey area and red curve, respectively.	59
Figure 6.2. The energy-band dispersion is shown in (a). The VBM and CBM are labeled as I and II, respectively. In panel (b), the density of states with Zn and Se contributions are shown as the grey and green curves, respectively. The band decomposed charge densities of the VBM and CBM are shown in right panel. The arm-chair and zig-zag direction are represented by ac and zz , respectively.	61
Figure 6.3. (a) The surface plot of the total energy difference of the system under the strain in the arm-chair and zig-zag. The energy levels are color coded. The polar plots of the total energy difference of the system under the tensile (b) and compressive (c) strains, respectively. In panels (d) and (e), the polar plots of the angle dependent in-plane stiffness and the Poisson ratio are shown, respectively.	63

Figure 7.1. (a) and (b) illustrate the structure of monolayer 1T and 1H SnS ₂ , respectively. (c) and (d) are the band structures of 1T and 1H SnS ₂ . The blue curves and the curve with red-circles are for GGA+SOC and GGA+HSE06, respectively. (e) and (f) are absorbance and the reflectivity of the 1T (black curve) and 1H SnS ₂ (red curve).	66
Figure 7.2. (a), (b), and (c) are side views of bilayer SnS ₂ , and (d), (e), and (f) are band structures within the GGA+SOC (blue) and GGA+HSE06 (red-circle) for <i>AA</i> , <i>A'B</i> , and <i>AB</i> stackings, respectively. (g) and (h) are the calculated absorbance and reflectivity of the <i>AA</i> (black), <i>A'B</i> (red), and <i>AB</i> (green). The vertical lines in the inset of (g) represent the band gap values of the corresponding stacking orders.	68
Figure 7.3. Left panel, blue (red) curve indicates the energy difference when the top layer is sliding along the armchair (zig-zag) direction. Right panel, the structural forms of the extremas marked on the energy profiles are given.	71
Figure 7.4. The plot of the energy barrier in the armchair (a) and zig-zag (b) directions under increasing electric fields. The blue, black, green and red lines are for 0.05, 0.15, 0.25 V/Å electric field values, respectively. (c) electron transfer from outer S atoms to the inner part (upper) and the total number of electron difference (lower) between 0.25 V/Å and zero electric field on the sliding paths. (d) The cross section of the total charge density difference between zero and non-zero field cases for both <i>AA</i> and <i>AB</i> stacking orders.	72
Figure 7.5. Energy band dispersions under three different E-field which are 0.05, 0.15, and 0.25 V/Å perpendicular to the plane of structure. The blue curves are for <i>AA</i> stacking and red curves are for <i>AB</i> stacking.	73
Figure 7.6. Plot of the energy barrier for sliding in the armchair (a) and the zig-zag (b) direction for four different charging cases and the bare case. Positive value of charging refers to a higher electron density. The blue curves represents the bare case. The green, the black, the yellow and the red curves are for the charging case of -0.2 , -0.1 , 0.1 , $0.2 e^-$. (c) Cross section of the total charge density difference between the charged cases and the bare case.	75

Figure 7.7. Energy band dispersions for four different charging conditions which are -0.2 , -0.1 , 0.1 , and $0.2 e^-$. The negative numbers refer the electron subtracted (hole doping) cases and the positive numbers refer the electron added (electron doping) cases. The blue curves are for AA stacking and red curves are for AB stacking.	76
Figure 7.8. (a) Constant height energy landscape of bilayer SnS_2 . The height is fixed at the value corresponding to the distance between the top and the bottom sulfur atoms when the bilayer is fully relaxed. (b) The constant pressure energy dependence along the line connecting the AA and the AB stackings.	77
Figure 8.1. Optical absorption spectrum of (a) bulk hexagonal-AlN and (b) bulk wurtzite-AlN compared to experimentally obtained imaginary dielectric function Source: (Li <i>et al.</i> , 2003; Loughin <i>et al.</i> , 1993).	79
Figure 8.2. (a) Imaginary dielectric function and (b) layer dependent absorbance spectra of single-layer, bilayer, three-layer, and four-layer (1L, 2L, 3L, and 4L) h -AlN. The comparison with bulk h -AlN crystal is shown as an inset.	82
Figure 8.3. Electronic band structures of 1L, 2L, 3L, and 4L h -AlN. Zero level is set to the valence band maximum. Red arrows indicate important band-to-band (direct) transitions.	84
Figure 8.4. (a) Frequency dependent optical conductivity, (b) absorption coefficient and (c) reflectivity of 1L, 2L, 3L, and 4L h -AlN as a function of $\hbar\omega$	86
Figure 8.5. The variation of electron (red line) and hole effective mass (blue line) with respect to the number of layers. The bulk values are shown by dashed lines.	87
Figure 8.6. (a) Imaginary dielectric function, (b) absorption coefficient and (c) frequency dependent reflectivity of single-layer h -AlN under strain. Black solid curve stands for the unstrained case and dashed lines for strain values of 1%, 3%, 5% and 7%, respectively.	88
Figure 8.7. (a) Strain dependent band structures indicating the variation of the band-gap values (E) and (b) partial densities of states of monolayer h -AlN.	90

Figure 8.8. Many-body calculations of the optical response of monolayer and bilayer h -AlN (a) Comparison of RPA-spectra based on PBE, HSE and G_0W_0 calculations for monolayer h -AlN and (b) Optical spectra of mono- and bilayer h -AlN with electron-hole interactions taken into account.	91
Figure 9.1. (a) and (b) are the structures (top and side view) of monolayer h -AlN and $Mg(OH)_2$, (c) and (d) are the band structures of h -AlN and $Mg(OH)_2$, respectively. The blue and light-red curves with square are for GGA+SOC and GGA+ GW_0 , respectively.	93
Figure 9.2. The results of the k-point sampling tests: (a) and (b) The imaginary part of the dielectric functions of the monolayer h -AlN and $Mg(OH)_2$ for different k-point samplings, respectively. (c) The first exciton peak positions are shown as the blue and red squares for the monolayer h -AlN and $Mg(OH)_2$, respectively.	96
Figure 9.3. The results of vacuum spacing tests: (a) and (b) The imaginary part of the dielectric functions of the monolayer h -AlN and $Mg(OH)_2$ for different vacuum spacing values, respectively. (c) The first exciton peak positions are shown. The blue and red curves correspond to the monolayer h -AlN and $Mg(OH)_2$, respectively.	97
Figure 9.4. The imaginary part of the dielectric function of h -AlN (blue curve) and $Mg(OH)_2$ (red curve) with oscillator strength of excitonic states (vertical green lines). The first, second and third excitons are labeled as I, II, III with the subscript of the corresponding individual layer, respectively. The quasi-particle band gap of h -AlN (blue dashed) and $Mg(OH)_2$ (red dashed) at Γ and exciton binding energies ($E_{bind}^{exc.}$) are given.	98
Figure 9.5. (a) Top view of six different stacking orders, (b) Electronic band dispersion (left panel) and the partial density of state (right panel) of AB' stacking order. The $CB-\Gamma_1$ and $CB-\Gamma_2$ label the first and second lowest levels of the CB at Γ point, respectively.	99

Figure 9.6. (a) The imaginary part of the dielectric functions of the AB' stacked hetero-bilayer are shown for different interlayer distances starting from ground state distance of 2.13 Å. Δd refers to interlayer distance while the ground state distance is set to 0 and labeled as 0.0 Å. The lowest three exciton peaks are labeled as **I**_{bil}, **II**_{bil}, and **III**_{bil}. (b) The distance dependent oscillator strengths of lowest three excitons are shown. 102

Figure 9.7. (a) Layer-layer distance dependent band decomposed charge densities at the Γ point for the lowest two bands ($CB-\Gamma_1$ and $CB-\Gamma_2$) are presented. The the numbers on the upper part of the figure are distances between the layers in the unit of Å. The optimized layer-layer distance is set to 0.0 Å. (b) shows the wave function of the lowest three excitons which are labeled as **I**_{bil}, **II**_{bil}, and **III**_{bil}. The methodology for the determination of excitonic wave functions is given in part 9.1.2. 104

LIST OF TABLES

<u>Table</u>	<u>Page</u>
Table 3.1. Table of the results of test calculations. The test parameters are given in bold character.	30
Table 4.1. Calculated lattice parameter in the lateral direction a and lattice parameter in the vertical direction c , the distance between layers d_{LL} , the intralayer atomic distance between Al and N atoms d_{Al-N} , the charge transfer from Al atom to N atom $\Delta\rho$, the cohesive energy E_{coh} and the energy bandgap of the structure E_{gap} . (d) and (i) indicate direct and indirect bandgap, respectively.	39
Table 4.2. Calculated direct and indirect transition energies between the VB and CB edges of single to ten layered structures.	45
Table 5.1. Calculated parameters for monolayer PbI_2 are the lattice constant in the lateral direction, a ; the atomic distance Pb and I atoms, d_{Pb-I} ; the charge transfer from Pb to I atom, $\Delta\rho$; the work function Φ ; and the cohesive energy, E_c . E_g^{GGA} and $E_g^{GGA+SOC}$ are the energy band gap values within GGA and GGA+SOC, respectively.	50
Table 5.2. Calculated parameters for half- and full-hydrogenated monolayer PbI_2 (half-H- PbI_2 and full-H- PbI_2) are; the lattice constant in the lateral directions, \mathbf{a}_1 and \mathbf{a}_2 ; the angle between the lattice vectors, θ ; the work function Φ ; the cohesive energy, E_c ; the binding energy per H atom, E_{bind} ; the band gap, E_g^{GGA} ; and magnetic moment per primitive cell, μ . ..	55
Table 6.1. Calculated parameters for monolayer $ZnSe$ are; the lattice constants in the lateral directions, a and b ; the atomic distance between Zn and S atoms, d_{Zn-Se} ; the charge transfer from Zn to Se atom, $\Delta\rho$; and the cohesive energy per atom, E_c . $E_g^{GGA+SOC}$ is the band gap values within GGA+SOC.	60
Table 7.1. Calculated parameters for monolayer SnS_2 are the lattice constant in the lateral direction, a ; the distance between the subplanes of S, c ; the intralayer atomic distance, d_{Sn-S} ; the charge transfer from Sn to S atom, $\Delta\rho$; the work function Φ ; and the cohesive energy, E_c . E_g^{GGA} and E_g^{HSE06} are the energy band gap values within GGA+SOC and GGA+HSE06, respectively.	67

Table 7.2.	Calculated values for possible stacking types of bilayer 1T-SnS ₂ of the lattice constant in the lateral direction, a ; the distance between the S sublayers of the layers, d_{L-L} ; the energy difference between the structures per SnS ₂ , ΔE ; interlayer interaction potential per formula, E_{L-L} ; the work function, Φ ; and the cohesive energy, E_c . E_g^{GGA} and E_g^{HSE06} are the energy band gap values within GGA+SOC and GGA+HSE06, respectively.	70
Table 8.1.	Optimized lattice constant, band-gap, absorption onset and absorption peak position values of strained h -AlN	89
Table 9.1.	Calculated parameters for monolayer h -AlN and Mg(OH) ₂ are the lattice constant in the lateral direction, a ; the final charges of Al, N, Mg, O, and H, ρ_{Al} , ρ_N , ρ_{Mg} , ρ_O , ρ_H , respectively; the work function Φ ; the cohesive energy, E_{coh} ; and the spin-orbit splitting, Δ_{SO} . E_g^{GGA} and $E_g^{GW_0}$ are the energy band gap values within GGA+SOC and GGA+GW ₀ , respectively.	95
Table 9.2.	The stacking labels are given in the first column. Calculated parameters for bilayer heterostructure of h -AlN and Mg(OH) ₂ are; the interlayer distance, d_{L-L} ; the energy difference between the ground state, Δ_E ; the interaction energy between the layers, E_{int} ; and the work function Φ . E_g^{GGA} are the energy band gap values within GGA+SOC.	101

CHAPTER 1

INTRODUCTION

The realization of one-atom-thick carbon crystal, namely graphene (Novoselov *et al.*, 2004) which was considered as unfeasible, opened up a new class of material family; “two dimensional (2D) materials”. (Geim and Grigorieva, 2013). A decade of research effort has shown that physical properties of materials significantly deviates when the dimensionality reduce. (Butler *et al.*, 2013; Chhowalla *et al.*, 2013) Through the recent advances in the synthesis techniques, many new members joined to 2D crystal family, such as graphene derivatives (graphane, grapheneoxide, fluorographene and chlorographene), hexagonal BN and AlN, (Şahin *et al.*, 2009; Wang *et al.*, 2009; Kim *et al.*, 2012; Tsipas *et al.*, 2013; Bacaksiz *et al.*, 2015) silicene, (Cahangirov *et al.*, 2009; Kara *et al.*, 2012) germanene, (Cahangirov *et al.*, 2009) stanene, (Bechstedt *et al.*, 2012; Guzmán-Verri and Lew Yan Voon, 2007) transition-metal dichalcogenides (with formula MX_2 where $M=Mo, W, Re$ and $X=S, Se, Te$), (Coleman *et al.*, 2011; Gordon *et al.*, 2002; Horzum *et al.*, 2014; Ross *et al.*, 2014; Sahin *et al.*, 2013; Tongay *et al.*, 2014; Wang *et al.*, 2012) black phosphorus and metal hydroxides (such as $Mg(OH)_2$ and $Ca(OH)_2$) (Aierken *et al.*, 2015; Suslu *et al.*, 2016). Beside the structural stability of these materials, it was shown that 2D crystals also show a variety of exceptional electronic and optical properties. In particular, the dimensional reduction bring significant changes in their dielectric properties which leads to enhancement in the photoluminescence performance. Despite the large amount of work that has been done on the structural and electronic properties of 2D materials, theoretical and experimental research on their optical properties are in early stage.

One of the first experimental determination of the optical performance of graphene was performed by Nair *et al.* (Nair *et al.*, 2008). As shown in Figs. 1.1 (a) and (b), the reflection of single-layer graphene is very low, less than 0.1% in the visible region. However, its optical absorption $A = \pi\alpha = 2.3\%$ is considerable. In addition, in multi-layer graphene, the optical absorption is proportional to the number of layers, i.e., each graphene layer contributes 2.3% and the overall absorption is the superposition of those monolayers. However, such simple result may break down in the non-visible regions. In the work of Mak *et al.* (Mak *et al.*, 2008) two important aspects in the optical spectrum of graphene are: (i) possible many-body effects leading to a reduction of the optical conductivity at lower photon energies, and (ii) deviations from the linear dispersion that leads to

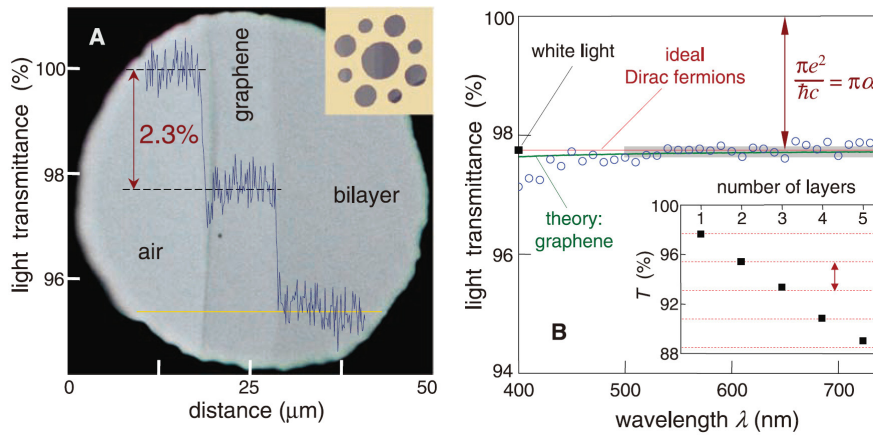


Figure 1.1. (a) Photograph of a 50- μm aperture partially covered by graphene and its bilayer. (b) Transmittance spectrum of single-layer graphene (open circles) and theoretically predicted results for two-dimensional Dirac fermions. Inset shows the transmittance of white light as a function of the number of graphene layers (squares) Source: Nair *et al.* (2008).

an increase of the optical absorption at high energies.

Sun *et al.* (Sun *et al.*, 2008) reported the first ultrafast spectroscopy of hot Dirac quasiparticles in epitaxial graphene in the region near the Fermi level. In the same year, infrared spectroscopy measurements performed by Wang *et al.* (Wang *et al.*, 2008) revealed that monolayers and bilayers of graphene have strong interband transitions and that their optical transitions can be substantially modified through electrical gating, much like electrical transport in field-effect transistors. This gate dependence of the interband transitions is an interesting tuning parameter for optically probing of the band structure of graphene. For monolayer graphene, it yields directly the linear band dispersion of Dirac fermions, whereas in bilayer graphene, a dominating van Hove singularity arising from interlayer coupling is observed. The strong and layer-dependent optical transitions of graphene and the tunability by simple electrical gating holds promise for new applications in infrared optics and optoelectronics.

In addition to the experimental studies, there are also theoretical investigations to reveal the optical performance of graphene. The first theoretical attempt to understand the optical properties of graphene within the first-principles method was made by Yang *et al.* in 2009. (Yang *et al.*, 2009) They investigated the optical properties of single and bilayer graphene including many-body effects. It is known that excitonic effects are suppressed in metals because of the high screening. However, they reported that the excitonic effects

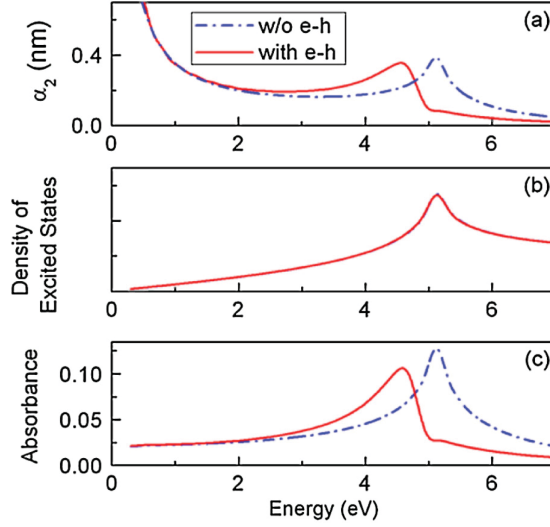


Figure 1.2. (a) Optical absorption spectrum, (b) density of excited states, (c) absorbance of graphene, with and without excitonic effects included Source: Yang *et al.* (2009).

significantly change the absorption spectrum (where the main peak position is red-shifted) in the energy regime near the van Hove singularity shown in Fig. 1.2, whereas excitonic effects do not change the absorbance in the infrared regime. (Yang *et al.*, 2009)

The optical properties of silicene and germanene, 2D buckled hexagonal structures, were also investigated theoretically. Bechstedt *et al.* studied the optical absorbance of graphene, silicene, and germanene by *ab-initio* calculations within the independent-particle approximation. The low energy absorbance was found to be the same for all structures as predicted for massless Dirac fermions ($A(0) = \pi\alpha$) and showed that the peaks and shoulders in the absorption spectrum can almost be related to band edges. (Matthes *et al.*, 2013; Bechstedt *et al.*, 2012) In addition to these Group-IV 2D materials, single-layer black phosphorus (phosphorene) was also studied. Çakır *et al.* calculated the optical properties of single-layer black phosphorus (phosphorene) using GW-BSE method and found that the optical response of the monolayer strongly depends on the direction and the magnitude of the applied strain. (Çakır *et al.*, 2014) Seixas *et al.* calculated the exciton binding energy of phosphorene under strain and found that strain modifies the binding energy of the excitons in the monolayer. (Seixas *et al.*, 2015)

In the literature, the optical properties of transition metal dichalcogenides (TMDs) (formulated as MX_2 where $M = Mo, W, Re$ and $X = S, Se, Te$) have attracted much more

attention. In early experimental studies on TMDs, Mak *et al.* (Mak *et al.*, 2010) and Splendiani *et al.* (Splendiani *et al.*, 2010) showed that the photoluminescence (PL) peak intensity of MoS₂ crystal remarkably increases when the crystal is thinned down to a monolayer. The strong enhancement in the PL intensity was explained as a consequence of an indirect to direct bandgap transition when going from multi to monolayer graphene. Subsequently similar indirect-to-direct bandgap crossover has been reported for other TMDs such as MoSe₂ (Tongay *et al.*, 2012; Tonndorf *et al.*, 2013), WSe₂ (Tonndorf *et al.*, 2013), and WS₂ (Gutiérrez *et al.*, 2013). The in-plane dielectric function of four different TMCs: MoS₂, MoSe₂, WS₂ and WSe₂ were determined by Li *et al.* (Li *et al.*, 2014) through reflectance measurements at room temperature. They concluded that for all four TMC monolayers, the two lowest energy peaks in the reflectance spectrum correspond to excitonic features that stem from interband transitions at the K (K') point, while at higher photon energies the spectral broad response originates from higher-lying interband transitions. In conventional semiconductors, increasing temperature or introducing defects usually reduces the PL strength. Interestingly, studies by Tongay *et al.* showed the opposite behavior in TMCs (Tongay *et al.*, 2013, 2012). They found that the PL of few-layer MoSe₂ was much enhanced with increasing temperature, due to the thermally driven crossover from indirect towards a direct bandgap (Tongay *et al.*, 2012). In another work, they observed an increase in the overall PL intensity as a result of the generation of vacancies in monolayer TMCs when put in a gas environment (such as N₂) (Tongay *et al.*, 2013). The interaction between the gas molecules and the defect sites, which caused a transition of exciton population from charged to neutral excitons, was responsible for the PL enhancement. In monolayer TMCs, due to the reduced screening of the Coulomb interaction, the exciton binding energy is much larger than in bulk materials. Ugeda *et al.* reported an exciton binding energy of 0.55 eV for monolayer MoSe₂ by means of scanning tunneling spectroscopy and the two-particle exciton transition energy using PL spectroscopy (Ugeda *et al.*, 2014).

In addition, many honeycomb lattice TMDs such as MoS₂ and WSe₂ showed rich valley-polarized optical properties. The inequivalent valleys in the Brillouin Zone could be selectively addressed using circularly-polarized light fields (Cao *et al.*, 2012; Jones *et al.*, 2013; Zeng *et al.*, 2012). Jones *et al.* (Jones *et al.*, 2013) reported the experimental generation and detection of valley coherence in WSe₂. Their study was based on the fact that excitons localized in a single valley emit circularly polarized photons. Linear polarization can only be generated through recombination of an exciton which is in a coherent superposition of the two valley states. Furthermore, Srivastava *et al.* realized a

valley Zeeman effect in WSe_2 .(Srivastava *et al.*, 2015) They showed strong anisotropic lifting of the degeneracy of the valley pseudospin degree of freedom by using an external magnetic field.

Monolayer TMDs are challenging system for calculating the optical properties because of various electronic and optical phenomenas play role in the optical excitations and exciton occurrence mechanism such as spin-orbit coupling and weak dielectric screening. To obtain accurate optical spectrum, it essential to include such effects correctly into the calculations.

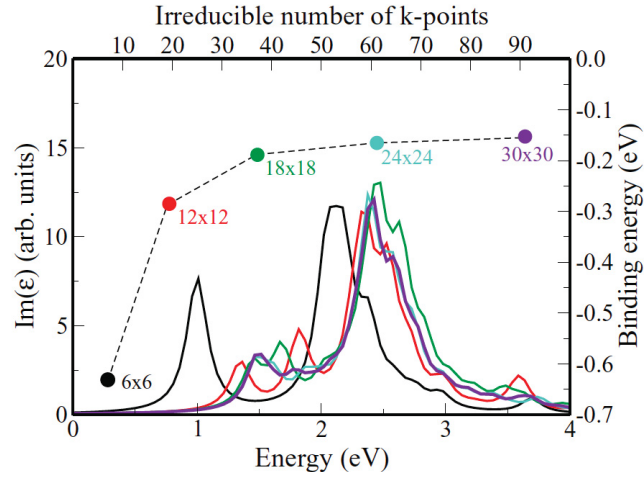


Figure 1.3. Imaginary part of the dielectric function, obtained by solving BSE, of MoS_2 for several k -point meshes (Left axis). Binding energy of the exciton (E_b) as a function of the number of irreducible k -points (Right axis) Source:Molina-Sánchez *et al.* (2013).

MoS_2 is one of the most investigated 2D materials among the TMDs. It is known from experiments that the positions of the A and B exciton peaks, which are the characteristics of PL spectrum in monolayer MoS_2 , are around 1.85 eV and 1.98 eV, respectively. Band structure calculations show that this splitting is due to the effect of spin-orbital coupling (SOC) at the K point of the BZ. In one of the several investigation on MoS_2 Cheiwchanchamnangij *et al.* showed that by using the self consistent GW method with Mott-Wannier theory, the MoS_2 is a direct gap semiconductor(Cheiwchanchamnangij and Lambrecht, 2012). It was found that the transition energy values for A and B excitons are 2.75 and 2.9 eV which is slightly overestimated as compared to the experimental values. Similarly, Ramasubramaniam showed that the MoS_2 is also an direct gap semiconductor by solving BSE over the single-shot GW method (G_0W_0) on top of Heyd-Scuseria-

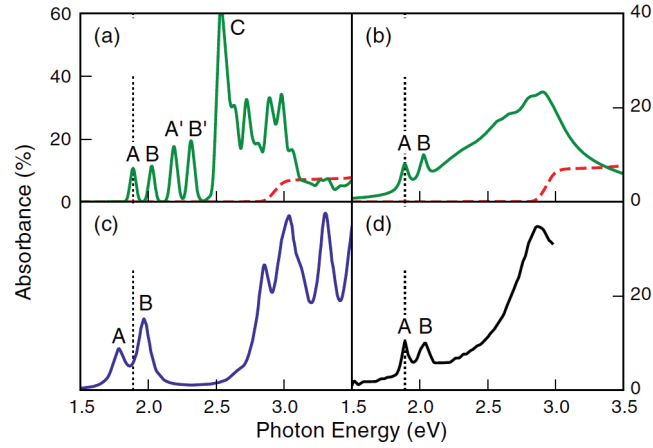


Figure 1.4. (a) Absorption spectrum of MoS₂ without (dashed red curve) and with (solid green curve) electron-hole interaction using a constant broadening of 20 meV. (b) Same data using an *ab initio* broadening based on the electron-phonon interaction. (c) Previous calculation using G₀W₀ (d) Experimental data Source: Qiu *et al.* (2013).

Ernzerhof (HSE) hybrid calculations (Ramasubramaniam, 2012). A and B excitons were found to be quite similar to the experimental values, 1.78 and 1.96 eV, respectively and with an exciton binding energy of 1.04 eV. By using self-consistent GW method, Shi *et al.* reported that in addition to A and B exciton peaks (at 2.22 eV), the A' and B' exciton peaks (at 2.50 eV) are also found which are not experimentally active (Shi *et al.*, 2013a). The discrepancies in the results are due to the different settings used in the calculations. For instance the dependence of the optical spectrum of the monolayer MoS₂ on the Brillouin Zone sampling is shown in Fig. 1.3. As can be seen the position of the peaks are moving towards higher energy values with increasing the k-point grid (Molina-Sánchez *et al.*, 2013; Shi *et al.*, 2013a).

To elucidate these discrepancies, a more recent work by Qiu *et al.* calculated the absorption spectrum of monolayer MoS₂ with very high settings (Qiu *et al.*, 2013). In this study the G part is updated self-consistently one time (G₁W₀) because an additional iteration change the the band gap by less than 20 meV. A 72 × 72 × 1 k-mesh is used with energy cutoff of $E_r = 476$ eV and $N_b = 6000$ bands where both parameters must be converged together for the accurate QP energies. The number of valance bands N_v and conduction bands N_c are selected as 7 and 8 for BSE calculation, respectively. Calculated absorption spectrum is shown in Fig. 1.4. They suggested that the previous calculations (Ramasubramaniam, 2012; Shi *et al.*, 2013a) were not converged with respect

to k-point sampling, and the agreement between the peak position for A and B and experimental results found in earlier reports are likely accidental. It was also suggested by Qiu *et al.* that the inconsistency between the converged calculations and the experiment can be solved by considering the quasiparticle lifetime effect due to electron-phonon interaction which is shown in Fig. 1.4 (b).

Furthermore, excitonic properties of 2D crystal structures show significant deviations from their bulk forms. While the exciton binding energy varies between few to 100 meV in an usual semiconductor, 2D TMDs have exciton binding energies of several hundred meV (Chernikov *et al.*, 2014; He *et al.*, 2014; Ugeda *et al.*, 2014; Ye *et al.*, 2014). Such a strong enhancement in the excitonic binding energy is attributed to two main effects: (i) the confinement forces that localize the electron and the hole at the same place (which causes a stronger binding energy), and (ii) the dielectric screening of the Coulomb interaction is significantly reduced due to the dielectric mismatch effect as compared to the bulk. In another recent study the screening properties of two-dimensional semiconductors and layered structures were investigated by Latini *et al.* It was shown that while the screened interaction in the generalized Mott-Wannier model yields results almost identical to those of the strict 2D model (*ab-initio* calculations) for exciton binding energies, it may fail for heterostructures and when supported 2D materials are present. They also showed that a quasi-2D model, that takes into account the finite extension of the 2D material in the out-of-plane direction, provides a much broader applicability (Latini *et al.*, 2015).

Most recent experimental efforts have also revealed that the synthesis of vertically stacked heterostructures consist of different monolayers can be achieved. These monolayers in heterostructures are binded with van der Waals-like interaction. Tongay *et al.* reported the synthesis of large-area (tens of micrometers) heterostructures of CVD-grown WS_2 and MoS_2 monolayers (Tongay *et al.*, 2014). They showed that the interlayer coupling can be tuned by vacuum thermal annealing. As the coupling strength increases, the photoluminescence gradually changes from a superposition of the spectra of MoS_2 and WS_2 monolayers to the coupled spectrum, in which charged exciton (also called trions) recombination and phonon-assisted indirect-bandgap transition dominate the light emission. Gong *et al.* also observed interlayer exciton transition in a MoS_2/WS_2 heterostructure, which leads to an additional PL peak at 1.4 eV (Gong *et al.*, 2014). Similar interlayer exciton transition in $\text{MoSe}_2/\text{WSe}_2$ heterostructure was also reported by Rivera *et al.*, and the interlayer exciton had a long lifetime of 1.8 ns, an order of magnitude longer than intralayer excitons (Rivera *et al.*, 2015). Besides their PL properties, Huo *et*

al. demonstrated enhanced optoelectronic performances of multilayer MoS₂/WS₂ heterostructure transistors, whose photoresponsivity is three orders of magnitude larger than for devices made of monolayer MoS₂(Huo *et al.*, 2014). Several studies have reported the observation of a photovoltaic response in MoS₂/WSe₂ heterostructures(Cheng *et al.*, 2014; Furchi *et al.*, 2014; Lee *et al.*, 2014). The collection of the photoexcited carriers can be enhanced by sandwiching MoS₂/WSe₂ between graphene(Lee *et al.*, 2014). Furthermore, Withers *et al.* demonstrated a new type of light-emitting diode based on van der Waals heterostructures, which consist of graphene, hexagonal boron nitride and various semiconducting TMCs such as MoS₂(Withers *et al.*, 2015). The devices showed a quantum efficiency up to 8.4%, and the emission spectrum can be tuned by choosing different semiconducting layers.

Beside the experimental investigations, there are several computational studies that revealed the effect of the heterostructure construction on excitonic properties. Komsa *et al.* calculated the optical absorption spectrum of vertical MoS₂/WS₂ heterostructure by solving BSE equation on top of single shot G₀W₀ calculation (Komsa and Krasheninikov, 2013) and it was observed that the optical spectrum of such a heterostructure has the same features as the individual monolayers and the optically active transitions are formed by direct intralayer transitions. Recently Kang *et al.* showed that certain van der Waals heterostructures, can facilitate spatial separate electron-hole localization which may find applications in photovoltaic energy conversion. (Kang *et al.*, 2013) The electronic structure of various heterostructures were calculated in the GW level by Debbichi *et al.* They predicted that due to the band alignment, the MX₂ heterostructures can be used as charge separator for solar cell applications(Debbichi *et al.*, 2014). The exciton radiative lifetimes of MoS₂/WS₂ and MoSe₂/WSe₂ bilayer heterostructures are calculated by solving the BSE equation on top of GW calculation. It is predicted that these heterobilayers exhibit long-lived ($\sim 20 - 30$ ns at room temperature) excitons whose electron is localized on the Mo and the holes are localized on the W based layer(Palumbo *et al.*, 2015).

Moreover, Torun *et al.* investigated the optical properties of GaS/Ca(OH)₂ heterobilayer by solving the Bethe-Salpeter equation on top of a single shot GW calculation (G₀W₀)(Torun *et al.*, 2016). They showed that heterobilayer construct a type II heterojunction which leads to spatially indirect excitons due to localization of the electrons and holes in different monolayers of the heterostructure. They also found that the calculated optical spectra of different stacking types of the heterostructure show dissimilarities, although their electronic structures are rather similar. Most resently, we investigated optical

properties of vertically stacked h-AlN and Mg(OH)₂, through *ab initio* DFT, the GW approximation and the BSE(Bacaksiz *et al.*, 2017). We found that the heterobilayer possesses excitonic peaks, which appear only after the construction of the heterobilayer and the exciton wave function calculation shows that the first peak of the heterobilayer originates from spatially indirect exciton where the electron and hole localized at h-AlN and Mg(OH)₂, respectively, which is important for the light harvesting applications.

Above-mentioned experimental and theoretical studies show that the optical properties and related applications of 2D materials gain more and more attentions. For that reason, the theoretical investigations is needed more than ever for elucidating the experimental observation, characterization of the materials, and also reliable prediction of possible structures. Therefore, in this thesis, we aim to give complete methodology for computing the optical properties of the ultra-thin materials by using DFT and beyond DFT approaches such as GW approximation and BSE. In the methodology part, firstly we will summarize light-matter interaction, secondly basic demonstration of DFT will be given. Thirdly, beyond DFT approaches will be shown. Following the methodology, the applications of given methods will be presented as complete published scientific articles.

CHAPTER 2

THEORETICAL BACKGROUND AND METHODOLOGY

2.1. Light-Matter Interaction

The section focuses to the basic concepts of the light-matter interaction. First, a classical interpretation of the light and then the dielectric function are given. Next, a quantum mechanical approach to light-matter interaction is demonstrated. The section mainly follows the book by Mark Fox(Fox, 2002).

2.1.1. Electromagnetic Waves in a Material

Since light is composed of oscillating electric and magnetic field vectors, to comprehend the response of a material to the light, it is essential to understand the interaction between electromagnetic wave and the material. In this regard, the interaction between the electric field and the dielectric medium is discussed. The light-matter interaction is governed by three macroscopic quantity; the electric field, E , the polarization of the material, P , and the electric displacement, D . In particular, the applied electric field, E , produces polarization by displacing the negative and positive charges in the atoms to the opposite direction. Adding these microscopic dipole moments ends up the total polarization, P , which is aligned parallel to the E . The relation is written as

$$P = \epsilon_0\chi E \quad (2.1)$$

where ϵ_0 is the dielectric constant of the free space and χ is the electric susceptibility of the medium. Here we assuming that the P varies linearly with the applied electric field. The electric displacement, D , can be written as follows

$$\begin{aligned} D &= \epsilon_0 E + P \\ D &= \epsilon_0 E + \epsilon_0\chi E \\ D &= \epsilon_0(1 + \chi)E \end{aligned} \quad (2.2)$$

$\epsilon_r = (1 + \chi)$ is the relative dielectric constant which determines the interaction between the electromagnetic waves and the dielectric medium.

The interaction between the materials and the external magnetic field can be treated similarly. The magnetization in the medium, M , depends on the magnetic field strength, H , and magnetic susceptibility, χ_M , as follows:

$$M = \chi_M H \quad (2.3)$$

and

$$\begin{aligned} B &= \mu_0(H + M) \\ B &= \mu_0(H + \chi_M H) \\ B &= \mu_0 \mu_r H \end{aligned} \quad (2.4)$$

where the μ_0 is the magnetic permeability of the vacuum and $\mu_r = 1 + \chi_M$ is the relative magnetic permeability of the medium.

The Maxwell's equations of the electromagnetism summarize the electric and magnetic response of the medium.

$$\nabla \cdot D = \rho, \quad (2.5)$$

$$\nabla \cdot B = 0, \quad (2.6)$$

$$\nabla \times E = -\frac{\partial B}{\partial t}, \quad (2.7)$$

$$\nabla \times H = j + \frac{\partial H}{\partial t}, \quad (2.8)$$

where ρ and j are free charge and current densities, respectively. The first equation is the Gauss's law and the second equation is equivalent to Gauss's law for the magneto-static. The third one is the combination of the Faraday and Lenz laws of electromagnetic induction. The fourth one is the Ampere's law. If there is no free charge and current, the Maxwell's equations can have wave-like solutions. Hence, we take the curl of third equation with substituting the fourth one:

$$\nabla \times (\nabla \times E) = \nabla \times \left(-\mu_0 \mu_r \frac{\partial H}{\partial t} \right), \quad (2.9)$$

$$\nabla \times (\nabla \times E) = -\mu_0 \mu_r \epsilon_0 \epsilon_r \frac{\partial^2 E}{\partial t^2}, \quad (2.10)$$

Here $\nabla \times (\nabla \times E) = \nabla(\nabla \cdot E) - \nabla^2 E$ and $\nabla \cdot E = 0$, so

$$\nabla^2 E = \mu_0 \mu_r \epsilon_0 \epsilon_r \frac{\partial^2 E}{\partial t^2}, \quad (2.11)$$

The solutions of this wave equation is in the form of

$$E(z, t) = E_0 e^{i(kz - \omega t)} \quad (2.12)$$

where E_0 is the amplitude, z is the propagation direction, and ω is the angular frequency. $k = \frac{2\pi}{\lambda} = \frac{\omega}{v} = \frac{n\omega}{c}$ is the wave vector, $v = \frac{1}{\sqrt{\epsilon_r \mu_r}} c$ is the velocity of wave, and $c = \frac{1}{\sqrt{\epsilon_0 \mu_0}}$ is the speed of light in free space. $n = \sqrt{\epsilon_r \mu_r}$ is the refractive index which is an important parameter as mentioned before. Note that at optical frequencies, $\mu_r = 1$, so the refractive index is $n = \sqrt{\epsilon_r}$. The refractive index, n , or the relative dielectric constant, ϵ_r , is complex in many cases. More detailed look will be in the next section.

In general, an electromagnetic wave propagating in the z direction have electric field components along both the x and y axes as $E_0 = E_{x0} \hat{\mathbf{x}} + E_{y0} e^{i\Delta\phi} \hat{\mathbf{y}}$:

$$E_x(z, t) = E_{x0} e^{i(kz - \omega t)} \quad (2.13)$$

$$E_y(z, t) = E_{y0} e^{i(kz - \omega t + \Delta\phi)} \quad (2.14)$$

The electromagnetic wave can have several type of polarization such as linearly and circularly. The relative amplitude and the phase difference between the directional components determine the polarization type of the light.

For linearly polarized light, the polarization vector points constant direction and $E_0 = E_{x0} \hat{\mathbf{x}} \mp E_{y0} \hat{\mathbf{y}}$ where $-$ and $+$ signs stand for the $\Delta\phi = 0$ and $\Delta\phi = \pi$, respectively.

For the case of circularly polarized light, the polarization vector rotates around the propagation direction as the wave propagates. The light can have either right or left circular polarization. If the electric field vector rotates clockwise (anti-clockwise) as the observer looks trough the source, the light have right (left) circular polarization and is represented by the symbol of σ^+ (σ^-). The electric vector form of the circularly polarized light can be written as:

$$\sigma^\mp = E_0 (\hat{\mathbf{x}} \mp i \hat{\mathbf{y}}) / \sqrt{2} \quad (2.15)$$

A simple example for reflection and transmission of light from vacuum to a medium having refractive index \tilde{n} can be treated by using Maxwell's equations. The tilde indicates the refractive index is considered to be complex. For the simplicity, the wave is considered to be have polarization vector in the x direction and incidence angle parallel to the normal of the surface. There are indecent, reflected, and transmitted waves where we show them as superscript letters of i , r , and t , respectively. The boundary conditions tell us that (i) the summation of electric and magnetic fields is equal to zero and (ii) the summation of

the tangential component of the electric and magnetic fields is continuous.

$$E_x^i + E_x^r = E_x^t \quad (2.16)$$

$$H_x^i - H_x^r = H_x^t \quad (2.17)$$

By using Maxwell's equation, the second equation here can be written as

$$E_x^i - E_x^r = \tilde{n} E_x^t \quad (2.18)$$

where the refractive index of the vacuum is equal to 1 and the magnetic permeability of the medium is also 1 at the optical frequencies which are interested here. Therefore, the reflectivity is in the form of:

$$R = \left| \frac{E_x^r}{E_x^i} \right|^2 = \left| \frac{\tilde{n} - 1}{\tilde{n} + 1} \right|^2 \quad (2.19)$$

This simple example also shows the importance of the complex refractive index, consequently the dielectric constant, which determines the response of the medium to the electromagnetic wave.

2.1.2. The Complex Refractive Index and Dielectric Function

In the previous section, we briefly showed that the reflectivity of a medium can be described by using only the refractive index. In this section we focus on how the complex refractive index or dielectric constant of a material determines the optical activities. The complex refractive index can be written as

$$\tilde{n} = n + i\kappa \quad (2.20)$$

where n and κ are the normal refractive index and extinction coefficient of the medium, respectively. Let assume that a wave propagating along the z direction and having the electric field part in the form of:

$$E(z, t) = E_0 e^{i(kz - \omega t)} \quad (2.21)$$

where $k = \tilde{n} \frac{\omega}{c} = (n + i\kappa) \frac{\omega}{c}$. So the the form of the wave becomes:

$$\begin{aligned} E(z, t) &= E_0 e^{i(\tilde{n} \frac{\omega}{c} z - \omega t)} \\ &= E_0 e^{-\kappa \frac{\omega}{c} z} e^{i(n \frac{\omega}{c} z - \omega t)} \end{aligned} \quad (2.22)$$

As it is seen, the extinction coefficient results in an exponential decay of the wave. In other word, the intensity of the light, which is proportional to the square of the electric field, decreases with the decaying rate of

$$\alpha = 2\kappa \frac{\omega}{c} \quad (2.23)$$

which is also known as the absorption coefficient.

We also mentioned that the refractive index and the relative dielectric constant are related by the formula of $n = \sqrt{\epsilon_r}$. Consequently, if the refractive index is complex, the relative dielectric constant can be written in the complex form:

$$\tilde{n}^2 = \tilde{\epsilon}_r = \epsilon_1 + i\epsilon_2. \quad (2.24)$$

where $\epsilon_1 = n^2 + \kappa^2$ and $\epsilon_2 = 2n\kappa$. We can rewrite the refractive index, n , and extinction coefficient, κ , in terms of ϵ_1 and ϵ_2 as

$$n = \frac{1}{\sqrt{2}} (\epsilon_1 + (\epsilon_1^2 + \epsilon_2^2)^{1/2})^{1/2} \quad (2.25)$$

$$\kappa = \frac{1}{\sqrt{2}} (-\epsilon_1 + (\epsilon_1^2 + \epsilon_2^2)^{1/2})^{1/2}. \quad (2.26)$$

As we mentioned in the previous section, the reflectivity is related with the complex refractive index then we can rewrite the reflectivity in the form of

$$R = \frac{(n - 1)^2 + \kappa^2}{(n + 1)^2 + \kappa^2} \quad (2.27)$$

and we can also write the transmissivity as

$$T = (1 - R)^2 e^{-\alpha l} \quad (2.28)$$

where R , α , and l are the reflectivity, absorption coefficient, and thickness of the material, respectively.

At this point, the absorption coefficient and the reflectivity can be defined by the complex relative dielectric constant, however the frequency dependence of these optical parameters must be investigated. To do this, a classical model, in which the atom is treated as a dipole that oscillates under the influence of varying electromagnetic wave, is used. According to the model, the negative charged particle, electron, binds to the positive charged nuclei by a spring having a series of characteristic resonant frequencies which correspond to the transition energies. Since, the nuclear mass is much more greater than the electron mass, the resonant frequency can be written as $\omega_0^2 = \frac{k_s}{m_0}$. It is reasonable to assume that the dipole oscillator has damping parameter which stands for the interaction between an electron and thermally excited phonons.

The displacement x of the electron fits the differential equation in the form of:

$$m_0 \frac{d^2 x}{dt^2} + m_0 \gamma \frac{dx}{dt} + m_0 \omega_0^2 x = -eE \quad (2.29)$$

where m_0 , γ , ω_0 , and e are the mass of an electron, the damping rate, the resonant frequency, and the charge of an electron, respectively. The electric field is considered to be:

$$E(t) = E_0 \cos(\omega t + \phi) = E_0 \text{Re}(e^{-i(\omega t + \phi)}) \quad (2.30)$$

where E_0 is amplitude and ϕ is the phase of the light. The solution of the equation is in the form:

$$x(t) = X_0 \text{Re}(e^{-i(\omega t + \phi')}). \quad (2.31)$$

If the phase of the displacement and electric field vanish each other, the amplitude of X_0 is then obtained as

$$X_0 = \frac{-eE_0/m_0}{\omega_0^2 - \omega^2 - i\gamma\omega}. \quad (2.32)$$

As we know that the dipole moment is $p(t) = -ex(t)$ for the single atom in the medium. The contributions to the macroscopic polarization at the frequency of ω_0 :

$$\begin{aligned} P_{res} &= Np \\ &= -Nex \\ &= \frac{Ne^2}{m_0} \frac{1}{\omega_0^2 - \omega^2 - i\gamma\omega} E \end{aligned} \quad (2.33)$$

In reality, there are multiple resonant frequencies, so P can be written as :

$$P = \left(\frac{Ne^2}{m_0} \sum_j \frac{1}{\omega_j^2 - \omega^2 - i\gamma_j\omega} \right) E \quad (2.34)$$

As we stated above, the dielectric displacement D of the medium and the polarization are related.

$$\begin{aligned} D &= \epsilon_0 E + P \\ &= \epsilon_0 \epsilon_r E, \end{aligned} \quad (2.35)$$

and

$$\epsilon_r = 1 + \frac{Ne^2}{\epsilon_0 m_0} \sum_j \frac{1}{\omega_j^2 - \omega^2 - i\gamma_j\omega} \quad (2.36)$$

where the imaginary and real parts according to $\epsilon_r = \epsilon_1 + i\epsilon_2$ are

$$\epsilon_1(\omega) = 1 + \frac{Ne^2}{\epsilon_0 m_0} \sum_j \frac{\omega_j^2 - \omega^2}{(\omega_j^2 - \omega^2)^2 + (\gamma_j \omega)^2} \quad (2.37)$$

$$\epsilon_2(\omega) = \frac{Ne^2}{\epsilon_0 m_0} \sum_j \frac{\gamma_j \omega}{(\omega_j^2 - \omega^2)^2 + (\gamma_j \omega)^2}. \quad (2.38)$$

The dipole oscillator model assumes that each oscillator contributes equally. However, in the actual absorption spectrum, the dispersion of dielectric constant varies between different transitions. It is known that the variation originates from difference in the quantum mechanical transition probability which can be put into the dielectric constant as:

$$\epsilon_r = 1 + \frac{Ne^2}{\epsilon_0 m_0} \sum_j \frac{f_j}{\omega_j^2 - \omega^2 - i\gamma_j \omega} \quad (2.39)$$

where f_j is known as the oscillator strength of the j 'th transition. The quantum mechanical interpretation is given in the next section.

2.1.3. Absorption

In this section, we aim to explain the physical processes that an electron is excited to a empty state by absorbing a photon. We consider semiconductor crystals which are enough to give the main points. Differing from the discrete atomic or molecular energy levels, the semiconductor crystals have continuous energy bands which lead to the continuous absorption spectrum. In addition, the absorption spectrum of a semiconductor have an edge at the lower part of the energy axis which is caused by transitions along the fundamental band gap of the material. In other word, if the photon has lower energy than the band gap, the interband transition from the valance to conduction band is not possible and the absorption spectrum does not show any dispersion at that region.

Before deeper analysis, we must distinct the electronic band structure of the materials based on whether the band gap is direct or indirect. For the direct band gap, the valance band maximum (VBM) and the conduction band minimum (CBM) occur at the same point in the Brillouin Zone. The conservation of the momentum indicates that when an electron absorbs a photon, the wave vector of that electron charges by a wave vector of absorbed photon. However, in the optical region, the wave vector value of a photon is about 10^7 m^{-1} . The wave vector of the electron, on the other hand, is in the order of 10^{10} m^{-1} which is related to the size of the first Brillouin Zone of the crystal. This means that the change in the wave vector during the absorption is negligible and can be considered

as a direct transition. Therefore, the interband absorption from the VBM to the CBM occurs when the band gap is direct and for the indirect band gap materials, the interband absorption between the band edges needs additional wave vector to carry the electron in the Brillouin Zone from VBM to CBM.

The interband transition rate is governed by the Fermi's golden rule which is related to the absorption coefficient, α . Let consider initial ($|i\rangle$) and final ($|f\rangle$) states which correspond to the state of an electron before and after absorption of a photon, respectively. The transition rate can be written as

$$W_{i \rightarrow f} = \frac{2\pi}{\hbar} |M|^2 g(\hbar\omega) \quad (2.40)$$

where M stands for the perturbation on the electron by a photon and $g(\hbar\omega)$ is the density of states at E_i and E_f when the difference between these band energies is $\hbar\omega$.

Firstly, the perturbation term is discussed. Here the perturbation potential is given as the electric-dipole interaction between the light and electron,

$$H' = -p_e \cdot \mathbf{E}_{\text{photon}} \quad (2.41)$$

$$M = \langle f | H' | i \rangle \quad (2.42)$$

$$= \int \psi_f^*(\mathbf{r}) H'(\mathbf{r}) \psi_i(\mathbf{r}) d^3\mathbf{r} \quad (2.43)$$

The light wave and the crystal wave functions can be written in the form of plane waves:

$$H' = -p_e \cdot \mathbf{E}_0 e^{i\mathbf{k} \cdot \mathbf{r}} = -e\mathbf{r} \cdot \mathbf{E}_0 e^{i\mathbf{k} \cdot \mathbf{r}} \quad (2.44)$$

$$\psi_i(\mathbf{r}) = \frac{1}{\sqrt{V}} u_i(\mathbf{r}) e^{i\mathbf{k}_i \cdot \mathbf{r}} \quad (2.45)$$

$$\psi_f(\mathbf{r}) = \frac{1}{\sqrt{V}} u_f(\mathbf{r}) e^{i\mathbf{k}_f \cdot \mathbf{r}} \quad (2.46)$$

We substitute into M , then

$$M = \frac{e}{V} \int (u_f^*(\mathbf{r}) e^{-i\mathbf{k}_f \cdot \mathbf{r}}) (\mathbf{E}_0 \cdot \mathbf{r} e^{i\mathbf{k} \cdot \mathbf{r}}) (u_i(\mathbf{r}) e^{i\mathbf{k}_i \cdot \mathbf{r}}) d^3\mathbf{r} \quad (2.47)$$

The conservation of momentum requires to be $\mathbf{k}_f - \mathbf{k}_i = \mathbf{k}$ then M becomes

$$M = \frac{e}{V} \int u_f^*(\mathbf{r}) (\mathbf{E}_0 \cdot \mathbf{r}) u_i(\mathbf{r}) d^3\mathbf{r} \quad (2.48)$$

It is seen that M is directly related to the envelop functions of the crystal and the polarization of the light. Since the envelop functions are periodic functions as the lattice, the integral can be reduced to a single unit cell of the crystal.

Secondly, the density of states $g(\hbar\omega)$, in other words, the joint density of states will be presented. The joint density of states is a quantity that holds the number of states

within the continuous bands for both initial and final electron states. The density of states per unit energy range can be written as $g(E)dE = 4\pi k^2 g(k)dk$. This gives

$$g(E) = \frac{4\pi k^2 g(k)}{dE/dk} \quad (2.49)$$

where $g(k)$ is the number of states per unit volume in k -space. So $g(k)$ can be written as

$$g(k) = \frac{V}{8\pi^3}, \quad (2.50)$$

where V is volume. dE/dk is the derivative of the energy dispersion curve which is unique for the crystal. If the band diagram of the material is known, the joint density of states $g(E)$ can be evaluated. We rewrite the transition rate and absorption coefficient as

$$\alpha(\hbar\omega) \propto W_{i \rightarrow f} \propto \left| \int_{unitcell} u_f^*(\mathbf{r})(\mathbf{E}_0 \cdot \mathbf{r})u_i(\mathbf{r})d^3\mathbf{r} \right|^2 \frac{V}{2\pi^2} \frac{k^2}{dE/dk} \quad (2.51)$$

If the envelop functions, u_i and u_f , and the electronic band structure are obtained accurately, the absorption coefficient can be determined. It can be assumed that the absorption coefficient is directly related to the imaginary part of the dielectric function, ϵ_2 , for a materials in which the normal refractive index is much more larger than the extinction coefficient, $n \gg \kappa$. This is generally true for the materials having low atomic densities. The 2D materials fit this conditions with their trademarks of low thickness. The assumptions is also valid for the semiconducting materials where the absorption is almost zero when the photon energy is away from the resonant energies.

In addition to the interband absorption, there are exciton formations and photon emission by recombination of the electron-hole in the optical processes which are discussed in the following sections.

2.1.4. Exciton

The interband absorption, which we discussed in the previous section, created an electron in conduction and a positive charged particle, hole, in the valance band. The Coulomb interaction between these particle leads to hydrogen-like bound state which is called exciton. Generally, there are two types of exciton: *Wannier-Mott* excitons and *Frenkel* excitons.

Wannier-Mott excitons are observed usually in semiconductors with small binding energy (a few 0.01 eV)between the electron and hole, hence the distance between electron-hole pair is much larger than the spacing between atoms. It is also called ‘‘free exciton’’ because the electron-hole pair can freely move in the crystal.

Frenkel excitons, on the other hand, are localized states with small exciton radius which is comparable with the size of the crystal unitcell. Consequently, the binding energy is in the order of 0.1-1.0 eV which is larger as compared to those of Wannier-Mott excitons.

Excitons in 2D materials, on the other hand, must be treated in more rigorous way. There two significant difference in the exciton formation between 2D materials and the bulk materials. One of them is that the dielectric environment that the exciton experiences changes when the material goes from 3D to 2D. To be more precise, the dielectric screening between electron and hole survives only in the layer when the structure is in the single-layer form. It results significant increase in the interaction of the electron-hole couple. The other difference between the 2D excitons and 3D excitons is that in 2D materials the electron and hole are confined into the layer which results increment in the single-particle energies and also increment in the interaction between electron and hole by forcing them stay close to each other. Due to these differences, the exciton binding energies are observed as a few hundred meV.(Chernikov *et al.*, 2014; He *et al.*, 2014; Ugeda *et al.*, 2014; Ye *et al.*, 2014)

2.1.5. Light Emission

In previous section, we refereed to interband absorption of light and exciton formation as a post process. In this section, we consider the relaxation of the excited electron by emitting photon. The radiative emissions are called luminescence. Since there are some other non-radiative relaxation mechanisms such that excited electron can loss its energy by emitting phonons.

Luminescence process is strongly related to the relaxation of the electron in the continuous band and the population at the state where the emission occurs. Usually, the emitting states are CBM and VBM for electron and hole, respectively. This also means that the absorption and emission spectrum differ. For semiconductors, the absorption spectrum have a threshold which corresponds to the band gap and continuous absorption line for the higher energy region, on the other hand, the emission spectrum is a narrow peak at around the band gap energy with slight shift through the lower energy that corresponds to the exciton binding energy.

2.1.6. Optical Measurements

A measurement of the absorption coefficient of a material is made as a collective measurements of transmission and reflection. A white-light is filtered by a monochromator and is incident on a thin platelet and the the transition and reflection data is collected for a wide range of wavelength. The detector should be at proper positions so that the reflected light is collected at the normal incident. The transmissivity is obtained by comparing cases that one in the presence of sample and one without sample. If the thickness is known the absorption coefficient can be deduced from the Eqn. 2.28. Recent developments on techniques provide more accurate and informative results by regarding polarization directions of the incident and collected lights, s and p orbital planes in the sample. A careful analysis after the measurement allows to be determined the real and imaginary parts of the refractive index.

Differing from the transition and reflection measurement, an emission, in other word, a luminescence measurement is made such a way that the sample is exposed laser or bright lamp having photon energy larger than the band gap of the sample, then the luminescent light collected and the whole spectrum is recorded at once by using an array of detector. As mentioned in previous section, the emission spectrum is a result of the post absorption processes and is not the same as absorption. However, since the luminescence peaks are related to the excited carrier density, it is determined by the absorption coefficient. Some sophisticated technique that records the luminescence as a function of time in ps range after the excitation of ultra-fast laser pulse allow us direct information about the absorption coefficient, carrier relaxation in the electronic band, and electron-hole recombination mechanisms.

2.2. Density Functional Theory

In this section, the basics of the density functional theory (DFT) are given mainly based on “Electronic Structure: Basic Theory and Practical Methods” by Richard M. Martin(Martin, 2004). As a theory of correlated many particle system, DFT is most widely used method for the structural, vibrational, electronic, and optical properties of materials such as bulk and lower dimensional crystallines, and also molecular structures. Briefly, DFT asserts that any property of an interacting many particle system can be written as a functional of the ground state density which is a function of position. The proof of the

assertion is demonstrated by Hohenberg and Kohn in 1968.(Hohenberg and Kohn, 1964) However, without a way of construct a functional, the many-body problem is impossible to solve by means of Hohenberg and Kohn theorem. The ansatz of Kohn and Sham provides a method to approximate a functionals for real system by replacing the original many-body problem with an independent-particle problem.(Hohenberg and Kohn, 1964) Kohn-Sham approach is now the basis most of computational works that are called “first principles” or “*ab-initio*” calculations. The functionals local density approximation and generalized gradient approximation, which we explain below, give remarkably accurate results for prediction of the structural and electronic properties of the many-body systems. Here, we demonstrate basics of the DFT by starting from the general hamiltonian of a many-body system:

$$H = -\frac{\hbar^2}{2m_e} \sum_i \nabla_i^2 + \sum_{i,I} \frac{Z_I e^2}{|\mathbf{r}_i - \mathbf{R}_I|} + \frac{1}{2} \sum_{i \neq j} \frac{e^2}{|\mathbf{r}_i - \mathbf{r}_j|} - \sum_I \frac{\hbar^2}{2M_I} \nabla_I^2 + \frac{1}{2} \sum_{I \neq J} \frac{Z_I Z_J e^2}{|\mathbf{R}_I - \mathbf{R}_J|} \quad (2.52)$$

The first term represents the total kinetic energy of the electrons counted by i . The second term stands for the external potential on the electrons arising from the nuclei. The third term is the Coulomb interaction energy between i 'th and j 'th electrons. Regarding that the mass of nuclei is infinity large as compared to the mass of electron, which is the implication of Born-Oppenheimer Approximation(Born and Oppenheimer, 1927), the fourth term can be ignored. The last term donates the Coulomb interaction between I th and J th nuclei. Hence, the Hamiltonian can be written in simple form of

$$H = T + V_{ext} + V_{int} + E_{II}. \quad (2.53)$$

Density functional theory is first proposed by Thomas(Thomas, 1927) and Fermi(Fermi, 1927). Their approximation is not accurate enough for electronic structure calculation for present-day.

2.2.1. Hohenberg-Kohn Theorems

The approach stands on two theorems which were first proved by Hohenberg and Kohn(Hohenberg and Kohn, 1964). It is shown that all properties of a quantum many-body system can be considered as unique functionals of the density of the particles in the ground state.

Theorem I : For any system of interacting particles in an external potential $V_{ext}(\mathbf{r})$, the potential $V_{ext}(\mathbf{r})$ is determined uniquely by the ground state particle density, $n_0(\mathbf{r})$.

Theorem II : A universal functional for the energy, $E[n]$, can be defined in terms of the density $n(\mathbf{r})$ and this functional is valid for any external potential $V_{ext}(\mathbf{r})$. For the exact ground state of the system, the functional has its global minimum value, and the density that minimizes the functional is the exact ground state density $n_0(\mathbf{r})$.

The ground state energy is the expectation value of the hamiltonian in terms of the ground state wave function.

$$E = \frac{\langle \Psi_0 | H | \Psi_0 \rangle}{\langle \Psi_0 | \Psi_0 \rangle} \equiv \langle H \rangle = \langle T \rangle + \int d^3\mathbf{r} V_{ext}(\mathbf{r})n_0(\mathbf{r}) + \langle V_{int} \rangle + E_{II}. \quad (2.54)$$

The proofs of the theorems are simple. However, at this stage, there is not any way to construct functionals and the original problem still stands.

2.2.2. Hellmann-Feynman Theorem

The theorem, which was formulated as it's last form by Hellman(Hellmann, 1939) and Feynman(Feynman, 1939), identifies that the force on a nucleus can be written in terms of the charge density independent of the electron exchange and correlation, and also kinetic energy. The Hellmann-Feynman theorem is essential for the DFT-based calculations because it provide to find optimum structural parameters such as lattice constants, atomic bond lengths, and bond angles. The force conjugate to any parameter in the hamiltonian of the system such as the position of a nucleus, \mathbf{R}_I .

$$\mathbf{F}_I = -\frac{\partial E}{\partial \mathbf{R}_I} \quad (2.55)$$

where the force depends only on the density of electrons, n , and the other nuclei. When we consider the total energy expression in Eqn. 2.54, the force can be written as

$$\mathbf{F}_I = -\frac{\partial E}{\partial \mathbf{R}_I} = -\int d^3\mathbf{r} n(\mathbf{r}) \frac{\partial V_{ext}(\mathbf{r})}{\partial \mathbf{R}_I} - \frac{\partial E_{II}}{\partial \mathbf{R}_I} \quad (2.56)$$

2.2.3. Kohn-Sham Ansatz

Since the interacting many-body system obeying the hamiltonian 2.53 is difficult to solve, the ansatz of Kohn and Sham(Kohn and Sham, 1965) assumes that the ground state density of the interacting system is equal to that of chosen non-interacting system. This leads to independent-particle equation that is soluble with all the difficult terms are

gathered in the exchange and correlations functionals. The density of N interacting-particle can be written as

$$n_0(\mathbf{r}) = N \int d^3\mathbf{r}_1 d^3\mathbf{r}_2 \dots d^3\mathbf{r}_N |\Psi_0(\mathbf{r}_1, \mathbf{r}_2, \dots, \mathbf{r}_N)|^2 \quad (2.57)$$

When we apply the assumption, the effective density becomes

$$n(\mathbf{r}) = N \sum_{i=1}^N |\psi_i(\mathbf{r})| \quad (2.58)$$

and the kinetic energy of the independent-particle system is

$$T_s = -\frac{\hbar^2}{2m_e} \sum_{i=1}^N |\nabla\psi_i|^2 \quad (2.59)$$

In addition, the classical Coulomb interaction of the independent-particle $n(\mathbf{r})$ with itself, the Hartree term, is defined as

$$E_{Hartree}[n] = \frac{1}{2} \int d^3\mathbf{r} d^3\mathbf{r}' \frac{n(\mathbf{r})n(\mathbf{r}')}{|\mathbf{r} - \mathbf{r}'|} \quad (2.60)$$

Then we can rewrite total energy of the interacting system by using the Kohn-Sham (KS) assumption

$$E_{KS} = T_s[n] + \int d^3\mathbf{r} V_{ext}(\mathbf{r}) + E_{Hartree}[n] + E_{XC}[n] + E_{II} \quad (2.61)$$

where $E_{XC}[n] = \langle T \rangle - T_s[n] + \langle V_{int} \rangle - E_{Hartree}[n]$. The many-body terms are incorporated into the exchange-correlation functional $E_{XC}[n]$. This means that the energy E_{XC} can be expressed as

$$E_{XC}[n] = \int d^3\mathbf{r} n(\mathbf{r}) \epsilon_{XC}([n], \mathbf{r}) \quad (2.62)$$

where $\epsilon_{XC}([n], \mathbf{r})$ is an energy per electron at point \mathbf{r} .

2.2.4. Functionals of Exchange and Correlations

As mentioned in previous section, the Kohn-Sham approach provides the soluble independent-particle equation by collecting the difficult terms into exchange-correlation functional, $E_{XC}[n]$, which can be approximated as a local or nearly local functional of the density. Local density approximation (LDA or local spin density approximation (LSDA))

is commonly used and successful functional in which the exchange-correlation energy density is assumed to be the same as that of homogeneous electron gas.

$$\begin{aligned} E_{XC}^{LSDA}[n^\uparrow, n^\downarrow] &= \int d^3\mathbf{r} n(\mathbf{r}) \epsilon_{XC}^{hom}(n^\uparrow(\mathbf{r}), n^\downarrow(\mathbf{r})) \\ &= \int d^3\mathbf{r} n(\mathbf{r}) [\epsilon_X^{hom}(n^\uparrow(\mathbf{r}), n^\downarrow(\mathbf{r})) + \epsilon_C^{hom}(n^\uparrow(\mathbf{r}), n^\downarrow(\mathbf{r}))] \end{aligned} \quad (2.63)$$

As a further step over the LDA, the exchange-correlation energy can be assumed to be write in terms of not only the density itself but also gradient of the density at a given point. The exchange-correlation functional is defined by Generalized-gradient approximation (GGA)(Perdew and Burke, 1996) as

$$\begin{aligned} E_{XC}^{GGA}[n^\uparrow, n^\downarrow] &= \int d^3\mathbf{r} n(\mathbf{r}) \epsilon_{XC}(n^\uparrow, n^\downarrow, |\nabla n^\uparrow|, |\nabla n^\downarrow|, \dots) \\ &\equiv \int d^3\mathbf{r} n(\mathbf{r}) \epsilon_X^{hom}(n) F_{XC}(n^\uparrow, n^\downarrow, |\nabla n^\uparrow|, |\nabla n^\downarrow|, \dots) \end{aligned} \quad (2.64)$$

where F_{XC} is dimensionless and $\epsilon_X(n)$ is the exchange energy of the unpolarized electron gas. There are widely used successful forms of GGA such as Perdew, Burke, and Ernzerhof (PBE)(Perdew *et al.*, 1996), Perdew and Wang (PW91)(Perdew and Wang, 1992), and Becke (B88)(Becke, 1988) which differ in form of F_{XC} .

2.3. Many Body Effects and Excited States

Despite the success of LDA and GGA in describing the exchange and correlation interactions and resulting electronic band dispersion of structures, electronic and optical bandgap values are mostly underestimated. Since simple Kohn-Sham eigenvalues give inaccurate quasiparticle energy spectrum for the structure, Kohn-Sham DFT can not explain properly the phenomena which include electronic excitations like photoemission or photoabsorption since the Kohn-Sham(Onida *et al.*, 2002). However, quite reliable results can be obtained by using beyond-DFT approaches such as HSE, GW and BSE.

One of the deficiencies of DFT arises from local exchange functionals, that give smaller ionization potential and electron affinity values. To solve this systematical error one can use hybrid functionals such as HSE; the short range part of the exchange term is defined as a mixture of exact short-range exchange from the Fock theory and semilocal long-range exchange of GGA. It was shown that nonlocal potentials generated by HSE functionals accurately describe the band gap of semiconductors(Heyd *et al.*, 2003).

Although the GGA+HSE and LDA+HSE methods are successful in finding electronic bandgap, inclusion of the self energy of the electron (*i*GW) is essential for cases in which the screening effects are large. This can be done by using the GW approximation (Fuchs *et al.*, 2007; Shishkin and Kresse, 2007, 2006; Shishkin *et al.*, 2007) where *G* and *W* stand for the single particle Green's function and the screened Coulomb interaction, respectively. Briefly, the self energy of a particle is the energy which originates from the disturbance on the environment by the particle itself, and the particle with its disturbance is the quasiparticle (QP). There are several methods to calculate the QP energies, such as the G_0W_0 (single shot for the *G* and *W*), GW_0 (several iterations over the *G* and no iterations over the *W*), *GW* (several iterations over the *G* and *W*) as well as the scGW (fully self-consistent). These methods are implemented in softwares ABINIT (Gonze *et al.*, 2009), Yambo (Marini *et al.*, 2009), BerkeleyGW (Deslippe *et al.*, 2012), QuantumEspresso (Giannozzi *et al.*, 2009), and VASP (Kresse and Hafner, 1994, 1993; Kresse and Furthmüller, 1996a,b).

2.3.1. Quasiparticle Energies

The quasiparticle states can be calculated solving following equation which is written in the GW approximation

$$(T + V_{ext} + V_{Hartree}) \psi_{n\mathbf{k}}(\mathbf{r}) + \int d^3\mathbf{r}' \Sigma(\mathbf{r}, \mathbf{r}', E_{n\mathbf{k}}^{\text{QP}}) \psi_{n\mathbf{k}}(\mathbf{r}) = E_{n\mathbf{k}}^{\text{QP}} \psi_{n\mathbf{k}}(\mathbf{r}). \quad (2.65)$$

As mentioned before *T*, *V_{ext}*, and *V_{Hartree}* are kinetic energy, *e*-ion interaction potential, and Coulomb potential between electrons, respectively. The wavefunctions $\psi_{n\mathbf{k}}(\mathbf{r})$ are calculated at DFT levels (LDA or GGA). New term, Σ , represents the self-energy operator,

$$\Sigma(\mathbf{r}, \mathbf{r}', \omega) = \frac{i}{4\pi} \int_{-\infty}^{\infty} e^{i\omega\delta} G(\mathbf{r}, \mathbf{r}', \omega + \omega') W(\mathbf{r}, \mathbf{r}', \omega') d\omega' \quad (2.66)$$

where *G* is known as single particle Green's function,

$$G(\mathbf{r}, \mathbf{r}', \omega) = \sum_n \frac{\psi_n(\mathbf{r}) \psi_n^*(\mathbf{r}')}{\omega - E_n + i\eta \text{sgn}(E_n - \mu)} \quad (2.67)$$

and *W* is the screened Coulomb interaction,

$$W(\mathbf{r}, \mathbf{r}', \omega) = \frac{e^2}{4\pi\epsilon_0} \int d\mathbf{r}'' \frac{\epsilon^{-1}(\mathbf{r}, \mathbf{r}'', \omega)}{|\mathbf{r} - \mathbf{r}''|}. \quad (2.68)$$

The quasiparticle eigenstates can be calculated by writing diagonal matrix elements of Eqn. 2.65

$$E_{nk}^{\text{QP}} = \mathbf{Re} \left[\left\langle \psi_{nk} \left| T + V_{ext} + V_{Hartree} + \Sigma(E_{nk}^{\text{QP}}) \right| \psi_{nk} \right\rangle \right] \quad (2.69)$$

This can be solve iteratively by using Newton-Raphson method which can be formulated as

$$E_{nk}^{\text{QP}} \leftarrow E_{nk}^{\text{QP}} + Z_{nk} \mathbf{Re} \left[\left\langle \psi_{nk} \left| T + V_{ext} + V_{Hartree} + \Sigma(E_{nk}^{\text{QP}}) \right| \psi_{nk} \right\rangle - E_{nk}^{\text{QP}} \right] \quad (2.70)$$

where Z is normalization factor which is calculated as

$$Z_{nk} = \left(1 - \mathbf{Re} \left[\left\langle \psi_{nk} \left| \frac{\partial}{\partial \omega} \Sigma(\omega) \right|_{E_{nk}^{\text{QP}}} \right| \psi_{nk} \right\rangle \right] \right) \quad (2.71)$$

The iteration starts from the eigenvalues of DFT level.

2.3.2. Excitonic States

The inclusion of screening effects is sufficient to obtain the accurate electronic structure of a material. However, to obtain accurate optical spectrum, such as absorption and photoluminescence, the excitonic states must be taken into account. Because, in the optical excitation mechanism, an electron usually makes a bound state with a hole rather than moving back-and-forth between the QP states. Furthermore, considering only the excitations between the QP states underestimates the strength of the low energy excitations and overestimates the high energy excitations. Therefore, the Bethe-Salpeter equation (BSE)(Salpeter and Bethe, 1951; Albrecht *et al.*, 1998; Rohlfing and Louie, 1998) must be solved for the two-particle Green's function of electron-hole pairs. The BSE is expressed in terms of the wave functions and energies that are obtained from the QP calculation. Before writing the corresponding equations explicitly, we can use more convenient notation for simplicity(Rohlfing and Louie, 1998):

$$|v\mathbf{c}\mathbf{k}\rangle \equiv \hat{a}_{v\mathbf{k}}^\dagger \hat{b}_{\mathbf{c}\mathbf{k}+\mathbf{Q}}^\dagger |0\rangle \quad (2.72)$$

where $|0\rangle$ is the ground state, $\hat{a}_{v\mathbf{k}}^\dagger$ and $\hat{b}_{\mathbf{c}\mathbf{k}+\mathbf{Q}}^\dagger$ quasi-electron and quasi-hole creation operators, respectively. \mathbf{Q} represents the momentum of the absorbed photon which is considered as zero at optical excitation regime as mentioned in part 2.1.3. By using the $|v\mathbf{c}\mathbf{k}\rangle$'s as a basis, the excited state $|S\rangle$ can be written as:

$$|S\rangle = \sum_{\mathbf{k}} \sum_v^{hole} \sum_c^{elec} A_{v\mathbf{c}\mathbf{k}}^S \hat{a}_{v\mathbf{k}}^\dagger \hat{b}_{\mathbf{c}\mathbf{k}+\mathbf{Q}}^\dagger |0\rangle \quad (2.73)$$

where $A_{v\mathbf{c}\mathbf{k}}^S$ is the electron-hole amplitude and corresponding excitation energy is Ω_S . Then we can determine these by solving the BSE:

$$\left(E_{c,\mathbf{k}+\mathbf{Q}}^{\text{QP}} - E_{v,\mathbf{k}}^{\text{QP}}\right) A_{v\mathbf{c}\mathbf{k}}^S + \sum_{v',c',\mathbf{k}'} \langle v\mathbf{c}\mathbf{k} | K^{eh} | v',c',\mathbf{k}' \rangle A_{v'c'\mathbf{k}'}^S = \Omega_S A_{v\mathbf{c}\mathbf{k}}^S \quad (2.74)$$

The term K^{eh} stands for the electron-hole interaction. It is significant point that to solve such two-particle equation need excessive computational effort which is an obstacle. After solving the BSE, the frequency dependent dielectric function can be written in the form of(Rohlfing and Louie, 2000)

$$\epsilon_2(\omega) = \frac{16\pi e^2}{\omega^2} \sum_S \left| \frac{\vec{P}}{|\vec{P}|} \cdot \left\langle 0 \left| \frac{i}{\hbar} [H, \mathbf{r}] \right| S \right\rangle \right|^2 \delta(\omega - \Omega_S) \quad (2.75)$$

where \vec{P} is the polarization of the absorbed photon.

2.4. Computational Methodology

This section introduces the general computation methodology which we used to study systems considered and discussed in following chapters. The details for the particular system is given in the corresponding chapter. Our investigations on the structural, mechanical, electronic, and optical properties of the ultra-thin materials considered were carried out using the Vienna ab-initio simulation package VASP(Kresse and Hafner, 1993, 1994; Kresse and Furthmüller, 1996b,a) which is based on density functional theory (DFT). The VASP code solves the Kohn-Sham equations(Kohn and Sham, 1965) iteratively for a system with periodic boundary conditions using plane-wave basis set. In order to describe the electron exchange and correlation, the Perdew-Burke-Ernzerhof (PBE) form of the generalized gradient approximation (GGA) was adopted(Perdew *et al.*, 1996, 1997). The hybrid DFT-HSE06 functional(Heyd *et al.*, 2003) on top of GGA was used for a more accurate estimation of the band gap, since GGA usually underestimates the band gap of semiconducting systems. The spin-orbit interaction, which is essential for some materials, was included in the calculations. The van der Waals (vdW) forces which is important for layered materials was taken into account by using the DFT-D2 method of Grimme(Bučko *et al.*, 2010; Grimme, 2006). To obtain the charge distribution on the structures, Bader technique was used(Henkelman *et al.*, 2006; Bader and Molecules, 1990). The vibrational properties were calculated for a large supercell of the considered structures using the small displacement methodology(Alfè, 2009). The stability of the

structures were also examined by performing ab-initio molecular dynamics (MD) calculations in some cases.

We also calculated the cohesive energy (E_{coh}), which was formulated as $E_{coh} = [(\sum_i n_i E_i) - E_T] / \sum_i n_i$ where i stands for the atoms which contract the structure; n_i , E_i , and E_T are the number of i atom in the unit cell, the energy of free i atom, and the total energy per unit cell. The work functions, which is the energy need to remove an electron from the system, were obtained by subtracting calculated Fermi energy from the calculated vacuum energy.

Structural optimizations were performed by using following parameters. The energy cutoff of the plane-wave basis set was taken to be 500 eV for all calculations. In order to minimize the total energy, the energy difference between the sequential steps was set to 10^{-5} eV. The convergence for the total Hellmann-Feynman forces in the unitcell was taken to be 0.05 eV/Å. In addition, Gaussian smearing factor of 0.05 eV was used for non-self-consistent calculations and the pressures on the unit cell were decreased to a value less then 1.0 kB in all three directions. For the determination of accurate charge densities, Brillouin Zone integration was performed using sufficiently dense Γ -centered k -point samplings.

CHAPTER 3

TESTS

DFT-based optical property calculations, especially when the excitonic states are considered, are in their early stage. Although DFT, GW-approximation, and BSE were demonstrated many years ago, the literature of field confines to the last decade as given in the introduction part. One of the reasons is that the calculation including many-body effects and two-particle excitations needs considerable computational resource to have reliable results in the acceptable time interval. The improvement in the technology provides faster computers, however the need for powerful computers are still bottleneck of the field. Therefore, if one attempts to perform DFT-based optical property calculation, the capability of computational resource must be tested. In the first part of this chapter, we give results of the tests for memory (RAM) usage and time cost for several parameters. In the second part, the results of the test for convergence of the parameters and for accuracy of the optical spectrum are given.

We use single- and few-layer MoS₂ as a test material which is a well-known 2D semiconductor. The structural optimization calculations were previously performed by using the methodology given in Sec. 2.4. The test calculations were carried out using a machine having 64-core processors (CPU MHz:2500.238) with 256 GB memory which is a considerably high memory for usual machine.

3.1. Computational Resource Tests

In this section, we aim to give brief results for investigate the limits of the computational resource that we have, we perform several test calculations.

In Table 3.1, we give results for number of atoms, energy cutoff value for the plane-waves, and k -point sampling in terms of RAM usage for both total and per number of core used and in terms of time cost. The bold character in Table 3.1 refers to tested parameters. We consider a single-, 2-, and 3-layer MoS₂ having 3, 6, 9 atoms in the unitcell, respectively. The vacuum spacing between sequential layer(s) in the neighboring unitcell is considered to be ~ 20 Å. In the optical properties calculations of VASP including the excitonic effects over the GW approximation, computationally the most expensive part

is the step that performs the exact diagonalization of the independent partial hamiltonian (ALGO = Exact) which is essential just before the GW-type calculation. Therefore, we extract the RAM usages and and time costs for “ALGO = Exact” step.

Table 3.1. Table of the results of test calculations. The test parameters are given in bold character.

number of atoms	ENCUT (eV)	number of cores	k -point sampling	RAM (GB)	RAM (GB per core)	Time (h)
3	400	4	$6 \times 6 \times 1$	33.4	8.3	9.9
3	400	16	$6 \times 6 \times 1$	35.7	2.2	3.4
3	400	32	$6 \times 6 \times 1$	41.9	1.3	2.0
3	300	32	$3 \times 3 \times 1$	9.4	0.3	0.2
3	400	32	$3 \times 3 \times 1$	17.0	0.5	0.5
3	500	32	$3 \times 3 \times 1$	24.9	0.8	1.2
3	300	32	$4 \times 4 \times 1$	13.4	0.4	0.3
3	400	32	$4 \times 4 \times 1$	23.5	0.7	0.9
3	500	32	$4 \times 4 \times 1$	36.5	1.1	1.7
3	300	32	$6 \times 6 \times 1$	21.5	0.7	0.4
3	400	32	$6 \times 6 \times 1$	41.9	1.3	2.0
3	400	32	$3 \times 3 \times 1$	17.0	0.5	0.5
6	400	32	$3 \times 3 \times 1$	21.1	0.7	1.0
9	400	32	$3 \times 3 \times 1$	30.5	1.0	1.8
9	400	32	$6 \times 6 \times 1$	88.2	2.8	6.7
9 (\vec{v}_\perp lower)	400	32	$6 \times 6 \times 1$	17.9	0.6	0.0
3	400	32	$3 \times 3 \times 1$	17.0	0.5	0.5
3	400	32	$6 \times 6 \times 1$	41.9	1.3	2.0
3	400	32	$9 \times 9 \times 1$	80.7	2.5	3.8
3	400	32	$12 \times 12 \times 1$	135.6	4.2	7.0
3	400	32	$15 \times 15 \times 1$	197.8	6.2	-

In first part of Table 3.1, the tests for the number of cores are given. When we use 4-, 16-, and 32-core, the increase in the total RAM usage is very slow and the RAM usage per core decreases and seems that it converge to ~ 1.0 GB. On the other hand, the time cost decreases fast when the number of cores increases as expected.

In the second part of Table 3.1, the energy cutoff value of the plane-waves is tested and given for different k -point samplings. The RAM requirement is increases, however the increment is enhanced significantly for higher k -points.

In the third part of Table 3.1, the number of atom is chanced by adding layer to

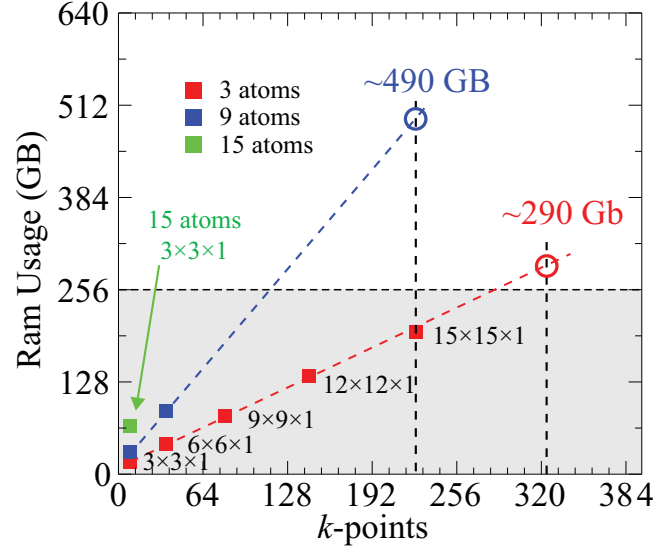


Figure 3.1. The number of k -points vs the RAM usage. The red, blue and green squares represents 3- (1L-), 9- (3L-), and 15-atom (5L-) MoS_2 systems. The grey region show the available RAM (256 GB) of the machine that is used for tests. The red and circle at the crossing of the dashed lines show the predictions of the RAM requirements when 1L MoS_2 for k -point sampling of $18 \times 18 \times 1$ and 3L MoS_2 for k -point sampling of $15 \times 15 \times 1$ are calculated.

system and in the perpendicular direction of the plane of the layer, the unitcell vector is kept constant. The RAM usage increases almost linearly which is a similar to that in the energy cutoff test.

In the fort part of Table 3.1, we give the results for tests of k -point sampling, which is also essential for the accuracy of the results, in the case that the energy cutoff of plane-wave is set to be 400 eV for 3-atom unitcell (single-layer). When we consider the total number of k -points in the Brillouin Zone the increase in the total RAM usage linear and fast such that it reaches to 197.8 GB which a close value to the total memory of the machine that we use. It seems that that any larger k -point sampling, such as $18 \times 18 \times 1$, needs memory exceeding 256 GB. This is an unfortunate result because the convergence of the calculated optical spectrum is also very sensitive to Brillouin Zone sampling which we discuss in the following section.

In Fig. 3.1, the RAM usage for different k-point samplings are used for the prediction of possible RAM usage of larger systems. We consider that the linear relation between the k -point sampling and RAM usage in the single-layer MoS_2 is valid for larger

k -point sampling and also for the 9-layer system, then we predict the possible RAM usage for both single-layer with k -points of $18 \times 18 \times 1$ and 9-layer with k -points of $15 \times 15 \times 1$ which are ~ 290 and ~ 490 GB, respectively, which exceed 256 GB RAM of the machine we use. As shown in Fig. 3.1, the RAM usage of 9-layer MoS₂ is predicted to increase faster than that of single-layer and exceed the 256 GB for lower k -point sampling than $12 \times 12 \times 1$. It should be noted that these results are for VASP package and as mentioned before, there are other program packages, such as YAMBO (Marini *et al.*, 2009) and BerkeleyGW (Deslippe *et al.*, 2012), that focus on the many-body effects and excited states. These program packages also provide reliable results and are used in valuable studies. Even so the need for computational resources is much more larger than that for usual DFT calculations.

3.2. Qualitative Tests for Parameters

In the previous section, we focused on the computational requirements for the optical property calculations using VASP package. In this section, we aim to show an example for obtaining the accurate optical spectra compatible with the experimental results. To do this, we perform several test calculations to have convergence in several parameters such as the k -point sampling, the vacuum spacing, and energy cutoff of the plane-wave basis set. As a test material, we consider single-layer MoS₂. We check the convergence of a parameter by the position of the first peak after inclusion of the many-body and excitonic effect, DFT+GW+BSE. The control parameters are considered as follows; the energy cutoff is taken to be 400 eV; the number of bands is set to 96 in the DFT part. The excitonic states are calculated by considering 2 occupied bands at the top of the valence band and 2 empty bands at the bottom of the conduction band. Because of the computational burden, we do not include spin-orbit interaction into the test calculations.

3.2.1. Effect of k -point sampling

The k -point sampling is an inevitable parameter for obtaining an accurate optical spectra. In Fig. 3.2, The imaginary part of the frequency dependent dielectric function, which mostly correspond to the absorption spectrum, and the first peak position in the energy axis are given for different k -point sampling. The vector perpendicular to the plane of the structure is taken to be 10 \AA . The energy cutoff of the plane-wave basis in the

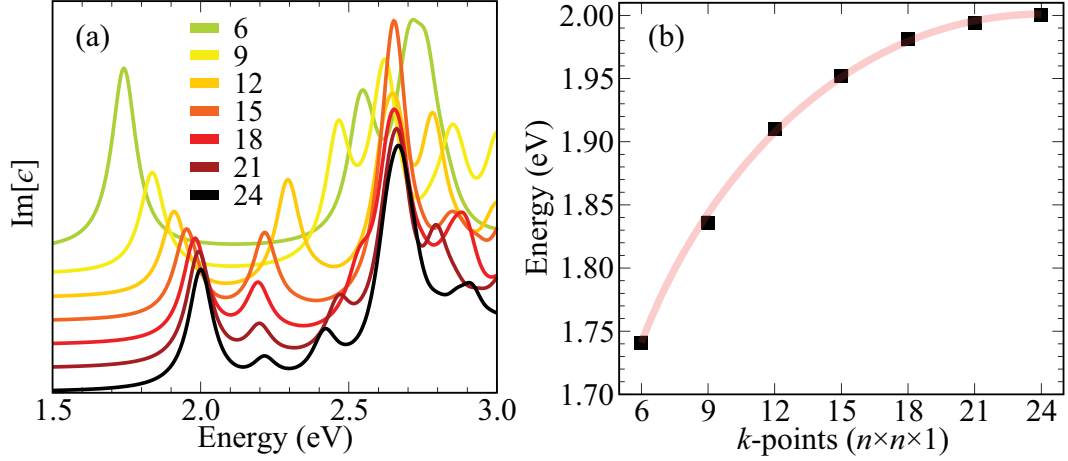


Figure 3.2. (a) The imaginary part of the dielectric function for different k -point samplings. For simplicity the sampling of $n \times n \times 1$ is represented as single number of n . (b) The excitation energy of the first excitonic peak for different k -point. The light-red curve is for tracking the convergence.

GW calculation is considered to be 100 eV.

First of all, the spectra is shifted and also the dispersion changes as the samplings increases. In particular, the second peak as well as the subsequently apparent third peak, which are unexpected peaks, diminish by increasing k -point sampling. These peaks are not consistent with the experimental spectrum. However they resemble the peaks vanishing after the inclusion of electron-phonon interaction and discussed in the study Qiu et al (Qiu *et al.*, 2013). As shown in Fig. 3.2 (b), the first peak converge to ~ 2.0 eV. The peak position difference between those of $18 \times 18 \times 1$ and $24 \times 24 \times 1$ is calculated to be ~ 15 meV which is fairly small. Therefore we can conclude that for the single-layer MoS_2 $18 \times 18 \times 1$ k -points is sufficient for having convergent optical spectra.

3.2.2. Effect of vacuum spacing

One of the most important parameter for the accuracy of the calculation is the vacuum spacing considered in the non-periodic direction, in other word, in the perpendicular direction to the plane of 2D structure. Even if one treats a 2D system, 3D scheme is constructed by using a supercell having additional vacuum region to consider the system as finite in particular direction. This brings an artifact which originates from the long range

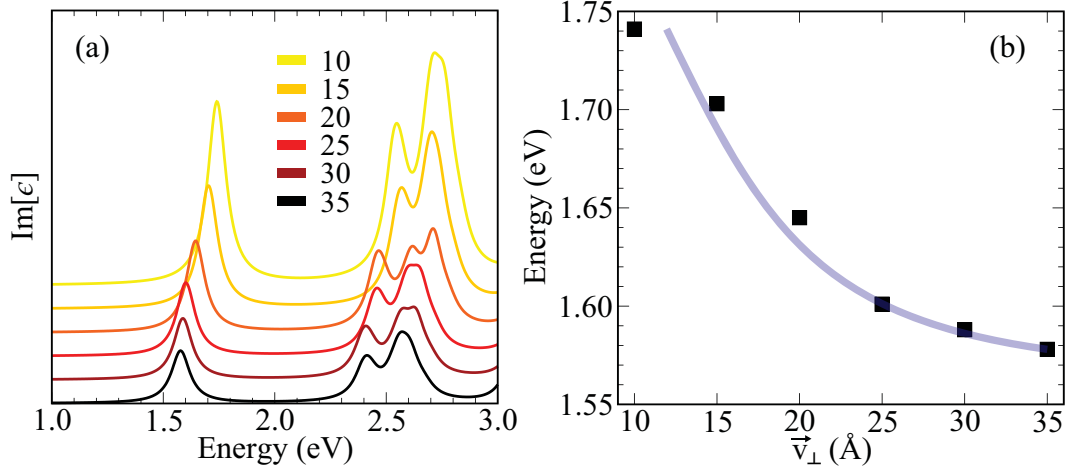


Figure 3.3. (a) The imaginary part of the dielectric function for different out-of-plane vector lengths. (b) The excitation energy of the first excitonic peak for different out-of-plane vector lengths. The light-blue curve is for tracking the convergence.

Coulomb interaction between the periodic replicas of the system in the direction that is considered to be non-periodic. This is important in the self-energy, GW, and exciton property, BSE, calculations. It should be noted that there is an analytical method (Rozzi *et al.*, 2006), the Coulomb cutoff technique, which was proposed and then implemented to several program packages such as YAMBO (Marini *et al.*, 2009) and BerkeleyGW (Deslippe *et al.*, 2012), to overcome the long range Coulomb interaction. Yet, to best of our knowledge, the Coulomb cutoff technique has not been implemented to VASP package. Therefore, we perform test calculations for different vacuum spacings to minimize these unintentional interactions.

In the test calculations, the energy cutoff of the plane-wave basis in the GW calculation is considered to be 100 eV as in the tests for the k -point sampling. In Fig. 3.3, we show the imaginary part of the dielectric function and the position of the first peak in the energy axis for different vector lengths. As shown in Fig. 3.3 (a), the spectrum is redshifted and the dispersion does not change significantly. The reduction in the peak sizes is because the formula contains unitcell volume as a denominator. In the Fig. 3.3 (b), it seems that the first peak position converges to ~ 1.58 eV and the energy difference between the values of 25 and 35 Å is ~ 20 meV. Therefore, it is considerable that the vector length of 30 Å gives convergent spectra.

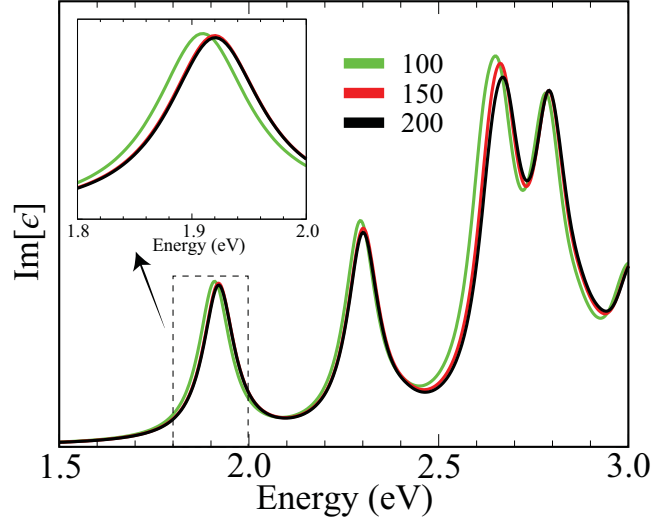


Figure 3.4. The imaginary part of the dielectric function for different energy cutoff of the response function in GW approximation. The first peak of the spectrum is zoomed and shown in the inset.

3.2.3. Effect of energy cut-off

The energy cutoff is the parameter that should be tested for structural optimization and electronic properties. Once an accurate results for electronic properties are obtained, the optical transition can be calculated accurately. In the calculation of the quasiparticle levels by using VASP, i.e. GW procedure, the energy cutoff of the response function can also be controlled via the tag of “ENCUTGW“ and should be tested. Here, the results of energy cutoff the response function are given in Fig. 3.4.

During the test calculations, the k -point sampling is set as $12 \times 12 \times 1$ and the unit-cell vector perpendicular to the structural plane is taken to be 10 \AA which is considerably low. As shown in Fig. 3.4, the spectrum converges fast and almost the same when the cutoff is set to 150 and 200 eV. Then we can conclude that the for the single-layer MoS_2 system, taking ”ENCUTGW“ as 150 eV is sufficient to have convergent spectrum.

In conclusion, we tested both the suitability of computational resources and the computational parameter for accurate optical spectrum on single-layer MoS_2 as test material by performing DFT-based calculation using VASP. Firstly, it is shown that the machine having 64-core with 256 GB memory, which is considerably powerful machine, is barely sufficient for complete the calculations. Secondly, an acceptable accuracy of the

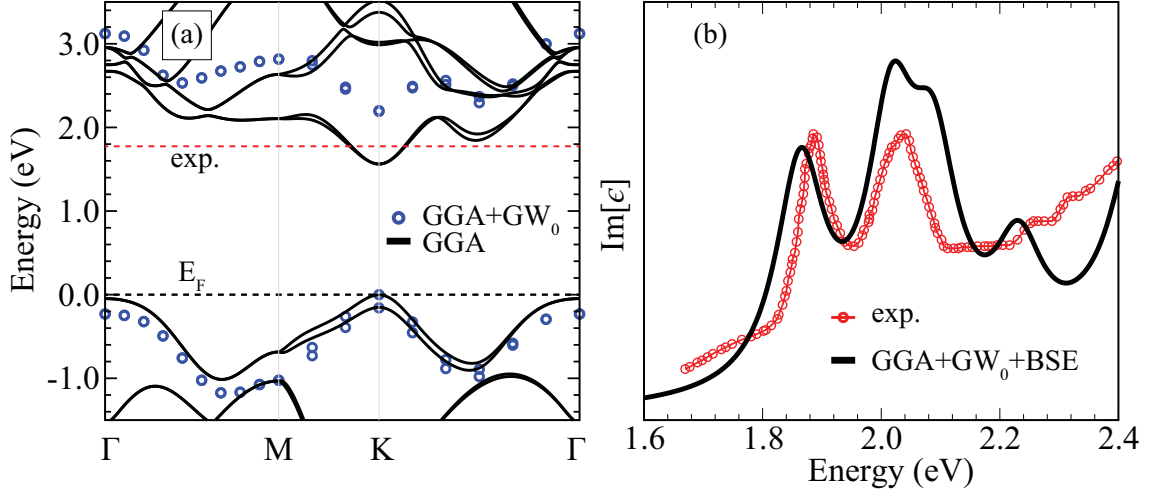


Figure 3.5. (a) The electronic band structure of single-layer MoS₂. Black curve is the GGA result. The blue circles are the quasi particle states at given path for highest two and lowest two bands of the VB and CB, respectively. (b) Imaginary dielectric function of single-layer MoS₂. The black curve is our calculated result and the red curve with circle is the experimental result from report of Mak et al(Mak *et al.*, 2010).

optical spectrum is obtained by performing test calculations of the parameters. It is found that the single-layer MoS₂ system needs at least $18 \times 18 \times 1$ k -point sampling with 25 Å out-of-plane vector as shown in Fig. 3.5. The other parameters do not have significant role on the spectrum according to our calculations.

To summarize, the theoretical background of the light-matter interaction and the basics of the DFT and beyond-DFT methods are overviewed. In addition, the computational requirement for ordinary calculation of the optical property and the accuracy of the optical spectrum of the single-layer MoS₂ system are tested. In the following chapters, the applications of the given theories and the techniques are presented in several studies which are recently published as scientific articles. In the first section gives the DFT application of the novel ultra-thin materials, the second one focuses to the optical properties of the novel ultra-thin materials, and the third section gives mainly experimental studies, which are assisted by DFT-based calculations, on ultra-thin materials in use.

CHAPTER 4

HEXAGONAL AlN

Bulk structures of III-V semiconductors have been widely studied due to their importance for technological applications such as blue light-emitting diodes, lasers operating in the blue and the ultraviolet regime, high temperature diodes and transistors (Yeh *et al.*, 1992b,a; Vurgaftman *et al.*, 2001; Miwa and Fukumoto, 1993; Christensen and Gorczyca, 1994; Morkoç *et al.*, 1994). In addition, technological advances lead to the emergence of novel low-dimensional forms of III-V binary compounds. Experimental fabrication of AlN nanowires (Zhao *et al.*, 2005; Wu *et al.*, 2004; Li *et al.*, 2006; Duan *et al.*, 2005), nanobelts (Yu *et al.*, 2011; Wu *et al.*, 2003; Tang *et al.*, 2007) and nanodots (Goh *et al.*, 2011; Bouchkour *et al.*, 2011) have already been reported. In recent years, theoretical and experimental studies of graphene (Novoselov *et al.*, 2004) provided a wide range of knowledge for a new class of materials and have opened up possibilities for the synthesis of many similar structures such as; silicene (Sahin *et al.*, 2013; Liu *et al.*, 2013; Kara *et al.*, 2012; Cahangirov *et al.*, 2009), germanene (Yang *et al.*, 2014; Ni *et al.*, 2012; Dàvila *et al.*, 2014; Cahangirov *et al.*, 2009), transition metal dichalcogenides (TMDs) (Gordon *et al.*, 2002; Novoselov *et al.*, 2005; Coleman *et al.*, 2011; Tongay *et al.*, 2012; Wang *et al.*, 2012; Sahin *et al.*, 2013; Ross *et al.*, 2014; Tongay *et al.*, 2014) and hexagonal structures of III-V binary compounds (e.g. *h*-BN, *h*-AlN) (Şahin *et al.*, 2009; Farahani *et al.*, 2009; Kim *et al.*, 2012; Wang *et al.*, 2009; Zhuang and Hennig, 2012). Among the binary compounds, after single-layer BN, AlN is currently a material of much interest due to its semiconducting nature and its large bandgap which is suitable for device applications.

Following the first theoretical study on the stability of hexagonal AlN reported by Sahin *et al.* (Şahin *et al.*, 2009), successful experimental realization of hexagonal AlN phase was achieved very recently by Tsipas *et al.* (Tsipas *et al.*, 2013). In the early study of Du *et al.*, energetic and electronic properties of one-dimensional AlN nanostructures such as nanowires with hexagonal cross sections, double- and triple-walled faceted nanotubes and single-walled faceted AlN nanotubes were investigated (Du *et al.*, 2012). Between the first theoretical prediction and the experimental realization of *h*-AlN, other groups have also focused on this material. Zheng *et al.* (Zheng *et al.*, 2010) predicted that zigzag AlN nanoribbons have an indirect bandgap whereas armchair AlN nanoribbons have a direct bandgap, and these bandgaps monotonically decrease with increasing ribbon width.

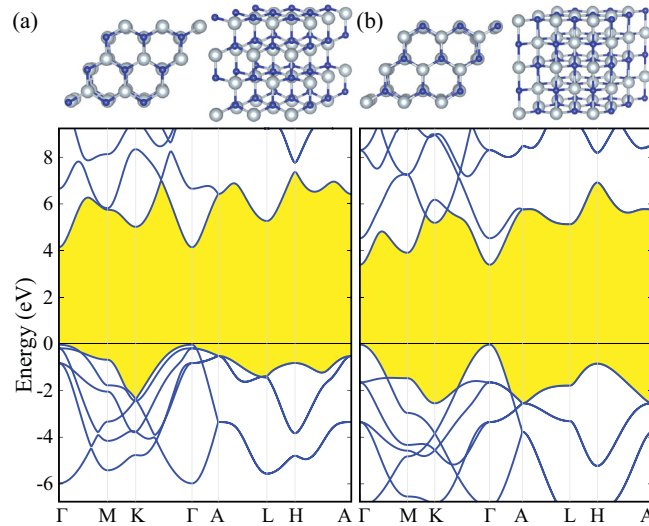


Figure 4.1. Top and tilted-side views of atomic structures of bulk (a) wurtzite and (b) hexagonal AlN (top panel). Their electronic band dispersion (lower panel).

Almeida *et al.* (de Almeida *et al.*, 2012) studied the energetics and electronic properties of typical defects in a *h*-AlN network such as vacancies, anti-sites and impurities. It was shown that defects such as N vacancies and Si impurities lead to the breaking of the planar symmetry of the *h*-AlN sheet and significant changes in the band structure in the vicinity of the Fermi level. In addition, Chen *et al.* systematically investigated the electronic structure of armchair and zigzag AlN, GaN nanoribbons and investigated also the electronic properties of AlN/GaN nanoribbon heterojunctions. They found that the bandgap of both nanoribbons decrease monotonically as the ribbon widths increase and that the bandgap of the nanoribbon heterojunctions are closely related to the AlN/GaN ratio (Chen *et al.*, 2013). Shi *et al.* calculated the magnetic properties of undoped and transition metal (TM) doped AlN nanosheets by using first-principles calculations. They reported that AlN nanosheet is nonmagnetic, whereas a single *3d* TM atom can bring about large local magnetic moments in TM-doped AlN nanosheets (Shi *et al.*, 2014).

Motivated by the recent study of Tsipas *et al.* (Tsipas *et al.*, 2013) reporting the formation of stable *h*-AlN phases at the early stages of AlN growth, we aim to address the following experimental observations: (i) modification in electronic valence band structure, (ii) relatively large lattice parameter that was reported as an indication of *h* phase, (iii) reduction in band gap in comparison with bulk wurtzite, and (iv) dynamical stability of *h*-AlN.

Our study reveal(Bacaksiz *et al.*, 2015) that the synthesized *h*-AlN, although it has structural similarities, electronically displays different characteristics from *h*-BN and TMDs. As well as weak van der Waals (vdW) interactions, ionic character of the interlayer interactions plays an important role in the electronic properties of multilayered *h*-AlN. Therefore, while monolayers of *h*-BN and TMDs are direct band gap semiconductors, *h*-AlN has an indirect band gap. In addition, upon dimensional reduction from bulk to bilayer energy the band gap decreases like as was found for *h*-BN and TMDs.

4.1. Structures of Bulk AlN

First we briefly overview the characteristics of wurtzite and recently synthesized *h*-AlN before the extensive investigation of the number of layer dependent properties of *h*-AlN are undertaken. At ambient conditions, AlN crystallizes in a wurtzite (*wz*) structure that belongs to the $P6_3mc$ space group. As shown in Table 4.1, PBE approximation gives the following structural parameters $a = 3.11 \text{ \AA}$ and $\frac{c}{a} = 1.61$. In the *wz* structure of AlN each Al-N bond is formed by $2.35 e^-$ charge donation from Al to N atom and therefore it has a highly ionic character. In parallel with the abundance of the *wz* form of AlN in nature, among the possible bulk structures *wz* is the energetically most favorable one. The electronic dispersion shown in Fig. 4.1 indicates that *wz*-AlN is a semiconductor with a 4.2 eV direct bandgap at the Γ point.

Table 4.1. Calculated lattice parameter in the lateral direction a and lattice parameter in the vertical direction c , the distance between layers d_{LL} , the intralayer atomic distance between Al and N atoms d_{Al-N} , the charge transfer from Al atom to N atom $\Delta\rho$, the cohesive energy E_{coh} and the energy bandgap of the structure E_{gap} . (d) and (i) indicate direct and indirect bandgap, respectively.

	a (\AA)	c (\AA)	d_{LL} (\AA)	d_{Al-N} (\AA)	$\Delta\rho$ (e)	E_{coh} (eV)	E_{gap} (eV)
Bulk <i>wz</i> -AlN	3.11	5.01	-	1.90	2.35	6.14	4.2 (d)
Bulk <i>h</i> -AlN	3.30	4.15	2.08	1.90	2.37	6.02	3.4 (d)
2L <i>h</i> -AlN	3.20	-	2.13	1.85	2.32	5.73	3.5 (i)
1L <i>h</i> -AlN	3.13	-	-	1.81	2.28	5.36	2.9 (i)

In addition to some early theoretical predictions(Şahin *et al.*, 2009) the stability of the hexagonal phase of AlN (*h*-AlN) was proven by a very recent experimental study.(Tsipas *et al.*, 2013) Regarding the less layered structures or surfaces of wurtzite materials, transformation from wurtzite to a graphite-like structure that allows the removal of destabilizing dipoles is energetically more favorable.(Freeman *et al.*, 2006a) This graphite-like hexagonal structure of AlN belongs to the $P6_3/mmc$ space group. The layered planar structure has two atoms in the unitcell which has lattice vectors $\mathbf{v}_1 = a(\frac{1}{2}, \frac{\sqrt{3}}{2}, 0)$, $\mathbf{v}_2 = a(\frac{1}{2}, -\frac{\sqrt{3}}{2}, 0)$ and $\mathbf{v}_3 = c(0, 0, 1)$ where $|\mathbf{v}_1| = |\mathbf{v}_2|$. Atomic coordinates are $(\frac{|v_1|}{3}, \frac{|v_1|}{3}, 0)$ and $(\frac{2|v_1|}{3}, \frac{2|v_1|}{3}, 0)$, for first and second type of atoms respectively. We considered that the layers are AA' stacking (deciding the stacking of layers is explained in Section IV-B) which is shown in Fig. 4.1 (b). And we found that the lattice constant is $a = 3.30 \text{ \AA}$ and the distance between layers is $c = 2.08 \text{ \AA}$ which is smaller when compared to graphite and *h*-BN ($\sim 3.33 \text{ \AA}$ and $\sim 3.30 \text{ \AA}$ for graphite(Baskin and Meyer, 1955; Chung, 2002) and *h*-BN(Marini *et al.*, 2006; Paszkowicz *et al.*, 2002; Shi *et al.*, 2010), respectively). Intralayer atomic distance between Al and N atoms is 1.90 \AA . This is the same as for *wz*-AlN. The cohesive energies are given in Table 4.1.

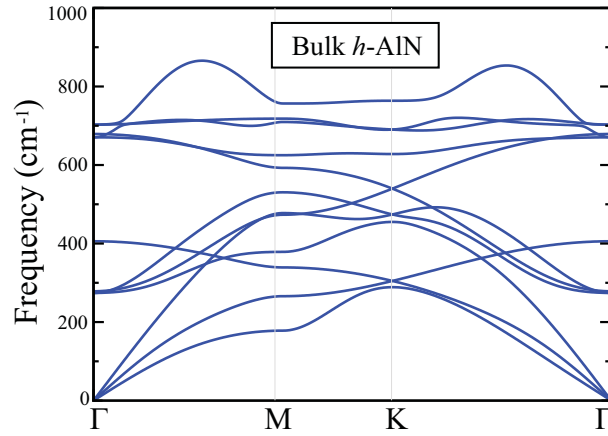


Figure 4.2. Phonon dispersion of bulk *h*-AlN.

As shown in Fig. 4.1 (d), layered *h*-AlN is a direct bandgap semiconductor which has 3.4 eV bandgap with band edges located at the Γ point. Therefore, our results confirm the experimentally reported bandgap reduction(Tsipas *et al.*, 2013) in *h*-AlN compared to bulk *wz*-AlN. At the top of the VB, there is a single parabolic band for holes and the main contributions are from the p_z orbital of N atoms. The bottom of the CB, there is a single parabolic band and most of the states come from p_x orbital of N atoms. Final charges of

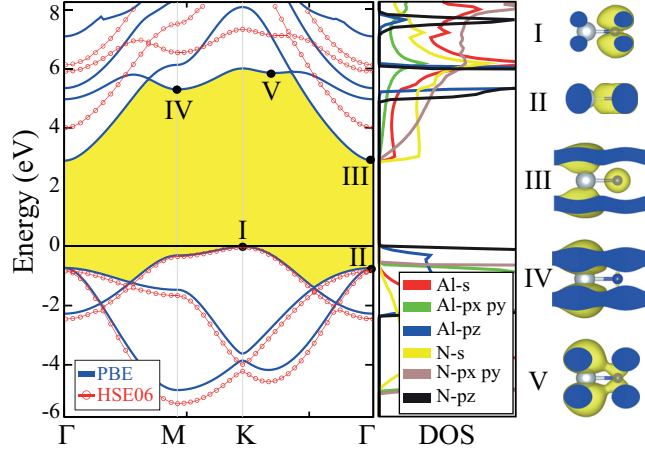


Figure 4.3. Monolayer h -AlN band diagram within PBE and HSE06 (left panel), partial density of states (middle panel) and the band decomposed charge densities of the band edges (right panel). Sections of 3D charge density that represent the connection to the neighboring cells are filled with blue color.

Al and N atoms are $0.63 e^-$ and $7.37 e^-$, respectively. Therefore, $2.37 e^-$ charges are transferred from Al to N atom. Following section is devoted to the understanding of the characteristics of monolayer h -AlN and the nature of the inter-layer interactions.

Lastly, we analyze vibrational properties of the h -AlN phase by calculating the phonon spectrum in whole Brillouin Zone (BZ) using the small displacement methodology (Alfè, 2009) for 32-atomic supercell. As shown in Fig. 4.2 phonon spectrum of h -AlN displays real eigenfrequencies in the whole BZ. Therefore, there is no doubt on the dynamical stability of the h -AlN structure. Here we also see that differing from its h -BN counterpart the optical and acoustical modes couple with each other at certain points in the BZ. In the case of h -AlN, there are 4 atoms per primitive unit-cell and 12 phonon branches. The first three are acoustical phonon modes, the phonon branch at 274 cm^{-1} is a doubly degenerate rigid layer shear mode, known as low-energy E_g mode, involving the out-of-phase motion of atoms in adjacent planes. In addition, the highly dispersive phonon modes with eigenvalues 406 and 679 cm^{-1} at the zone center correspond to out-of-phase motion of Al and N atoms in adjacent layers. Interestingly, the contribution of the second atom type in these modes are negligibly small. The highest optical mode, doubly degenerate at the Γ point, have the E_g symmetry and therefore it is expected to be measured in Raman experiments.

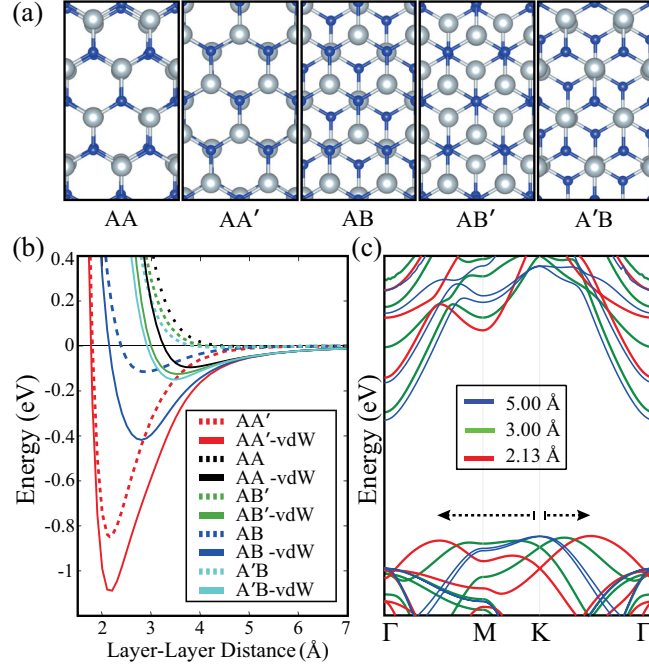


Figure 4.4. (a) Possible stackings between two layers of h -AlN. (b) Layer-layer interaction energy for different stackings. (c) Interlayer spacing dependent band dispersion of AA' stacked two layers of h -AlN.

4.2. Monolayer, Bilayer and Few Layer h -AlN

Monolayer h -AlN: The first prediction of the dynamical stability and electronic properties of single-layers of h -AlN and similar III-V compounds were first reported by Sahin *et al.* (Sahin *et al.*, 2009). Monolayer hexagonal structure belongs to the space group $P6_3/mmc$ with unit vectors $\mathbf{v}_1 = a(\frac{1}{2}, \frac{\sqrt{3}}{2}, 0)$, $\mathbf{v}_2 = a(\frac{1}{2}, -\frac{\sqrt{3}}{2}, 0)$ where $|\mathbf{v}_1| = |\mathbf{v}_2|$. In this configuration the atomic coordinates are given as $(\frac{|v_1|}{3}, \frac{|v_1|}{3}, 0)$ and $(\frac{2|v_1|}{3}, \frac{2|v_1|}{3}, 0)$ for first and second type of atoms, respectively. We calculated that the lattice constant of monolayer h -AlN is 3.13 Å and the distance between Al and N atoms is 1.81 Å which is the lowest value when compared with bulk forms and bilayer structure as seen from Table 4.1. These results are in good agreement with the measured lattice parameters (3.13 Å) of epitaxially grown of h -AlN, at early stages, by Tsipas *et al.* (Tsipas *et al.*, 2013). The cohesive energy of monolayer h -AlN is the lowest among the possible phases. It is also seen that the amount of charge transfer from Al to N slightly decreases from bulk to monolayer h -AlN.

Fig. 4.3 illustrates the band diagrams, density of states and also the 3D charge densities of states at the band edges for monolayer h -AlN. Differing from bulk h -AlN which has a direct bandgap at the Γ , the VBM of the monolayer is at the K point and the CBM is at the Γ point, therefore monolayer h -AlN is an indirect bandgap insulator with 2.9 eV bandgap. It is also seen that bare-GGA and DFT-HSE06 approximated electronic band dispersions shown in Fig. 4.3 are almost the same. With DFT-HSE06 hybrid functional, h -AlN is an indirect bandgap material with a bandgap of 4.06 eV. It is also noteworthy to mention that h -BN is the counterpart of AlN with a direct bandgap at the K point.

Right panel of Fig.4.3 shows that the bonding states at VBM (label I) are mainly composed of N- p_z orbitals and the degenerate state, with lower energy, at the Γ point (label II) stems from hybridized p_x and p_y orbitals. In addition, the CBM located at the Γ point has a quadratic-like dispersion (label III) and the relevant charge density is in the form of surface state. Therefore, the conduction electrons in single-layer h -AlN display free-electron-like behavior. Moreover the anti-bonding states with higher energy at the M and the K points are composed by mainly Al and slightly N states together.

Bilayer h -AlN and Layer-layer Interaction: During the growth of lamellar materials prediction of the most preferable stacking sequence is of importance. To determine the stacking order of bilayer AlN, we examined five possible (see Fig. 4.4 (a)) stacking types: AA (Al over Al and N over N), AA' (Al over N and N over Al), AB (Al over N and N over center of hexagon), A'B (Al over Al and N over center of hexagon), AB' (N over N and Al over center of hexagon).

To determine the interaction strength and interlayer interaction profile of above-mentioned stacking orders of bilayer h -AlN, total energies were calculated as a function of layer-layer distance. As seen in Fig. 4.4 (b), the largest interlayer coupling energy and shortest interlayer distance is obtained for AA' type stacking. Therefore AA' stacking corresponds to the ground state stacking order. It is also seen that the vdW correction to the interaction energy is ~ 250 meV per unitcell. In addition, for AA' stacking, layer-layer distance is 2.13 Å which is the minimum value among all stacking combinations. Here it appears that due to the presence of surface states interlayer distance in bilayer h -AlN is slightly larger than that of bulk h -AlN. However, compared to graphite(Baskin and Meyer, 1955; Chung, 2002) and h -BN(Marini *et al.*, 2006; Paszkowicz *et al.*, 2002; Shi *et al.*, 2010), and their bilayer forms, h -AlN has a smaller interlayer distance. The lattice parameter, 3.20 Å, which is the maximum value of all stacking combinations that slightly differs from the value obtained by self-correlation analysis of the experimental

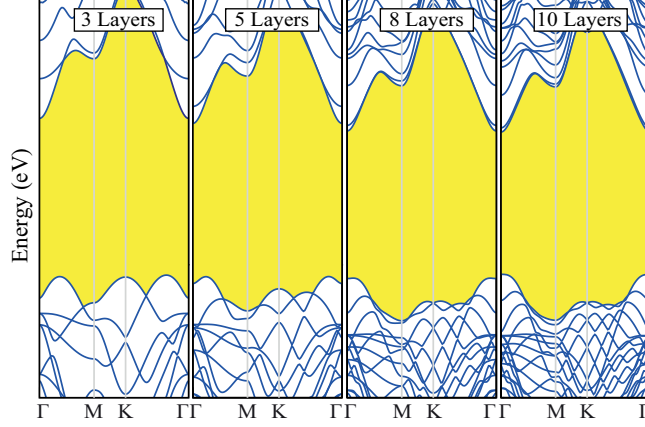


Figure 4.5. Evolution of electronic band dispersion of N -layer h -AlN.

data (3.14 ± 0.06) for few layers. This slight disagreement can be understood from the effect of the Ag(111) substrate.

Moreover, in Fig. 4.4 (c), we analyze how the electronic band dispersion of AA'-stacked bilayer is modified with varying interlayer distance. Negligibly interacting, weakly interacting and highest interaction (ground state) cases are illustrated using layer-layer distances of 5.00, 3.00 and 2.13 Å, respectively. The band diagram of negligibly interacting case resembles the electronic structure of monolayer h -AlN. However, when the layers start to interact, for instance in the weakly interacting case (delineated by green lines in Fig. 4.4 (c)), the top of the VBM are shifted towards the Γ zone center. When the interlayer distance reaches its optimum position, one of the VBM appears at $K - \Gamma$ while the other one is located at $M - \Gamma$. Interestingly, the location of CBM in BZ is independent from the interlayer distance. Hence from monolayer to bilayer, the indirect character is conserved and the bandgap is changed from 2.9 to 3.5 eV.

Few Layer h -AlN: Synthesis of stable ultra-thin h -AlN structures, sub-monolayer to 12 layers, was demonstrated by Tsipas *et al.* (Tsipas *et al.*, 2013), recently. Our first-principles total energy optimization calculations revealed that lamellar hexagonal structure of N -layered ($N = 1, 2, \dots$) AlN is a stable phase. As shown in Figs. 4.5 and 4.6, planarity of the few-layered structures is preserved, except the negligible buckling at the surface layers, while electronically few layer h -AlN is significantly different from monolayer one.

In order to illustrate how the electronic structure evolves with increasing number

Table 4.2. Calculated direct and indirect transition energies between the VB and CB edges of single to ten layered structures.

	$\Gamma \rightarrow \Gamma$	$K \rightarrow \Gamma$	$\Gamma M \rightarrow \Gamma$	$K\Gamma \rightarrow \Gamma$	E_{coh}
1L AlN	3.62	2.92	-	-	5.36
2L AlN	4.29	-	3.61	3.53	5.73
3L AlN	4.05	3.58	3.57	3.53	5.82
4L AlN	3.79	-	3.51	3.50	5.86
5L AlN	3.61	3.73	3.46	3.46	5.89
6L AlN	3.48	-	3.41	3.41	5.92
7L AlN	3.38	3.77	3.35	3.35	5.93
8L AlN	3.33	-	3.30	3.30	5.94
9L AlN	3.27	3.81	3.26	3.26	5.95
10L AlN	3.22	-	-	-	5.96

of layers we present the band dispersion of 3, 5, 8 and 10-layered h -AlN in Fig. 4.5. Here there are several interesting trends that is worth to note: (i) the energy of the conduction band edge at the K point decreases with increasing number of layers, (ii) states at conduction band edge which have surface state character remain unchanged. The energy difference between the band edges VBM(K) and CBM(Γ) increases from 2.92 eV for monolayer to 3.81 eV for 10-layer h -AlN, and (iii) the most significant influence of additional number of layers is on the bonding states forming the valence band maximum at the ΓM and the ΓK points. It appears that due to the strong interlayer interaction each additional layer shifts these band edges towards the zone center. This gradual shift of VB edges continues up to 10 layers. Upon the formation of the 10th layer h -AlN structure reaches the bulk limit and it becomes a direct band gap semiconductor. Increasing the thickness furthermore has no influence on the electronic properties of N -layered h -AlN and they are direct bandgap (3.22 eV for ten layered) materials like bulk h -AlN. As given in detail in Table 4.2, transition energies between the points converge asymptotically to values of bulk h -AlN. Increasing the number of layers, cohesive energies converge to that of bulk h -AlN. It appears that only few layer h -AlN structures with thickness $N > 11$ are suitable for lasing device applications. Here calculated modifications in electronic structure explains and supports the experimental findings of Tsipas *et al.* (Tsipas *et al.*, 2013).

However, the evolution of the VBM with changing number of layers requires further attention. In Fig. 4.6 we present the 3D charge density of the electronic states located

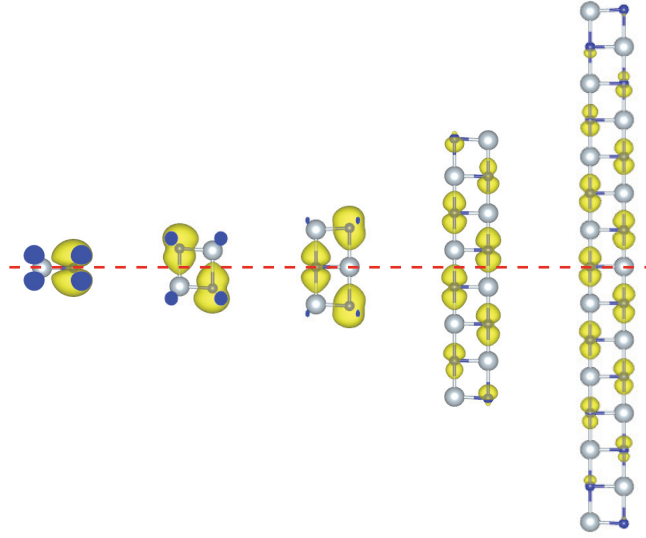


Figure 4.6. The evolution of the bonding charge density of h -AlN for monolayer, bi-layer, 3-layer, 8-layer and 15-layer. Sections of 3D charge density that represent the connection to the neighboring cells are filled with blue color.

at the VBM. It is clearly seen that the character of the bonding state (VBM) is modified monotonically with increasing number of layers. With increasing number of layers the hybridization between N- p_z states is weakened. In addition, due to the mild buckling the interaction of the surface states which have sp^3 -like character and N- p_z states vanishes at the vicinity of the upper- and the lower-most layers. Therefore for enough thick h -AlN materials, which is found to be larger than 10-layers, the electronic structure is mainly determined by uniformly distributed N- p_z states and hence the structure behaves like a bulk material having a direct bandgap at the Γ symmetry point.

4.3. Conclusions

Using first principles methodology, we investigated the thickness dependent electronic properties of layered hexagonal AlN (Bacaksiz *et al.*, 2015). First, we showed that the bulk structure of hexagonal AlN is a semiconductor with a direct bandgap at the Γ point. Phonon spectrum analysis of this structure reveals two Raman-active modes at 274 and 703 cm^{-1} . Here, the lattice parameter of h -AlN, which is larger than the wurtzite phase, agrees with the experiment of Tsipas *et al.* (Tsipas *et al.*, 2013) that reports the for-

mation of hexagonal regions at the early stages of the growth process. Next, the formation of multilayer structures and most favorable stacking order were investigated via total energy calculations. It is seen that, similar to the hexagonal BN counterpart, among the possible stacking orders, AA' type stacking is the most favorable. It is worthwhile to note that the interlayer interaction is larger compared to similar layered materials with hexagonal lattice symmetry. Differing from some other two-dimensional crystal structures such as graphite, *h*-BN and TMDs, here the ionic interlayer interaction is dominant between the *h*-AlN layers. Therefore, for the synthesis of *h*-AlN the epitaxial growth technique performed by Tsipas *et al.* (Tsipas *et al.*, 2013) appears more suitable than mechanical exfoliation.

Subsequently, the evolution of the electronic structure of *N*-layered *h*-AlN was investigated for structures with 1 – 15 layers. It is seen that unlike bulk *h*-AlN, monolayer *h*-AlN has an indirect bandgap where VBM and CBM are at the *K* and the Γ points, respectively. Moreover, it is seen that upon the formation of additional layers valence band edges gradually shift towards the Brillouin Zone center. Such a modification of the valence band states is in good agreement with the experiment of Tsipas *et al.* (Tsipas *et al.*, 2013) It was also calculated that the few layered structures reach the bulk limit and their electronic properties remains almost unchanged after the formation of 10 layers. Therefore, structures thicker than 10 layers, exhibits a direct band gap of 3.22 eV at the Γ point. We believe that easy synthesis and the presence of a thickness-dependent bandgap crossover in few-layered hexagonal AlN structures are very important for novel device applications.

CHAPTER 5

HYDROGENATION OF SINGLE LAYER PbI_2

Recent research efforts have been directed towards not only synthesis of graphene-like materials, but also towards the functionalization of existing ultra-thin crystal structures. These recent studies have revealed some important results such as (i) tunable bandgap opening in graphene(Şahin *et al.*, 2009; Sofo *et al.*, 2007; Elias *et al.*, 2009; Flores *et al.*, 2009; Sahin *et al.*, 2010; Sahin and Ciraci, 2011) (ii) H-defect-induced magnetization of graphane(Şahin *et al.*, 2009; Zhou *et al.*, 2009), (iii) band gap engineering in silicene and germanene(Houssa *et al.*, 2011; Voon *et al.*, 2010; Wang *et al.*, 2012), (iv) stability enhancement in h-BN(Cabria *et al.*, 2006), (v) tunable magnetic features in TMDs(Pan, 2014; Shi *et al.*, 2013b).

One of the most recently synthesized single-layer semiconductor is lead iodide (PbI_2). In bulk PbI_2 , which is a member of metal halides family, van der Waals stacked individual layers are in the form of octahedral T-phase. As a precursor material for lead iodide perovskites, given by the general formula of $\text{CH}_3\text{NH}_3\text{PbI}_{3-n}\text{X}_n$ ($\text{X}=\text{Cl}, \text{Br}$), PbI_2 has been used in many different device applications(Green *et al.*, 2014; Guo *et al.*, 2015; Jeng *et al.*, 2013; Lee *et al.*, 2012; Tan *et al.*, 2014). Recently, by performing the optical measurements and first-principles calculations of bulk and few-layer PbI_2 , Toulouse *et al.* showed that exciton binding energy dramatically increases with a decreasing number of layers(Toulouse *et al.*, 2015). In addition, the synthesis of the monolayer PbI_2 within the carbon nanotubes was reported by Cabana et al(Cabana *et al.*, 2014). In a recent work, Zhou *et al.* investigated the structure, stability, electronic and optical properties of the monolayer PbI_2 and also the hetero-bilayer form with graphene by using first principles calculations(Zhou *et al.*, 2015). However, to our knowledge, the interaction between hydrogen (H) atom and the surface of monolayer PbI_2 and how the physical properties are effected under hydrogenation are still open questions.

In this study, using first principles calculations based on density functional theory (DFT), we investigate the interaction of hydrogen atoms with bare single-layer PbI_2 (Bacaksiz and Sahin, 2016). We also focus on structural and electronic properties of half- and fully-hydrogenated monolayers of PbI_2 . We found that the T-phase is energetically more favourable than H-phase and it is an indirect semiconductor. Our investigation revealed that the chemical functionalization by both half- and full-hydrogenation cause reconstruc-

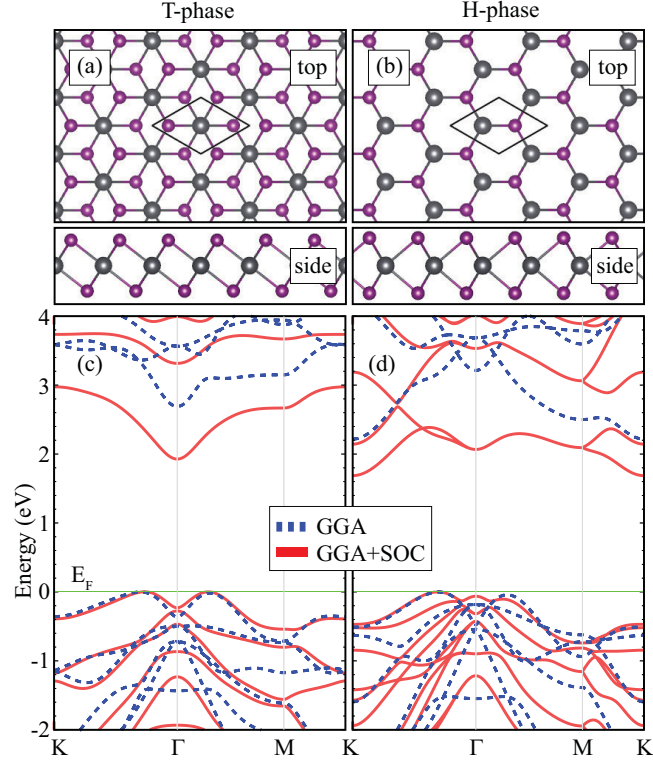


Figure 5.1. (a) and (b) illustrate the structure of monolayer 1T and 1H PbI_2 , respectively. (c) and (d) are the corresponding band structures where the blue and red curves represent the GGA and GGA+SOC, respectively. The Fermi level (E_F) is given by green solid line.

tion in the structure of monolayer PbI_2 and lead to significant reduction in the band gap of the structure. Such a hydrogen-driven reconstruction in monolayers of PbI_2 have not been reported before.

5.1. H and T Phases of Single Layer PbI_2

Similar to TMDs, monolayer PbI_2 can form two different phases, octahedrally coordinated 1T and trigonal-prismatic coordinated 1H. As shown in Fig. 5.1, both phases have three trigonal subplanes where the Pb subplane is sandwiched by two I-subplanes. While the 1T phase is a member of the $P\bar{3}m2$ space group where subplanes of it are ABC stacked, the 1H is a member of the $P\bar{6}m2$ space group where subplanes of it are ABA stacked. The lattice vectors of both phases are $\mathbf{v}_1 = a(\frac{1}{2}, \frac{\sqrt{3}}{2}, 0)$, $\mathbf{v}_2 = a(\frac{1}{2}, -\frac{\sqrt{3}}{2}, 0)$ where $|\mathbf{v}_1| = |\mathbf{v}_2|$ and a is the lattice constant. The atomic coordinates of 1T phase are

Table 5.1. Calculated parameters for monolayer PbI_2 are the lattice constant in the lateral direction, a ; the atomic distance Pb and I atoms, $d_{\text{Pb-I}}$; the charge transfer from Pb to I atom, $\Delta\rho$; the work function Φ ; and the cohesive energy, E_c . E_g^{GGA} and $E_g^{\text{GGA+SOC}}$ are the energy band gap values within GGA and GGA+SOC, respectively.

	a (Å)	$d_{\text{Pb-I}}$ (Å)	$\Delta\rho$ (e^-)	Φ (eV)	E_c (eV)	E_g^{GGA} (eV)	$E_g^{\text{GGA+SOC}}$ (eV)
1T PbI_2	4.44	3.23	0.9	5.96	2.76	2.69	1.93
1H PbI_2	4.32	3.26	0.8	6.05	2.70	2.22	1.68

$(\frac{|v_1|}{2}, \frac{|v_1|}{2}, 0)$, $(\frac{|v_1|}{6}, \frac{|v_1|}{6}, \frac{c}{2})$, and $(\frac{5|v_1|}{6}, \frac{5|v_1|}{6}, -\frac{c}{2})$ for the Pb and two I atoms, respectively, where c is the distance between the subplanes of I atoms. The atomic coordinates of 1H phase are given as $(\frac{|v_1|}{3}, \frac{|v_1|}{3}, 0)$, $(\frac{2|v_1|}{3}, \frac{2|v_1|}{3}, \frac{c}{2})$, and $(\frac{2|v_1|}{3}, \frac{2|v_1|}{3}, -\frac{c}{2})$.

Lattice constants of the optimized crystal structures of 1T and 1H phases are 4.44 Å and 4.32 Å, respectively. However, as shown in Table 5.1, interatomic distance $d_{\text{Pb-I}}$ of T-phase (3.23 Å) is found to be shorter than H-phase (3.26 Å). Total energy calculations also reveal that the 1T phase is 165 meV per unit cell more favourable over the H-phase. The cohesive energies per atom of 1T and 1H phases are 2.76 and 2.70 eV, respectively. These results are consistent with the previous results which showed that the T-phase is the most favourable form of both bulk and monolayer crystals of PbI_2 . In addition, the work-functions (Φ) of 1T and 1H phases are calculated to be 5.96 eV and 6.05 eV, respectively.

We also present electronic energy band dispersions of 1T and 1H phases (approximated by GGA and GGA+SOC) in Figs. 5.1 (c) and (d), respectively. The 1T phase of PbI_2 monolayer has an indirect band gap where the valence band maximum (VBM) is between the K and the Γ symmetry points and the conduction band minimum (CBM) is at the Γ point. As given in Table 5.1, the energy bandgaps of 1T phase are 2.69 and 1.93 eV within GGA and GGA+SOC. Total charge donated by each Pb atom are 0.9 and 0.8 e^- for 1T and 1H phases, respectively. Moreover, the 1H phase has also an indirect band gap where the VBM is between the K and the Γ points and CBM is at the K point. The band gap of 1H phase is calculated to be 2.22 eV within GGA and 1.68 eV within GGA+SOC.

It is seen that although the T and H phases have similar electronic characteristics at the valence band edges which are immeasurable by experimental tools such as ARPES, lattice parameter and the work function is unique feature of each phases. Discussions in

the following chapters will be performed on the 1T-phase that corresponds to the ground state crystalline structure of single-layer PbI_2 .

5.2. Interaction with Single Hydrogen

For engineering the structural, electronic and magnetic properties of a material, surface hydrogenation is an easy and powerful method. From theoretical point of view determination of the interaction between the PbI_2 surface and H atoms is of importance.

For the calculation of adsorption and diffusion characteristics of H atom on the surface of monolayer PbI_2 a 3×3 supercell, which is enough to avoid the interaction between adjacent H atoms, is used. First of all, to determine the most favourable adsorption site of H atom, various initial positions over the surface are calculated; top-Pb site, mid-point of Pb-I bond, the top-I site and the sites in between these points. As shown in Fig. 5.2 (a), adsorption of hydrogen atom in the vicinity of I atom with the bond length of 1.66 Å is much more preferable than adsorption on other lattice points. It is also seen that the formation of tilted I-H bond with the surface leads to slightly out-of-plane relaxation of the underlying I atom. Considering its spin polarized ground state in vacuum, the binding energy of single H atom is calculated to be 0.32 eV which is quite small compared to binding energy of H to graphene (0.98 eV(Sahin and Ciraci, 2012)).

In addition, our Bader charge analysis reveal that bonded H atom preserves its 1.0 e^- , on the other hand, the H bonded I atom has 7.0 e^- in contrast with the other I atoms which have 7.4 e^- . The displaced 0.4 e^- from that particular I atom are shared by the nearest three Pb atoms. Our analysis reveals that the H atom do not form a bond when the vdW term excluded. Therefore, one can conclude the bonding type of H with PbI_2 surface as a weak vdW type bonding.

The single H bonded system have midgap states which originate from H atom. When we consider these states, the band gap is 0.21 eV as shown in Fig 5.2 (c). There is one localized band near the Fermi level which have charge distribution as shown inset of Fig 5.2 (c). The system has a magnetic ground state with magnetic moment of 1.0 μ_B . It also appears that only the states around Fermi level have splitting due to hydrogen-induced magnetism.

To have more general picture of interaction between H atom and the monolayer PbI_2 , we perform the diffusion barrier calculation which is shown in Fig. 5.2 (d). From the top of an I atom to top of its second nearest I atom, the energy difference plot shows that top of I atom possesses the minimum energy. The barrier to escape from the influence

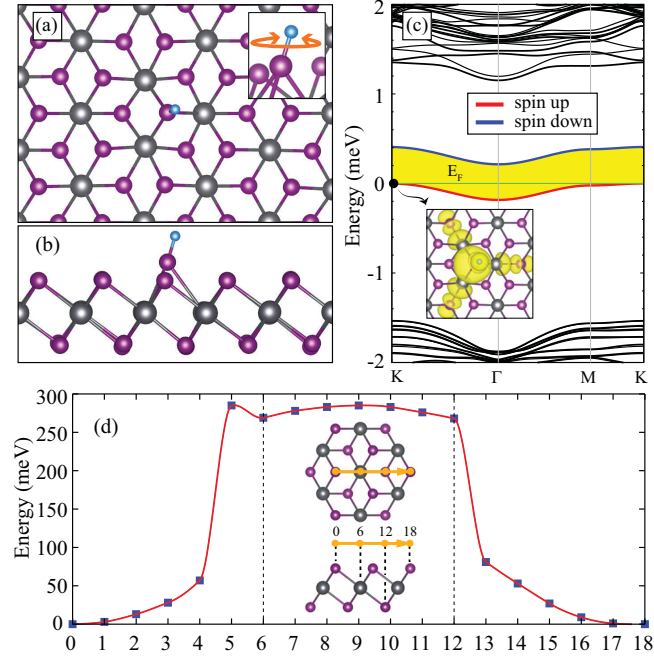


Figure 5.2. (a) and (b) show the structure of H atom adsorbed (3×3) PbI_2 from top and the side, respectively. The inset in (a) illustrates the rotation of H around the I atom. (c) is the band structure of single H atom adsorbed 3×3 PbI_2 monolayer where the blue and red curves represent the spin-different states. Inset shows the charge distribution of VBM at the Γ . (d) is the diffusion barrier plot through the given path. The Fermi level (E_F) is given by green solid line.

of I atom is around 285 meV. There are one local minimum on the path which coincide the center of triangle of I atoms over the Pb atom. In addition, considering the energy plot around the I atom as an harmonic potential, the jump frequency of H atom is estimated to be $\nu \approx 0.191$ GHz. These results are consistent with the MD simulations reveal that at low temperatures (up to 50 K), each single H rotates almost freely around the I atom. Although each H is bonded to underlying I, there is no certain preferable bonding direction with the PbI_2 surface.

5.3. One-side Hydrogenation

Following the analysis of the interaction of H atoms with the surfaces of PbI_2 , in this section, we investigate how the structural, electronic and magnetic properties are

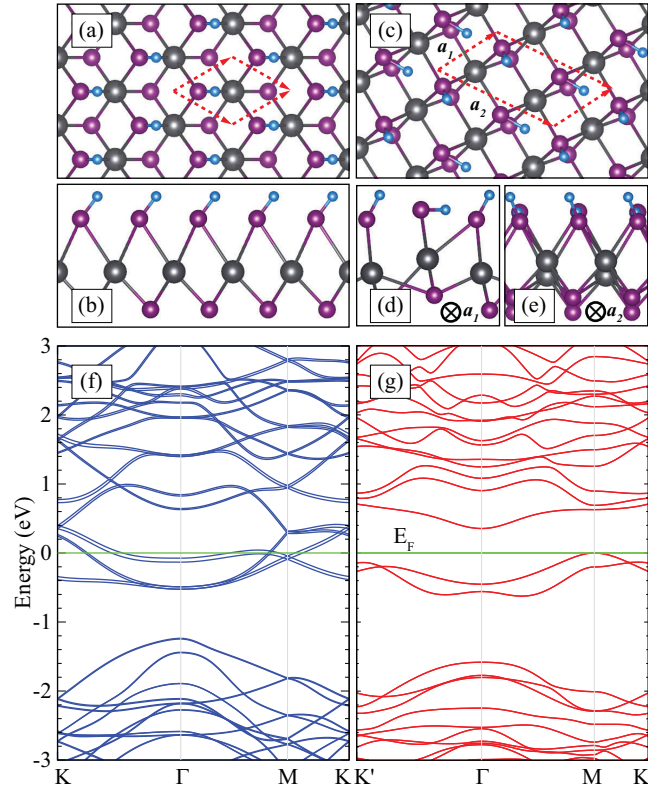


Figure 5.3. The structures in (a) and (b) for perfect hexagonal and (c), (d), and (e) for distorted forms of half-hydrogenated monolayer PbI_2 (half-H- PbI_2), respectively. View direction are given in (d) and (e). (f) and (g) are the corresponding band structures. To compare the perfect and distorted forms, 2×2 unitcells are used for both band structures. The Fermi level (E_F) is given by green solid line.

modified upon the hydrogen coverage of surfaces. Firstly, the half-hydrogenated (half-H- PbI_2), one-by-one hydrogen coverage of each I atom on the same surface, structure is investigated.

As shown in Figs. 5.3 (a) and (b), H atoms form a well-ordered crystal structure (where $\theta=60^\circ$) in the one-side covered structure. The lattice constant of this perfectly hexagonal crystal structure is calculated to be 4.05 \AA . Compared to hydrogen-free bare PbI_2 structure, Pb-I bond length increases from 3.23 to 3.77 \AA at the hydrogenated side. However, at the hydrogen-free side, Pb-I bonds become stronger and the bond length is calculated to be 3.08 \AA . Moreover, alongside with the structural changes, the half-hydrogenation also modifies charge distribution in the crystal structure. Bader charge analysis shows that functionalization cancels charge transfer between Pb and I atoms at

the hydrogenated side and therefore, removes the ionic character of Pb-I bond. In contrast, at the bare side of the half-H-PbI₂, the charge sharing increases where the I and Pb atoms have 7.4 and 3.5 e^- , respectively. Electronically, as shown in Fig. 5.3 (f), the semiconducting character vanishes after hydrogenation and the system turns into a ferromagnetic metal with 0.14 μ_B per unitcell. However, hydrogenation-induced metalization in single-layer PbI₂ requires further analysis.

For further analysis of the half-hydrogenated structure we also perform finite temperature MD calculations. Our calculations showed that starting from very low temperatures (20-25 K) half-H-PbI₂ tends to undergo a structural transformation. Apparently, the perfectly hexagonal half-hydrogenated structure mentioned before corresponds to a local minimum on Born-Oppenheimer surface and for the determination of the ground state structure one needs small perturbation such as temperature. Then, by performing full structural optimization of the distorted structure created by MD calculation, we obtained the real ground state crystal structure of half-H-PbI₂.

As shown in Figs. 5.3 (c) and (d), the ground state of half-H-PbI₂ forms a (2×1) reconstructed surface. It is calculated that this (2×1) reconstructed phase of half-H-PbI₂ is 0.41 eV per unitcell more favourable than the perfectly hexagonal phase which is obtained by a total energy calculation performed at 0 K. In this half-H-PbI₂ structure, there are two bonding types of H atom. One H atom stands over the I atom with an angle of 28.5° with the normal of the structure plane, the other H reclines parallel to the surface at level of the I atoms. The I-H bond lengths for the standing and reclined H atoms are 1.70 and 1.69 Å which are slightly larger than that of perfectly hexagonal phase (1.65 Å). The Pb-I bond length of reconstructed phase is 3.93 Å at the hydrogenated side and the smallest Pb-I bond length is 3.11 Å at the hydrogen-free side. These values are larger than those of perfectly hexagonal phase (3.77 and 3.08 Å, respectively). As given in Table 5.2, the lattice constants are 4.22 and 7.83 Å with an angle of 58.9° and the workfunction at the hydrogenated side is found to be 3.57 eV. On the other side, the H binding energy per H atom is 0.64 eV which is much larger than that of single H on 3×3 supercell ($E_{bind}=0.32$ eV for single H).

The charge distributions of the reconstructed structure are specific for the structurally different Pb, I, and H atoms. In general, with respect to H atom bonding configurations, all atoms have specific charge in (2×1) reconstructed unitcell (see Fig. 5.3 (c), (d), and (e)). Shortly, the standing- and reclining-H atoms have 1.1 and 1.0 e^- ; the I atoms bonded with standing- and reclining-H have 7.0 and 7.1 e^- ; the Pb atoms close to standing- and reclining-H have 3.4 and 3.7 e^- , respectively. On the bare side of the

Table 5.2. Calculated parameters for half- and full-hydrogenated monolayer PbI_2 (half-H- PbI_2 and full-H- PbI_2) are; the lattice constant in the lateral directions, \mathbf{a}_1 and \mathbf{a}_2 ; the angle between the lattice vectors, θ ; the work function Φ ; the cohesive energy, E_c ; the binding energy per H atom, E_{bind} ; the band gap, E_g^{GGA} ; and magnetic moment per primitive cell, μ .

	\mathbf{a}_1 (Å)	\mathbf{a}_2 (Å)	θ (°)	Φ (eV)	E_c (eV)	E_{bind} (eV)	E_g^{GGA} (eV)	μ (μ_B)
half-H- PbI_2	4.22	7.83	58.9	3.57	2.23	0.64	0.35	0.0
full-H- PbI_2	8.29	8.02	63.0	3.73	2.03	0.93	0.76	0.0

half-H- PbI_2 , the I atoms have larger charge of 7.3 and 7.4 e^- which are aligned in z -axis with standing- and reclining-H, respectively

Furthermore, upon the temperature-driven structural transformation from perfectly hexagonal to (2×1) reconstructed phase, not only the structure but also electronic properties are modified dramatically. As shown in Fig. 5.3 (g), the reconstruction removes the metallic property and the system becomes semiconductor with a small band gap of 0.35 eV. The band gap is still indirect in which the VBM and CBM are at M and Γ points, respectively. After the reconstruction the system has a nonmagnetic ground state. This type of distortions are known as Jahn-Teller distortion in which the dangling bonds are filled up and the system transforms from metal to semiconductor. Therefore, semiconducting nature of (2×1) reconstructed phase of half-H- PbI_2 , that corresponds to the ground state structure, is quite important for nanoscale optoelectronic device applications.

5.4. Full Hydrogenation

As well as one-side hydrogenation that may be realized on one-side-supported material, one can also achieve both-side coverage of monolayer PbI_2 (full-H- PbI_2) when it is in freestanding form. Structural analysis of the full-H- PbI_2 is performed by applying the same methodology. MD calculations revealed that the ground state atomic structure of the full-H- PbI_2 is quite different from half-H- PbI_2 .

Similar to half-hydrogenated structure, H-induced reconstructions take place starting from 20-25 K° and therefore three different types of I-H bonds (perpendicular, tilted bond with 44.8°, and the reclined parallel to the surface) are formed over the PbI_2 sur-

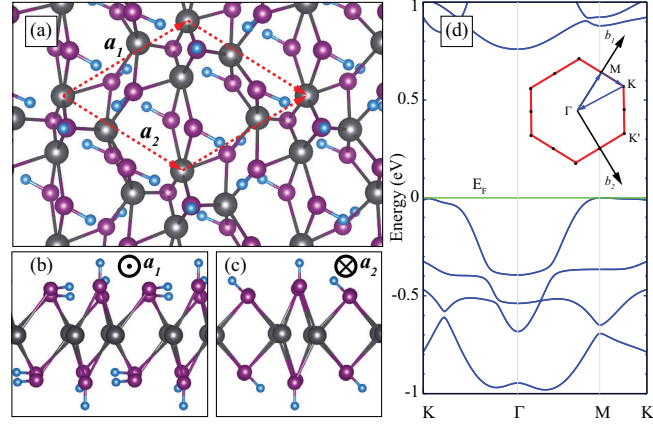


Figure 5.4. (a), (b), and (c) illustrate the structure of full-hydrogenated monolayer PbI_2 from top, side views with the corresponding directions, respectively. (d) is the band structure of full-hydrogenated monolayer PbI_2 . The Fermi level (E_F) is given by green solid line.

face (see Figs. 5.4 (a), (b) and (c)). Then the analysis of fully-optimized crystal structure reveals that the primitive unitcell of full-H- PbI_2 contains a (2×2) reconstructed phase of PbI_2H_2 . In reconstructed structure, the shortest Pb-I bond length is calculated to be 3.60 Å. The I-H bond length is around 1.68 Å which is very close to that of single H adsorbed case. As given in the Table 5.2, lattice parameters of the (2×2) reconstructed structure are calculated to be 8.29 and 8.02 Å with an angle of 63.0° .

Upon full hydrogenation, not only the structure but also work functions, cohesive energies and the H binding energies significantly differ from half-hydrogenated structure. The work function of the full-H- PbI_2 is found to be 3.73 eV. The cohesive energy of the full-H- PbI_2 is calculated to be 2.03 eV smaller than that of half-H- PbI_2 . The calculated average binding energy of an H atom is 0.93 eV which is larger as compared to those of single H and half-hydrogenated cases. Here, it is noteworthy that the larger binding energy is consistent with the slightly larger work function. As shown in Figs. 5.4 (d) the full-H- PbI_2 is a semiconductor with an indirect band gap of 0.76 eV. The VBM and CBM stay at M and Γ points which are similar to those of half-H- PbI_2 . It is also seen that the Jahn-Teller type distortion in the structure removes dangling bonds and therefore the system is converged to non-magnetic semiconducting ground state.

5.5. Conclusions

In this work, we studied the newly emerging ultra-thin PbI_2 which is a member of metal halides (Bacaksiz and Sahin, 2016). Starting from the comparison of two possible monolayer phases, 1T and 1H, interaction with single H atom, half- and full-hydrogenation of monolayer PbI_2 were investigated using first principles DFT calculations. The 1T phase was found to be favourable with the band gap of 2.69 and 1.93 eV within GGA and GGA+SOC, respectively. Our calculations also showed that the H atoms strongly reacts with the PbI_2 surface and further functionalization of its surfaces can be realized. The binding energy was found to be 0.3 eV.

In the case of half-hydrogenation, it was found that the (2×1) Jahn-Teller type distorted ground state structure corresponds to the ground state phase. We showed that reconstruction from perfectly hexagonal structure to 2×1 half-H- PbI_2 leads to dramatical modifications such as (i) metal-to-semiconductor transition (ii) removal of magnetic moments. Moreover, our calculations revealed that full-hydrogenated monolayer PbI_2 forms another (2×2) Jahn-Teller distorted form in its ground state. In that case, the structure, full-H- PbI_2 , was a nonmagnetic semiconductor with a bandgap of 0.76 eV. Our results reveal that hydrogenation is an efficient way to engineer the structural and electronic properties of single-layer PbI_2 .

CHAPTER 6

ANISOTROPIC AND FLEXIBLE ULTRA-THIN ZnSe

The II-VI binary compounds are well-known and have been extensively studied semiconductor structures. Mostly II-VI structures crystallize in the zinc-blende (*zb*) and wurtzite (*wz*) phases, and depending on their size and shape, they exhibit diverse electronic and optical properties (Manna *et al.*, 2003; Murray *et al.*, 1993; Peng *et al.*, 2000; Yin and Alivisatos, 2005). Although, most of the ultra-thin crystals have layered structure in their bulk forms, there are several studies that revealed possibility of synthesis of 2D crystals from non-layered materials of II-VI binary compounds (Ithurria *et al.*, 2011; Ithurria and Dubertret, 2008; Ithurria *et al.*, 2011; Lei *et al.*, 2014; Li and Peng, 2011; Park *et al.*, 2013; Son *et al.*, 2009; Sun *et al.*, 2012, 2013, 2012; Zhang *et al.*, 2013, 2012). Among these studies, Sun *et al.* (Sun *et al.*, 2012) reported the synthesis of monolayer ZnSe. According to their observations, the monolayer ZnSe is ultra-flexible and has a band gap of ~ 3.5 eV. Motivated by this observations, several computational studies were also reported. Tong *et al.* investigated the various compounds having zinc-blende form, comparatively (Tong *et al.*, 2014). They predicted a phase of monolayer ZnSe resembling a slab of the rock-salt crystal (t-ZnSe) and claimed that this phase is energetically more favorable than that observed. In addition, Zhou *et al.* compared different monolayer phases of ZnSe by means of many body perturbation theory on top of density functional theory (Zhou *et al.*, 2015). They also predicted that the t-ZnSe phase is dynamically stable and energetically favorable. More recently, Zhou *et al.* predicted the structural transition from the experimentally observed phase to the t-ZnSe phase under lateral pressure at room temperature by using molecular dynamic simulations (Li *et al.*, 2015).

Although, the computational studies asserted that the synthesized monolayer ZnSe is meta-stable, the dynamical stability and also the mechanical properties are still unknown. Here, using first principles calculations based on density functional theory (DFT), we investigate structural, electronic, and mechanical properties of the synthesized monolayer ZnSe. Our investigation reveals that the monolayer ZnSe is dynamically stable and possesses angle dependent elastic parameters such as in-plane stiffness and Poisson ratio (Bacaksiz *et al.*, 2017).

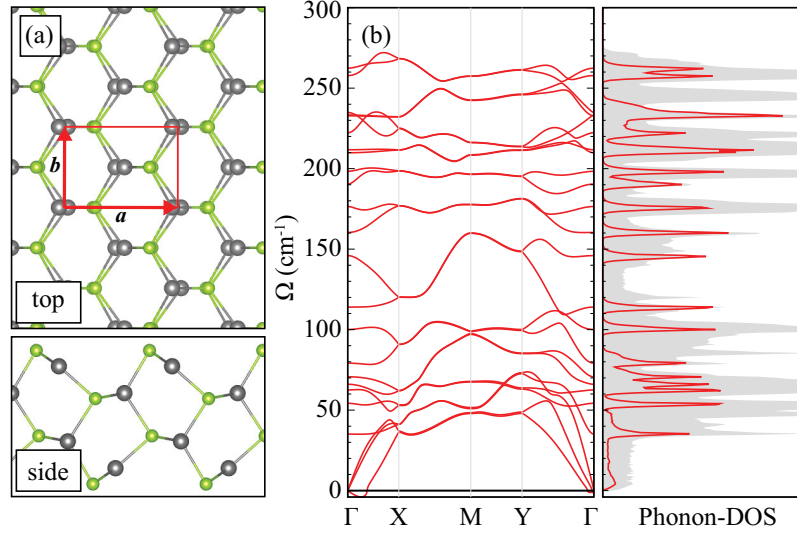


Figure 6.1. (a) The top and side views of monolayer ZnSe. The red vectors stands for unitcell vectors. In panel (b), the phonon band structure and phonon density of states are shown. In Phonon-DOS panel, the total and the Γ projected phonon density of states are shown as grey area and red curve, respectively.

6.1. Structural and Electronic Properties

In this section, we investigate the structural and electronic properties of the monolayer ZnSe. As the experimental observation (Sun *et al.*, 2012) of 4-atom-thick monolayer ZnSe, we truncate 4 Zn-Se sublayers from the bulk *zb*-ZnSe for the initial configuration of the DFT-based structural optimization. As shown in Fig. 6.1 (a), a rectangular unit-cell with 8 atoms is constructed and the lattice parameters are found to be $a = 5.57$ and $b = 3.96$ Å as given in Table 6.1. At the optimized surfaces of the monolayer ZnSe, the outermost Zn and Se atoms are distorted as shown in the side view of Fig. 6.1 (a). The outermost Zn atoms have three coordinating Se atoms with the same bond length of 2.40 Å. The inner Zn atoms have 4 coordinating Se atoms with a tetrahedral type as in bulk crystal but the bond lengths vary between 2.43 and 2.50 Å. These bond lengths are not significantly different from the bulk value of 2.45 Å. The Bader charge analysis reveals that slightly varying bonds exhibit the same charge depletion of $0.7 e^-$ from Zn to S. In addition, the cohesive energy is found to 2.69 eV which slightly differ from the bulk value of 2.84 eV per atom.

Table 6.1. Calculated parameters for monolayer ZnSe are; the lattice constants in the lateral directions, a and b ; the atomic distance between Zn and S atoms, d_{Zn-Se} ; the charge transfer from Zn to Se atom, $\Delta\rho$; and the cohesive energy per atom, E_c . $E_g^{GGA+SOC}$ is the band gap values within GGA+SOC.

	a (Å)	b (Å)	d_{Zn-Se} (Å)	$\Delta\rho$ (e^-)	E_c (eV)	$E_g^{GGA+SOC}$ (eV)
monolayer	5.57	3.96	2.40-2.50	0.7	2.69	1.88
zb -bulk	5.65	-	2.45	0.7	2.84	1.32

After the structural optimization, the dynamical stability of the monolayer ZnSe is also examined. As shown in Fig. 6.1 (b), the phonon-band dispersion reveals that the monolayer ZnSe is dynamically stable. In addition, the maximum frequency which corresponds the optical phonon mode appears at 262 cm^{-1} . The low frequencies of the vibrational modes indicates the flexibility of the monolayer ZnSe. The total and the Γ projected phonon density of states are shown in Fig 6.1 (b) so that a possible Raman measurement of a monolayer ZnSe can be compared.

In addition, the energy band gap of monolayer ZnSe is calculated to be 1.91 eV within GGA+SOC. As shown in Fig. 6.2 (a), the valence band maximum (VBM) and conduction band minimum (CBM) appears at the Γ point. For comparison, using the same methodology, the band gap of bulk zb -ZnSe is also calculated to be 1.32 eV which is ~ 0.6 eV lower than that of monolayer. Note that the bulk zb -ZnSe is known to have direct the band gap of ~ 2.8 eV(Yoffe, 1993) and the band gap of the monolayer is reported to be 3.5 eV(Sun *et al.*, 2012). Although the calculated band gap values are underestimated, the difference between the bulk and monolayer is consistent with the experimental difference of ~ 0.7 eV.

We also calculated the electronic density of state which is shown in Figs. 6.2 (b). The VBM is dominated by the Se atoms. In the CBM, it is seen that the Zn and Se atoms contribute. Since the outermost atoms have different bond coordinations, more detailed analysis is needed. Therefore, we focus on the band edges by calculating the band decomposed charge densities of the VBM and CBM. As shown in the right panel of Fig. 6.2, the VBM (I) is dominated by the p_x orbitals of Se atoms, on the other hand, the CBM (II) is dominated by the p_y orbitals Se atoms. For both band edges, the charge densities of the inner atoms are more localized. The outer Se and Zn charge densities

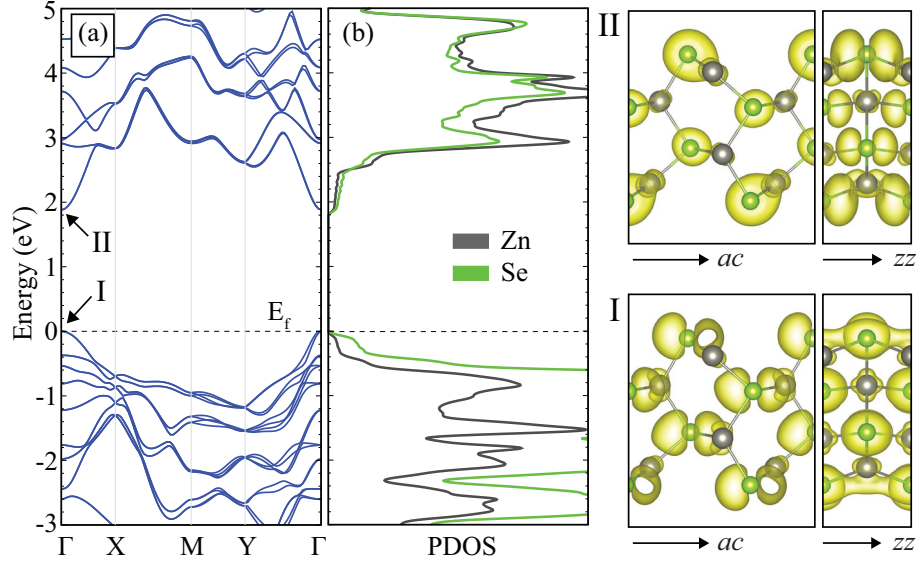


Figure 6.2. The energy-band dispersion is shown in (a). The VBM and CBM are labeled as I and II, respectively. In panel (b), the density of states with Zn and Se contributions are shown as the grey and green curves, respectively. The band decomposed charge densities of the VBM and CBM are shown in right panel. The arm-chair and zig-zag direction are represented by ac and zz , respectively.

extend over the surface of the monolayer especially along the zig-zag (y) direction.

6.2. Mechanical Properties

The dimensional reduction from bulk to monolayer brings not only novel electronic properties but also some unusual mechanical properties. The flexibility of the monolayer ZnSe is emphasized by Sun et al. (Sun *et al.*, 2012) however it is still needed to be elucidated in terms of elastic parameters. Therefore, in this section, we investigate the mechanical properties of the monolayer ZnSe. To obtain the response of the monolayer to the in-plane strain, the total energy differences are calculated under the combinations of strain values along the arm-chair and zig-zag directions as shown in Fig. 6.3 (a). We restrict our calculation in elastic region in which the strains are considered to be between $\mp 2\%$ in each direction. As it is seen, the maximum energy increase is obtained under biaxial strain. Moreover, the change in the energy is larger when the structure strained along the arm-chair (x) direction as compared to that of the zig-zag (y) direction. Since

there is remarkable difference between the strain directions, which is a direct indication of the structural anisotropy, the energy difference is also calculated for the applied strain along the specific direction having an angle θ to the arm-chair (x) direction, so that the angle dependent elastic parameters can be depicted.

In Figs. 6.3 (b) and (c), the tensile and compressive strain-dependent energy curves are shown separately. As it is seen, the response to the strains are not circular but varying with the angle. The maximum energy differences of 92 and 91 meV are obtained when the system strained along the direction of 30° and 90° (zig-zag) angle with respect to the arm-chair direction, respectively. The minimum energy difference (a few meV), on the other hand, is obtained at the angle of 0° and 60° . The response in the level of meV indicates the flexibility of the monolayer ZnSe. Using the strain-energy relation, we further investigate the in-plane stiffness and the Poisson ratio with considering the angle dependency.

The relation between strain and the total energy difference is considered to be obey the formula of $E_s = c_1\varepsilon_\theta^2 + c_2\varepsilon_\phi^2 + c_3\varepsilon_\theta\varepsilon_\phi$, where the ε_θ and ε_ϕ applied strain values along the corresponding direction and the direction which is perpendicular to θ ($\phi - \theta = 90^\circ$), respectively. The coefficients of c_1 , c_2 , and c_3 are obtained separately by fitting the energy-strain equation given above. Since the monolayer ZnSe possesses anisotropic response depending on the strain direction, the c_1 and c_2 are not equal. By using the coefficients of c_1 , c_2 , and c_3 the elastic parameters such as in-plane stiffness and Poisson ratio can be obtained.

In-plane Stiffness: The stiffness defines the resistivity of a material to the structural deformation under mechanical force. It is one of the fundamental properties that describes the flexibility or rigidity of a material. To reveal the mechanical properties, we investigate the in-plane stiffness by using the relation of $C_\theta = [4c_1c_2 - (c_3^2/2c_2)]/A_0$, where the c_1 , c_2 , and c_3 are the coefficients that are determined by the energy-strain relation given above, and A_0 is the area of the unstrained supercell.

The calculated in-plane stiffness, C_θ , is shown as a polar plot in Fig. 6.3 (d). As a consequence of the angle dependent strain energy, the in-plane stiffness values also vary between 1.0-8.0 N/m depending on the strain direction. The in-plane stiffness values for the arm-chair and zig-zag directions are found to be $C_0 = 6.89$ and $C_{90} = 2.07$ N/m, respectively. In addition, the maximum and minimum values are obtained for the angles of 30° and 75° , respectively.

Here, the calculated stiffness can be compared with the Young's modulus of the bulk *zb*-ZnSe yet differing from the bulk form, the thickness of the monolayer ZnSe is

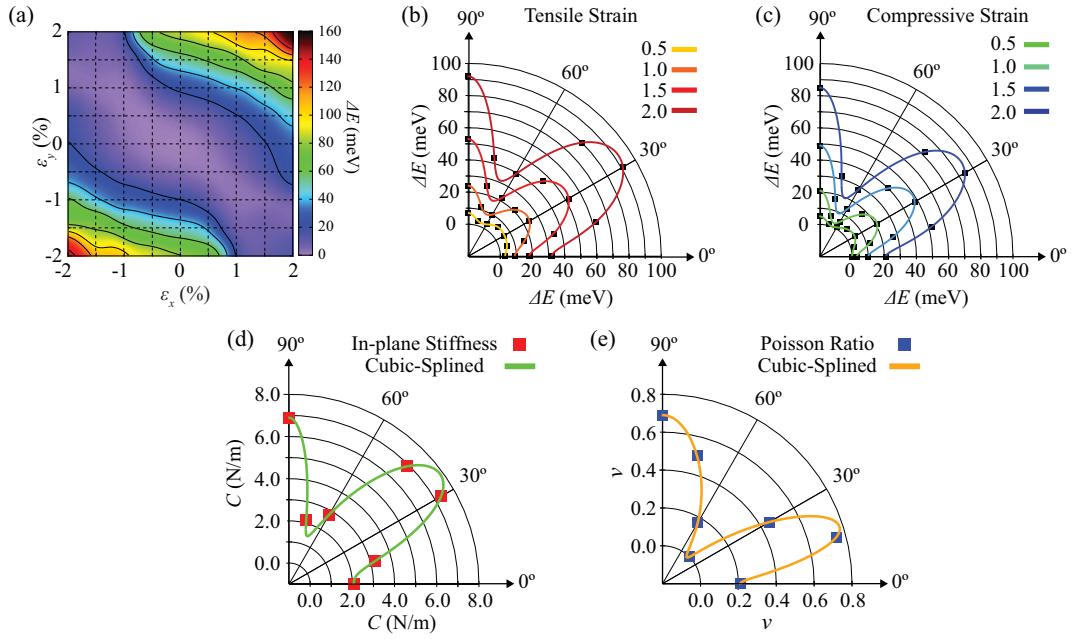


Figure 6.3. (a) The surface plot of the total energy difference of the system under the strain in the arm-chair and zig-zag. The energy levels are color coded. The polar plots of the total energy difference of the system under the tensile (b) and compressive (c) strains, respectively. In panels (d) and (e), the polar plots of the angle dependent in-plane stiffness and the Poisson ratio are shown, respectively.

considered when the in-plane stiffness is obtained. Therefore, we divide the calculated in-plane stiffness by the thickness of the monolayer ZnSe and these effective values in the arm-chair and zig-zag directions are found to be 3.2×10^9 and 10.5×10^9 N/m². The Young's modulus of the bulk *zb*-ZnSe is known to be 67.2×10^9 N/m². As it is seen, there is a dramatic decrease in the stiffness when the dimensionality of structure reduces from 3D to 2D. The small in-plane stiffness values confirmed the flexibility of the monolayer ZnSe which is reported by Sun *et al.* (Sun *et al.*, 2012). In addition, as compared to calculated values of 91 and 77 N/m for GaS and GaSe (Yagmurcukardes *et al.*, 2016), respectively, the in-plane stiffness of the monolayer ZnSe is also very low.

Poisson Ratio: One of the important fundamental elastic constants of a material is the Poisson ratio. Briefly, when a material is stretched (compressed) along one particular direction, it usually shrinks (expands) in the perpendicular direction. The amount of that kind of deformations are governed by the Poisson ratio which must be investigated for

well-identification of the mechanical properties. Therefore, we calculated the angle dependent Poisson ratio of the monolayer ZnSe by using the relation of $\nu_\theta = c_3/2c_1$, where the c_1 and c_3 are the coefficients introduced above.

The polar plot of the calculated Poisson ratio, ν_θ is shown in Fig. 6.3 (e). Apparently, the angle dependency of the Poisson ratio differs from that of in-plane stiffness. The values vary between 0.0-0.75. The maximum Poisson ratio is obtained when the directional angle with of the strain is 15° . For the arm-chair and zig-zag directions, the Poisson ratio are $\nu_0 = 0.21$ and $\nu_{90} = 0.69$, respectively. More significantly, the Poisson ratio for the angle of 45° is about 0.0. When we compare the calculated Poisson ratio of the monolayer ZnSe with that of bulk *zb*-ZnSe, which is known to be 0.28, values are not compatible. Since the monolayer ZnSe is very flexible, the Poisson ratio values given above must be considered qualitatively. Therefore, one can conclude that the in-plane anisotropy is still valid for the Poisson ratio of the monolayer ZnSe.

6.3. Conclusions

In this study, we investigate the synthesized monolayer ZnSe by performing state-of-the-art first principles calculations (Bacaksiz *et al.*, 2017)). The structural optimization reveals that outermost Zn and Se atoms relaxed in a distorted form and the inner Zn and Se atoms have tetrahedral bond coordinations. The phonon analysis shows that the monolayer ZnSe is dynamically stable. In addition, the monolayer, ZnSe has a direct electronic band gap at the Γ symmetry point. The electronic density of states analysis shows that VBM and CBM are dominated by the p_x and p_y orbitals of Se atoms, respectively. Furthermore, we investigate the mechanical properties of the monolayer ZnSe in the elastic region. First of all, the energy-strain calculation shows that the monolayer ZnSe has anisotropic response which depends to the direction of the strain. In particular, the in-plane stiffness values are found to be 6.89 and 2.07 N/m for the arm-chair and zig-zag directions, respectively, which are effectively very low as compared to the Young's modulus of the bulk *zb*-ZnSe. The low in-plane stiffness values are also confirmed the experimental observation of the flexibility of monolayer ZnSe. Moreover, the Poisson ratio is calculated to be 0.21 and 0.69 for the arm-chair and zig-zag directions, respectively. With its flexibility nature and in-plane anisotropic mechanical properties, the monolayer ZnSe appears quite suitable for flexible nanoscale device applications.

CHAPTER 7

ULTRA-THIN SnS₂

The atomic scale of thickness of 2D materials led to new physical insights which suggests that possible other 2D materials may exhibit novel properties. In addition, the need for a wide range of materials for device technology makes the discovery of new layered materials essential.

In regard to search for new graphene-like or TMD-like 2D material, Sn dichalcogenides are good candidate because of their vdW-linked lamellar crystal structure and energy bandgap which is in the visible frequency region. As a member of this family, tin disulfide (SnS₂) was previously investigated in the bulk form for various applications (Delawski and Parkinson, 1992; Fotouhi *et al.*, 1985; Ma *et al.*, 2008; Panda *et al.*, 2007; Parkinson, 1990, 1988; Schlaf *et al.*, 1995). After the emergence of novel 2D materials and improved production methods such as chemical vapor deposition, chemical and mechanical exfoliation, thinner structures of SnS₂ were synthesized for different applications. For example, a few nanometer-thick hexagonal SnS₂ was used for lithium storage in battery applications (Kim *et al.*, 2007; Ma *et al.*, 2012; Seo *et al.*, 2008; Zhai *et al.*, 2011). To enhance the electrochemical performance, composite forms of SnS₂ with graphene were examined (Huang *et al.*, 2015; Jiang *et al.*, 2012; Qu *et al.*, 2014; Zhou *et al.*, 2014; Zhuo *et al.*, 2012). Single- and few-layer SnS₂ were also used to fabricate a field-effect transistor (De *et al.*, 2013; Pan *et al.*, 2013; Song *et al.*, 2013). Moreover, photocatalytic character of single- and few-layer SnS₂ was shown in different studies which is directly related to the optical properties of hexagonal SnS₂ (Chao *et al.*, 2012; Chen *et al.*, 2013; Sun *et al.*, 2012; Wei *et al.*, 2014). Furthermore, SnS₂ nanosheet was studied for photosensitive field emission and photodetector applications (Joshi *et al.*, 2015; Xia *et al.*, 2015).

Recently, Zhang *et al.* demonstrated that photoluminescence spectrum of SnS₂ and MoS₂ show additional features when they form a van der Waals heterostructure which is important for the engineering of their electronic and optical properties (Zhang *et al.*, 2013). Huang *et al.* investigated the synthesis, characterization and the electronic properties of SnS₂, from bulk to monolayer (Huang *et al.*, 2014). More recently, Su *et al.* reported that hexagonal SnS₂ is a suitable material for photodetection applications with fast photocurrent response time $\sim 5 \mu\text{s}$ (Su *et al.*, 2015). In addition to these, Ahn *et al.*

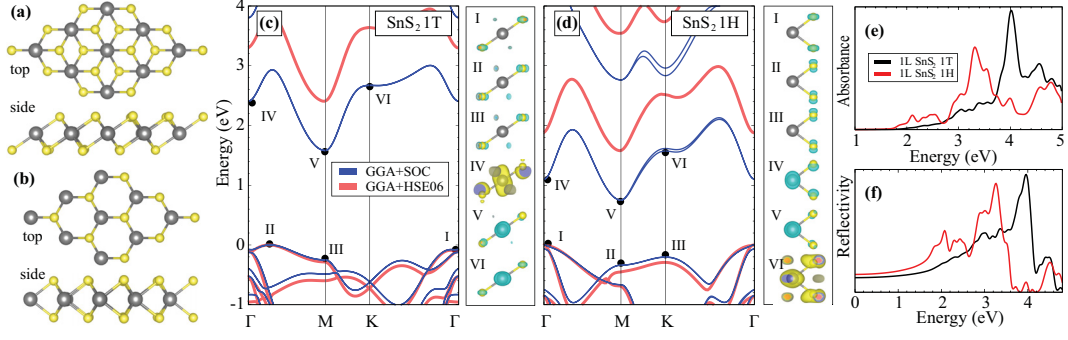


Figure 7.1. (a) and (b) illustrate the structure of monolayer 1T and 1H SnS_2 , respectively. (c) and (d) are the band structures of 1T and 1H SnS_2 . The blue curves and the curve with red-circles are for GGA+SOC and GGA+HSE06, respectively. (e) and (f) are absorbance and the reflectivity of the 1T (black curve) and 1H SnS_2 (red curve).

successfully synthesized hexagonal SnS_2 and orthorhombic SnS as a polymorphic 2D heterostructure (Ahn *et al.*, 2015).

Although there are a few number of computational works on single-layer hexagonal SnS_2 (Xia *et al.*, 2014; Zhuang and Hennig, 2013), comprehensive investigation of electronic and optical properties of its monolayer and bilayer crystal structures are still lacking. Therefore, in this study (Bacaksiz *et al.*, 2016), we concentrate on the monolayer and bilayer forms of hexagonal SnS_2 . The structural parameters, electronic properties and optical response of these materials are investigated using ab initio methods. In addition, from the calculated absorbance or reflectivity spectra, the optical signatures which allows one to characterize the structural phase or the stacking order of the SnS_2 layers were sought. Furthermore, we investigate the effects of an applied perpendicular electric field, charging, and loading pressure on the characteristic properties of bilayer SnS_2 .

7.1. Computational Details

In addition to structural and electronic properties which were calculated by using the methodology given in Sec. 2.4, we also calculated the the dielectric function which provides us with the optical quantities such as the frequency dependent absorbance $A(\omega)$

Table 7.1. Calculated parameters for monolayer SnS₂ are the lattice constant in the lateral direction, a ; the distance between the subplanes of S, c ; the intralayer atomic distance, d_{Sn-S} ; the charge transfer from Sn to S atom, $\Delta\rho$; the work function Φ ; and the cohesive energy, E_c . E_g^{GGA} and E_g^{HSE06} are the energy band gap values within GGA+SOC and GGA+HSE06, respectively.

	a (Å)	c (Å)	d_{Sn-S} (Å)	$\Delta\rho$ (e^-)	Φ (eV)	E_c (eV)	E_g^{GGA} (eV)	E_g^{HSE06} (eV)
1T SnS ₂	3.68	2.96	2.59	0.7	7.53	3.79	1.58	2.40
1H SnS ₂	3.60	3.23	2.63	0.7	6.19	3.49	0.78	1.58

and the Fresnel reflectivity $R(\omega)$ through the formulas;

$$A(\omega) = \frac{\omega}{c} L \text{Im}[\epsilon(\omega)] \quad (7.1)$$

$$R(\omega) = \left| \frac{\sqrt{\epsilon(\omega)} + 1}{\sqrt{\epsilon(\omega)} - 1} \right|^2 \quad (7.2)$$

where the dielectric function is defined as $\epsilon(\omega) = \epsilon_1(\omega) + i\epsilon_2(\omega)$ and ω is the frequency, c is the speed of light, L is the unitcell length in the perpendicular direction.

7.2. H and T Phases of Single Layer SnS₂

Monolayer SnS₂ possesses two different phases 1T and 1H as shown in Fig. 7.1. Both phases have three trigonal subplanes where the Sn subplane is sandwiched by two S-subplanes. The 1T phase is a member of the $P\bar{3}m2$ space group where subplanes of it are ABC stacked. The 1H is a member of the $P\bar{6}m2$ space group where subplanes of it are ABA stacked. The lattice vectors of both phases are $\mathbf{v}_1 = a(\frac{1}{2}, \frac{\sqrt{3}}{2}, 0)$, $\mathbf{v}_2 = a(\frac{1}{2}, -\frac{\sqrt{3}}{2}, 0)$ where $|\mathbf{v}_1| = |\mathbf{v}_2|$ and a is the lattice constant. The atomic coordinates of 1T phase are $(\frac{|v_1|}{2}, \frac{|v_1|}{2}, 0)$, $(\frac{|v_1|}{6}, \frac{|v_1|}{6}, \frac{c}{2})$, and $(\frac{5|v_1|}{6}, \frac{5|v_1|}{6}, -\frac{c}{2})$ for the Sn atom and the S atoms, respectively, where c is the distance between the subplanes of S atoms. The atomic coordinates of 1H phase are given as $(\frac{|v_1|}{3}, \frac{|v_1|}{3}, 0)$, $(\frac{2|v_1|}{3}, \frac{2|v_1|}{3}, \frac{c}{2})$, and $(\frac{2|v_1|}{3}, \frac{2|v_1|}{3}, -\frac{c}{2})$.

We obtained the lattice constants of 3.68 Å and 3.60 Å for 1T and 1H, respectively. The corresponding Sn-S bond lengths (d_{Sn-S}) are 2.59 Å and 2.63 Å which are given in

Table 7.1. The energy difference between the 1T and 1H phases is 875 meV per unit cell which shows that the formation of the 1H phase is less favorable than 1T. The cohesive energies of 1T and 1H phases are 3.79 eV and 3.49 eV, respectively. These results are consistent with the previous results which find the 1T phase the most favorable form of the monolayer. For both phases, $0.7 e^-$ is donated to each S atom by Sn atom. This charge transfer is larger as compared to MoS_2 in which Mo donates $0.5 e^-$ to each S. In addition, the work functions (Φ) of the phases are 7.54 eV and 6.19 eV. These work function values are larger than those of graphene and bilayer graphene (~ 4.6 and ~ 4.7 eV (Yu *et al.*, 2009), respectively) and of single- and few-layer MoS_2 (~ 5.4 eV (Choi *et al.*, 2014)).

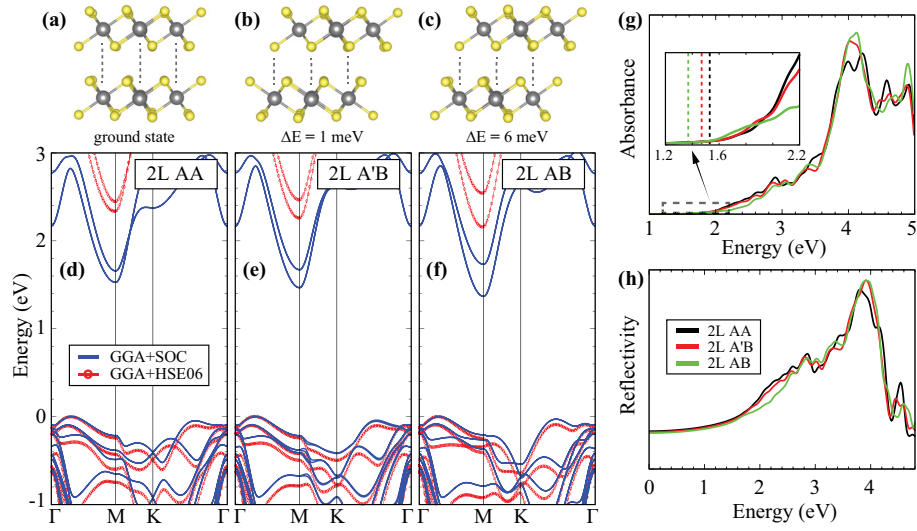


Figure 7.2. (a), (b), and (c) are side views of bilayer SnS_2 , and (d), (e), and (f) are band structures within the GGA+SOC (blue) and GGA+HSE06 (red-circle) for AA , $A'B$, and AB stackings, respectively. (g) and (h) are the calculated absorbance and reflectivity of the AA (black), $A'B$ (red), and AB (green). The vertical lines in the inset of (g) represent the band gap values of the corresponding stacking orders.

Band structures of 1T and 1H phases based on GGA including spin-orbit coupling (SOC) and HSE06 hybrid functional are given in Fig. 7.1. The 1T phase of SnS_2 monolayer has an indirect band gap where the VBM is between the Γ and M points and the conduction band minimum (CBM) is at the M point. As given in Table 7.1, the band gap of 1T phase is 1.58 eV within GGA+SOC and 2.40 eV within GGA+HSE06. The 1H phase also has an indirect band gap where the VBM is at Γ point and the CBM is at M point. The band gap values are 0.78 eV within GGA+SOC and 1.58 eV within GGA+HSE06.

In Fig. 7.1, band decomposed charge densities of the valance and conduction band edges are also given. For both phases, the charge density of the VBM is dominated mainly by the p_x and p_y orbitals of S atom. On the other hand, the CBM is dominated by s of Sn and p_z of S orbitals. These orbitals of the band edges are different than that of MoS₂ in which the VBM and CBM are composed of d_{xy} and d_{z^2} , respectively (Padilha *et al.*, 2014).

The effect of the SOC is evident in both the 1T and 1H structures, as shown in Figs. 7.1 (c) and (d). In the 1T structure, the splitting is ~ 50 meV at the highest VB states at the Γ point while in the 1H structure the splittings are ~ 69 meV in the highest VB states at the Γ point and ~ 43 meV in the lowest CB states at the K point. These splittings can be exploited in ‘valleytronics’ applications where the excitations of the electrons with different spin are controlled by the polarization of the incident light. This was recently demonstrated for the TMDs, especially for MoS₂ (Cao *et al.*, 2012; Mak *et al.*, 2012).

The absorbances and the reflectivities of monolayer SnS₂ are also calculated and the energy dependent plots are given in Figs. 7.1 (e) and (f), respectively. The absorbance plot shows that the 1T and 1H phases have different characters. For the 1T phase, absorbance (black) starts at ~ 1.8 eV, and at around 4 eV a peak is found. It has also a local maximum at around 4.5 eV. On the other hand, for the 1H phase the absorbance (red) starts at ~ 1.7 eV and it shows its main peak around 3.2 eV, a local maximum around 4.8 eV. Since the absorbance spectra of the alternative phases are quite distinguishable, optical absorbance measurements can be a reliable tool for determining the structural phase of monolayer SnS₂ samples.

7.3. Bilayer SnS₂

Determining or controlling the stacking order of a layered material is important for electronic and optical applications. They can modify the electronic and the optical properties even if the layers are weakly interacting as in van der Waals layered materials. Improvements in synthesis techniques allows researchers to control the stacking order of multilayer structures and synthesis of devices with desired features. Therefore, in this section we investigate properties of bilayer SnS₂ starting with the analysis of possible stacking orders.

In Fig. 7.2, bilayer structures with three different stacking types, their corresponding band diagrams, and the imaginary part of the dielectric functions are given. In the monolayer section, the 1T phase was found to be energetically favorable, and therefore we restrict ourselves to 1T phase. *AA* (Sn atoms are aligned on Sn atoms), *AB* (S atoms

Table 7.2. Calculated values for possible stacking types of bilayer 1T-SnS₂ of the lattice constant in the lateral direction, a ; the distance between the S sublayers of the layers, d_{L-L} ; the energy difference between the structures per SnS₂, ΔE ; interlayer interaction potential per formula, E_{L-L} ; the work function, Φ ; and the cohesive energy, E_c . E_g^{GGA} and E_g^{HSE06} are the energy band gap values within GGA+SOC and GGA+HSE06, respectively.

	a (Å)	d_{L-L} (Å)	ΔE (meV)	E_{L-L} (meV)	Φ (eV)	E_c (eV)	E_g^{GGA} (eV)	E_g^{HSE06} (eV)
AA	3.68	2.95	0	38	6.50	3.81	1.53	2.34
$A'B$	3.68	2.97	1	38	6.50	3.81	1.47	2.27
AB	3.68	3.03	6	35	6.58	3.81	1.37	2.17

are aligned on Sn atoms) and $A'B$ (similar with AB but the bottom layer is upside-down) are considered. Also the AA' stacking (not shown) where the S atoms are aligned on S is examined, but its total energy is considerably larger as compared to the given three other stacking types. A few meV energy difference was found between the AA , $A'B$, and AB stacking orders which are given in Table 7.2 where we have set the minimum energy to 0. All types have the same lattice constant of 3.68 Å. The interlayer distances are 2.95 Å, 2.97 Å, and 3.03 Å for the AA , $A'B$, and AB stacking orders, respectively.

The cohesive energy of bilayer SnS₂ in all stacking orders are the same, 3.81 eV which is slightly higher than the monolayer 1T phase. The work functions are also similar where the values are 6.50 eV, 6.50 eV and 6.58 eV for the AA , $A'B$, and AB , respectively. The work function of the bilayer is smaller than that of the 1T monolayer which is in contrast with what was found for graphene and MoS₂(Choi *et al.*, 2014; Yu *et al.*, 2009). Another point is that the interlayer potential energy per SnS₂ for the different stacking types are also very close to each other; 38 meV, 38 meV, and 35 meV for AA , $A'B$, and AB , respectively. This weak interaction is a characteristic feature of van Waals layered materials, yet these energy values are smaller as compared to graphite (30-55 meV per atom)(Chen *et al.*, 2013; Liu *et al.*, 2012) and typical TMDs (74, 107, 90, 126 meV per MX₂ for MoS₂, MoSe₂, WS₂, WSe₂, respectively(He *et al.*, 2014)).

In spite of the weak interlayer interactions, and the similarities of the structural parameters, the AA , AB and $A'B$ stacking types possess different band dispersions and band gaps. Although the VBM and the CBM are at the same symmetry points for all stacking orders, the values of the indirect band gaps are different. For AA , which is en-

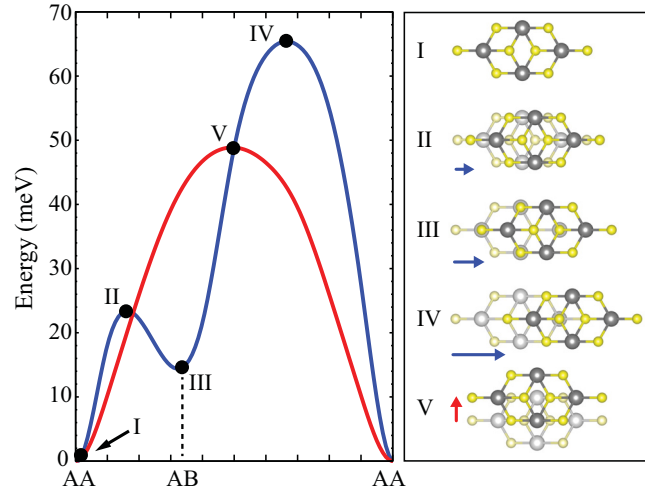


Figure 7.3. Left panel, blue (red) curve indicates the energy difference when the top layer is sliding along the armchair (zig-zag) direction. Right panel, the structural forms of the extremas marked on the energy profiles are given.

energetically the favorable one, we have 1.53 eV band gap within GGA and 2.34 eV within HSE06. The band gaps in the $A'B$ and the AB stackings are 1.47 and 1.37 eV within GGA and 2.27 and 2.17 eV within HSE06, respectively. It must be emphasized that the band dispersions arising from each bilayer configuration differ especially at the symmetry points M and K which are important for the optical transitions and the excitonic states. For AA stacking, the two CB edge states at the M point are very close to each other as compared to those of $A'B$ and AB . On the other hand, the two CB edge states at the K point are significantly different in energy as compared to those of $A'B$ and AB . The absorbance spectrum of the bilayer systems are given in Figs. 7.2 (g) and (h). The general trend of the absorbances for all bilayers are similar. Inset of Fig. 7.2 (g) is a zoom at the onset region of the absorbance spectrum. Despite the weak interactions given in Table 7.2, the absorbance spectra provide information on the stacking. In addition, the main peak around 4 eV of the AA stacking displays two distinct peaks while $A'B$ and AB have only one peak. Hence, the simple absorbance spectrum carries structural signatures although the structures are energetically very similar.

The weak layer-layer interaction in bilayer SnS_2 is also promising for barrierless sliding applications. The sliding potential in the armchair and the zig-zag directions are given in Fig. 7.3. The local and global extrema and the corresponding structural forms are shown. The positions of the upper S atoms of the bottom layer and lower S atoms

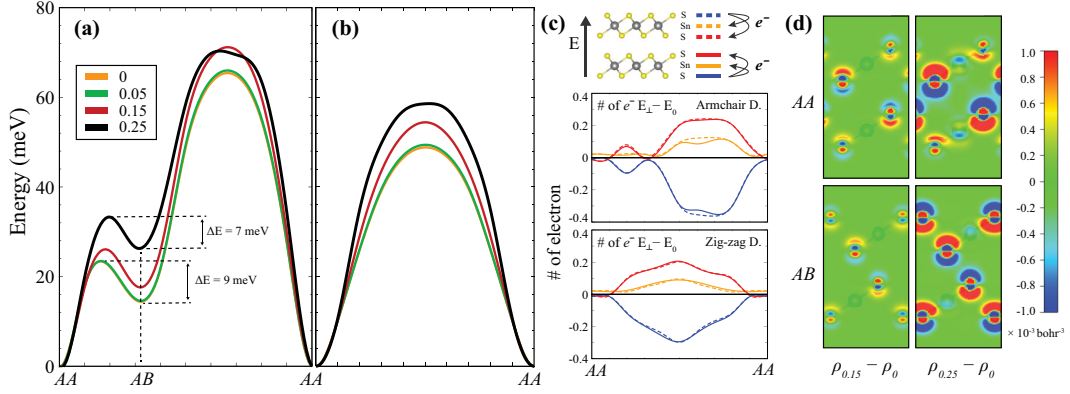


Figure 7.4. The plot of the energy barrier in the armchair (a) and zig-zag (b) directions under increasing electric fields. The blue, black, green and red lines are for 0.05, 0.15, 0.25 V/Å electric field values, respectively. (c) electron transfer from outer S atoms to the inner part (upper) and the total number of electron difference (lower) between 0.25 V/Å and zero electric field on the sliding paths. (d) The cross section of the total charge density difference between zero and non-zero field cases for both AA and AB stacking orders.

of the top layer are responsible for the potential profile. In the case of sliding along the armchair direction the local maximum is seen when the lower S atoms of the top layer are positioned at the mid point of the upper S atoms of the bottom layer. This is followed by a local minimum that corresponds to AB stacking. The highest point of the barrier is ~ 65 meV. This point is also global maximum where the S atoms from top and bottom layer are aligned on top of each other. This energy barrier is very small as compared to that of MoS₂ (~ 200 meV)(Tongay *et al.*, 2014). In the zig-zag direction, the barrier profile results in a symmetric peak with the highest point obtained when the S atoms of the top and bottom layers are closest to each other at the path of sliding. The maximum value of the barrier is ~ 50 meV. This type of barrier is common for the T phase of TMDs. Following subsections investigate how these barrier profiles are modified by electric field, charging and loading pressure.

Effect of External Electric Field: In this part, we investigate how the sliding potential is modified under the influence of an external perpendicular electric field (E-field). Three different (0.05, 0.15, 0.25 V/Å) E-field values in the positive z -direction (perpendicular to the plane of bilayer system) are applied. While the energy barrier is conserved, the barrier heights increases as shown in Figs. 7.4 (a) and (b). The changes at 0.05 V/Å field is

negligible and the profiles are almost the same as in the zero E-field case. In addition, for *AB* stacking the energy difference between the local minimum and the neighboring local maximum decreases with applied E-field. The reason of the changes can be elucidated by analyzing the variations of the charge separation in the system.

In Fig. 7.4 (c), by using the Bader charge analysis technique, the amount of charge difference on the atoms between the 0.25 V/Å case and the zero field case is shown along the sliding path. The solid (dashed) orange curve represents the Sn atoms at the bottom (top) layer. The solid (dashed) blue curve represents the outer S atom at the bottom (top) layer and the solid (dashed) red curve is for the inner S atom (S atoms between the sublayers of Sn atoms). The charge configurations seem to be sensitive not only to the E-field but also the stacking order of the layers. Firstly, the charge variations of the Sn atoms of the bottom and the top layers are positive which indicates that the E-field shifts electron around the Sn atoms. On the other hand, the behaviors of the changes on the S atoms are different according being at the outer or the inner part of the bilayer system. The outer S atoms have less electrons under E-field while inner S atoms attain more electrons. As an exception to these trends, the charge of the S atoms is not altered much by the E-field for the *AA* and the *AB* stackings. It needs more detailed analysis.

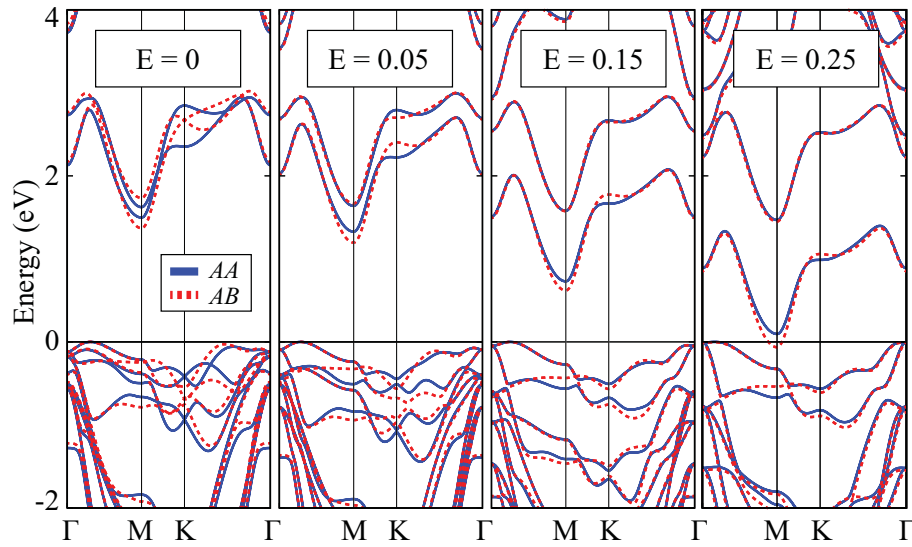


Figure 7.5. Energy band dispersions under three different E-field which are 0.05, 0.15, and 0.25 V/Å perpendicular to the plane of structure. The blue curves are for *AA* stacking and red curves are for *AB* stacking.

To clarify the effect of the external E-field on the *AA* and *AB* bilayer systems,

the total charge density difference between with- and without-E-field for the cross section through the atoms in the unitcell are shown in Fig. 7.4(d). It seems that the S atoms are polarized by the E-field, but the Sn atoms experience no significant change. In the case of 0.15 V/\AA , the polarizations are larger at the inner sides of S atoms for both *AA* and *AB* stackings. In the case of 0.25 V/\AA , the polarization vanishes at the outer S atoms for *AA* stacking order. On the other hand, the polarization still exists and is enhanced at the inner S atoms of *AA* and all S atoms of *AB* stacking. More importantly, the number of electron increases gradually between the layers with electric field strength for both the *AA* and the *AB* stackings. This charge accumulation between the layers is consistent with the study of Ramasubramaniam *et al.* (Ramasubramaniam, 2012) where the MoS_2 bilayer is tuned by the external E-field and the charge distribution between the layers was gradually enhanced with increasing out of plane E-field. According to our results, the perpendicular E-field increases the coupling between the SnS_2 layers for *AA* stacking as compared to *AB*.

In addition, the E-field dramatically modifies the electronic structure of the bilayer system as shown in Fig. 7.5. Under the E-field, the VBM approaches to Γ point while the CBM at *M* point drops in energy which means that band gap decreases. The drop of band gap with E-field is slower for the *AA* stacking, so under 0.25 V/\AA E-field, the *AB* become semi-metal while the *AA* stacked bilayer is semiconductor with band gap 85 meV within GGA. Although this is the underestimated band gap, the trend of change on electronic structure together with enhanced stacking strength at *AA* order indicates that perpendicular E-field is useful method for tuning the band gap of bilayer SnS_2 which is needed in a material for the field effect transistor application.

Effect of Charging: The sliding-energy barrier can also be tuned by controlling the total charge on the system. In this part, we examine the modifications of the sliding barrier by adding or subtracting electron (doping electron or hole) to the bilayer. In Figs. 7.6 (a) and (b), we show respectively the barriers forms along the armchair and the zig-zag directions for four different charging conditions. Positive value of charging refers to extra electrons. First of all, it is interesting that the $0.2 e^-$ and also the $0.1 e^-$ (per unit cell) cases result in a minimum energy for the *AB* stacking instead of *AA*. In addition, the barrier height decreases in all charging conditions and the shape of the barrier differs considerably for the armchair direction. Moreover, the maximum barrier height in the zig-zag direction decreases down to $\sim 20 \text{ meV}$ which is comparable with the thermal energy at room temperature (25 meV).

The effect of charging can be understood by monitoring the charge localizations

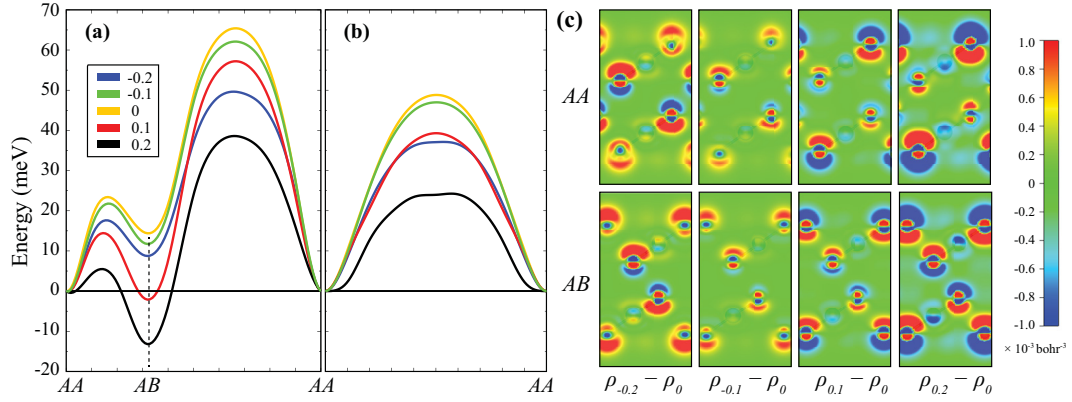


Figure 7.6. Plot of the energy barrier for sliding in the armchair (a) and the zig-zag (b) direction for four different charging cases and the bare case. Positive value of charging refers to a higher electron density. The blue curves represents the bare case. The green, the black, the yellow and the red curves are for the charging case of -0.2 , -0.1 , 0.1 , $0.2 e^-$. (c) Cross section of the total charge density difference between the charged cases and the bare case.

for *AA* and *AB* stacking. Therefore, in Fig. 7.6(c), the cross section of the charge density differences between the charged and the bare systems is shown for *AA* and *AB* stackings. It is expected that only positively charged regions to appear in the plot for the electron subtracted system. For the electron-added system, the expectation is the opposite. However the occurrence of both positive and negative regions for each charging case indicates that charging (positive or negative) modifies the distribution of the other electrons. In Fig. 7.6(c), it is explicitly seen that the inserted charges accumulate to the outer surfaces (red for positive charges and blue for the negative charges) of the bilayer system. In all cases, except the $0.2 e^-$ added to *AA* stacking, the electrons (blue region) also accumulate to the region between the layers. When we compare the *AA* and *AB* stackings in all charging conditions, the lower energy case has always a larger amount of electrons (negative charge means blue region) between the layers which indicates that the interactions between the layers have covalent character.

In addition, when electrons are doped, *s* orbital of Sn atoms which mostly construct the CBM are firstly occupied as shown in Fig. 7.7. The energy difference between the newly occupied Sn states and the already occupied S states decreases. The change is higher for the *AB* stacking as compared to *AA*. For the hole doping case, *p_x* and *p_y* orbitals of S atoms which are dominant around the Fermi level (VBM) are firstly occupied. To sum up, both electron and hole doping decreases sliding barrier which makes easier

to modify the stacking order, and for proper value of electron doping, favorable stacking order become AB stacking instead of AA .

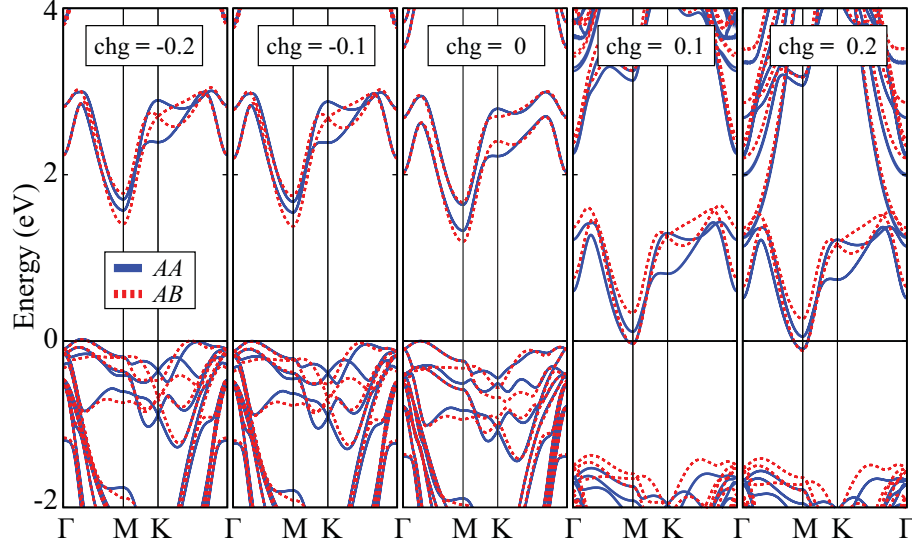


Figure 7.7. Energy band dispersions for four different charging conditions which are -0.2 , -0.1 , 0.1 , and $0.2 e^-$. The negative numbers refer the electron subtracted (hole doping) cases and the positive numbers refer the electron added (electron doping) cases. The blue curves are for AA stacking and red curves are for AB stacking.

Bilayer Under Loading Pressure: The energy landscape of bilayers under constant loading pressure is studied for various 2D materials (Cahangirov *et al.*, 2009). It is shown that for a given value of the applied pressure, the ratio between intralayer and interlayer interaction is a material property that describes the transition from the stick-slip to the superlubric regime. Here we study the effect of a constant loading pressure on the energy landscape of bilayer SnS_2 .

The AA and the AB stackings of bilayers, composed of materials like MoS_2 , have the same energy due to the symmetry of the 1H structure. However, the energy of bilayer SnS_2 in 1T is different for AA and AB stackings. This is evident from the previous figures in this section as well as from Fig. 7.8(a) where we present the constant height energy landscape of the SnS_2 bilayer. To calculate the energy landscape at constant pressure we repeat constant height scans by lowering the height by 0.2 \AA steps. In this way we get the energy for the three-dimensional movement of the layers with respect to each other. We use this data to create the plots presented in Fig. 7.8(b). Here for a chosen

loading pressure we first find the corresponding force in the z -direction. Then using spline interpolation we calculate the height that gives this force for each position in the xy plane while moving from AA stacking to AB stacking. Interestingly, as the applied pressure is increased the relative energy difference between AA and AB stacking decreases and become even zero at 3 GPa. For pressures exceeding 3 GPa AB stacking becomes more favorable than AA stacking.

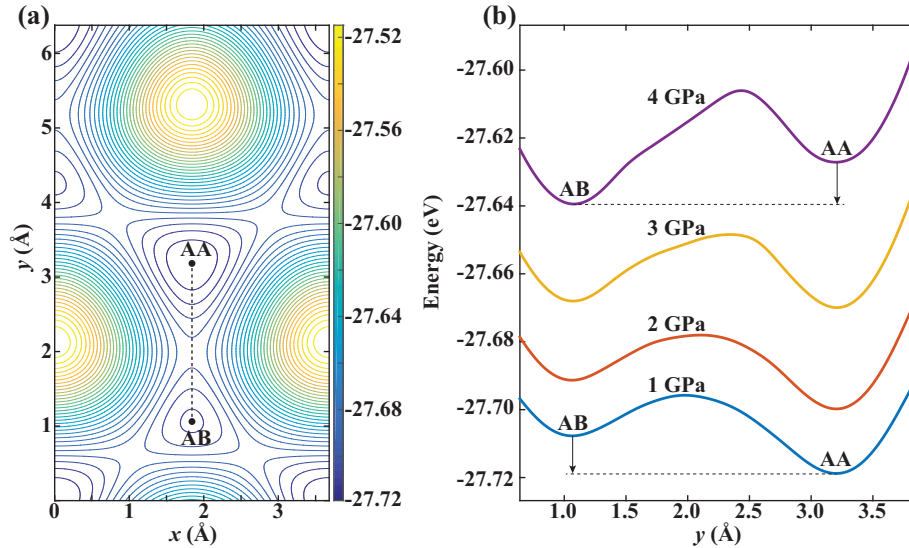


Figure 7.8. (a) Constant height energy landscape of bilayer SnS_2 . The height is fixed at the value corresponding to the distance between the top and the bottom sulfur atoms when the bilayer is fully relaxed. (b) The constant pressure energy dependence along the line connecting the AA and the AB stackings.

7.4. Conclusions

Starting from the monolayer, the electronic and the optical properties of bilayer SnS_2 are investigated within first principles DFT calculations (Bacaksiz *et al.*, 2016). We found that the interaction between the layers is weaker than that of MoS_2 and other common TMDs. We showed that although the layers interact weakly the energy band gaps and the absorbance spectra could be informative about the stacking type of the bilayer system. The energy barrier for the sliding of one layer over the other is found to be ~ 65 meV at its maximum which is also small as compared to MoS_2 .

The effect of applied E-field, charging and loading pressure on the sliding barrier of bilayer SnS₂ were also studied. Under the influence of a perpendicular E-field, for the *AA* stacking which is favorable for the bilayer system, the coupling of the layer strengthens and consequently the sliding barrier height increases. In addition, it is shown that band gap of the bilayer SnS₂ can be tuned by perpendicular E-field and under sufficient E-field it can be turned from semiconductor to semi-metal. On the other hand, both adding and subtracting electrons decreases the barrier. More significantly, under charging or loading pressure, *AB* stacking order can become the favorable configuration instead of *AA* stacking. Tunable bandgap makes 2D crystal of SnS₂ a promising material for nanometer size field effect transistor applications. Furthermore, due to its easy-tunable stacking sequence, layered SnS₂ is also a good candidate for nanoscale lubricant applications.

CHAPTER 8

OPTICAL PROPERTIES OF h -AlN

One of the main reasons of the growing interest on such materials is their optical properties. It was shown that graphene reflects only 0.1% of the incident light in the visible region(Nair *et al.*, 2008), which can be enhanced by increasing the number of layers(Casiraghi *et al.*, 2007). It was also demonstrated that graphene flakes can be made luminescent by mild oxygen plasma treatment(Gokus *et al.*, 2009). In addition, Mak *et al.* reported that distinct optical conductivity spectra were observed for different samples having the same number of layers. The effect of stacking order on the electronic structure of few-layer graphene was also shown(Mak *et al.*, 2010). Lui *et al.* experimentally demonstrated a waveguide-integrated electroabsorption modulator, based on monolayer graphene with broadband and high-speed. Owing to the high modulation efficiency of graphene, the device has $25 \mu m^2$ active area, which was the smallest to its date(Liu *et al.*, 2011).

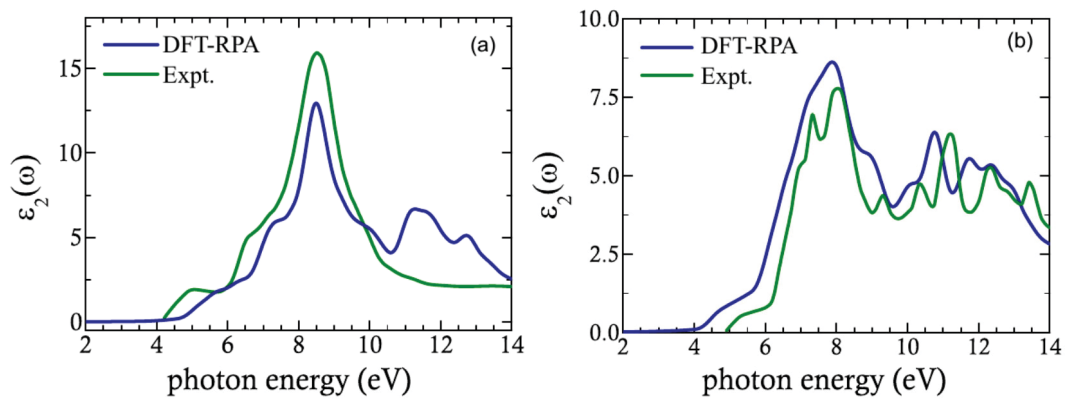


Figure 8.1. Optical absorption spectrum of (a) bulk hexagonal-AlN and (b) bulk wurtzite-AlN compared to experimentally obtained imaginary dielectric function Source: (Li *et al.*, 2003; Loughin *et al.*, 1993).

In addition to graphene, binary compound MoS_2 , a member of TMD family, displays interesting optical properties. Splendiani *et al.* showed that single-layer MoS_2 exhibits strong photoluminescence in contrast to the bulk form(Splendiani *et al.*, 2010). In

addition, Mak *et al.* investigated monolayer and few-layer MoS₂ by optical spectroscopy and reported that compared to its bulk form, monolayer MoS₂ displays an increase in the quantum efficiency of luminescence by more than a factor of 10⁴(Mak *et al.*, 2010; Eda *et al.*, 2011). Yin *et al.* indicated that a phototransistor based on monolayer MoS₂ yields better photoresponsivity than the graphene-based device(Yin *et al.*, 2012). Feng *et al.* studied the optical properties of monolayer MoS₂ with charged vacancies and found that vacancies induce extra peaks at low energy in the complex dielectric function(Feng *et al.*, 2014).

Hexagonal structure of monolayer BN (*h*-BN), despite its structural similarity to graphene, is an insulator. It was addressed that *h*-BN possesses an ultraviolet luminescent peak at 215 nm which is critical for deep-UV light-emitting and laser applications(Watanabe *et al.*, 2004). Furthermore, Kim *et al.* showed that 2D *h*-BN layers display very high transparency (transmittance over 99%) in the wavelength range of 250-900 nm, with a sharp absorption peak below 250 nm, where the optical gap was calculated as 6.07 eV(Kim *et al.*, 2012). Gao *et al.* indicated that the optical gap of *h*-BN increases with decreasing number of layers(Gao *et al.*, 2013). On the other hand, no cathodoluminescence or photoluminescence measurements of monolayer or few-layer *h*-BN structures have yet been reported. This indicates that further studies are needed in order to explore the optical properties of *h*-BN to expand its potential applications(Song *et al.*, 2013).

AlN is a III-V binary compound material with remarkable features which makes it very promising for advanced technological applications. It has high electrical resistivity(Virkar *et al.*, 1989; Weimer *et al.*, 1994) and high thermal conductivity(Slack *et al.*, 1987). As AlN has a wide direct electronic band-gap of ~ 6 eV(Li *et al.*, 2003), it can be potentially used in ultraviolet light-emitting-diodes (LEDs) and laser diodes(Adivarahan *et al.*, 2004; Akasaki and Amano, 1997; Han *et al.*, 1998; Hirayama, 2005; Khan *et al.*, 2008; Nishida and Kobayashi, 1999; Ponce and Bour, 1997). At ambient conditions, the stable bulk form of AlN is wurtzite, however under high pressure, phase transition from wurtzite to zinc blende or rock-salt forms were previously addressed(Hultman *et al.*, 1992; Ueno *et al.*, 1992; Xia *et al.*, 1993). Following the theoretical prediction(Şahin *et al.*, 2009), *h*-AlN was experimentally recently realized by Tsipas *et al.*(Tsipas *et al.*, 2013) Theoretical studies on nanofilms of AlN also indicate that the hexagonal phase (graphitic-like structure) is a lower energy configuration for only small thicknesses(Freeman *et al.*, 2006b). However, the domain of stable hexagonal structures can be extended to larger thicknesses by applying epitaxial strain(Wu *et al.*, 2011).

Electronic properties of monolayer and few-layer forms of *h*-AlN also theoretic-

cally studied(Şahin *et al.*, 2009; Zhuang *et al.*, 2013) and excitonic effects on monolayer *h*-AlN were investigated(Fakhrabad *et al.*, 2015). However, to the best of our knowledge, there are no studies yet on the modification of the optoelectronic properties of monolayer and few-layered *h*-AlN, unlike the numerous experimental and theoretical works on well-known 2D materials such as graphene, *h*-BN and MoS₂. Thus, the aim of the present study(Kecik *et al.*, 2015) is to investigate the layer and strain dependent optical properties of the recently discovered *h*-AlN. An approach based on random phase approximation on top of the density functional theory is adopted in order to depict the trends among the different cases, which is seen sufficient for a qualitative evaluation of the spectral optical quantities, considering also the computational burden that more advanced methodologies would bring. On the other hand, higher levels of accuracy in the calculations, namely the quasiparticle corrections and electron-hole interactions are also accounted for in order to depict their influence on the optical features of specific cases.

8.1. Computational Details

In Sec. 2.4, the general methodology to obtain the structural and electronic properties is given. Regarding the optical response calculations, random phase approximation (RPA)(Bohm and Pines, 1951; Ehrenreich and Cohen, 1959) was undertaken on top of the DFT approach. A Monkhorst-Pack(Monkhorst and Pack, 1976) *k*-point sampling of $127 \times 127 \times 1$ was adopted for PBE-RPA calculations of the 2D unit cell. A total number of 192 bands was used and the vacuum space was increased to 18 Å for the computation of the optical properties. The *k*-point mesh and number of bands were scaled accordingly for the bulk forms of both hexagonal and wurtzite AlN. Local field effects were accounted for both at the levels of Hartree and exchange-correlation potential.

Subsequently, hybrid functionals (HSE06)(Heyd and Scuseria, 2004b,a; Paier *et al.*, 2006) and quasiparticle (QP) *GW* corrections(Shishkin and Kresse, 2006; Hedin, 1965; Hybertsen and Louie, 1986) were undertaken in order to test the validity of the approaches, for specific cases (mono- and bilayer *h*-AlN). Finally, for the optical response beyond the independent-particle approach, the Bethe-Salpeter equation (BSE)(Onida *et al.*, 2002; Rohlfing and Louie, 2000; Salpeter and Bethe, 1951) was employed on top of the G_0W_0 step, where the Tamm-Dancoff approximation (TDA) was adopted. Due to the computational burden, *k*-point sampling was limited to $19 \times 19 \times 1$ for the G_0W_0 approach. The plane-wave cutoff was decreased to 350 eV and basis set for the response functions was set to 240 eV for the many-body calculations. Total number of bands used

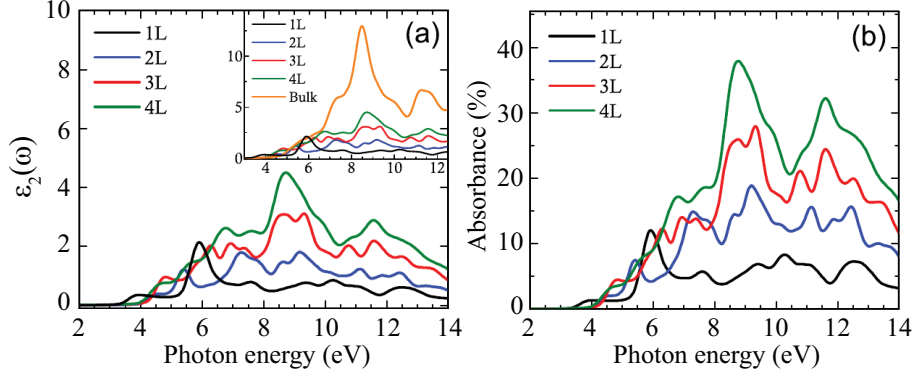


Figure 8.2. (a) Imaginary dielectric function and (b) layer dependent absorbance spectra of single-layer, bilayer, three-layer, and four-layer (1L, 2L, 3L, and 4L) *h*-AlN. The comparison with bulk *h*-AlN crystal is shown as an inset.

for the *GW* calculations was increased to a maximum of 384. The excitonic effects were considered by undertaking the eight highest occupied valence- and ten lowest unoccupied conduction-bands.

Optical response functions presented in the upcoming discussions are expressed with the following relations. The calculated frequency dependent complex dielectric function (vide supra) enables a variation of the linear optical spectral quantities such as the layer dependent absorbance [$A(\omega)$], optical conductivity $\sigma(\omega)$, absorption coefficient $\alpha(\omega)$, and Fresnel reflectivity $R(\omega)$.

Layer dependent absorbance is obtained from the imaginary dielectric function, as described below:

$$A(\omega) = \frac{\omega}{c} L \text{Im}\epsilon(\omega) \quad (8.1)$$

where c is the speed of light and L is the total size of the cell in layer-normal direction.

The optical conductivity is given by the relation:

$$\sigma(\omega) = \frac{\omega}{4\pi} \text{Im}\epsilon(\omega) \quad (8.2)$$

The absorption coefficient is defined in the following way:

$$\alpha(\omega) = \sqrt{2}\omega [(\epsilon_1(\omega)^2 + \epsilon_2(\omega)^2)^{1/2} - \epsilon_1(\omega)]^{1/2} \quad (8.3)$$

Frequency dependent reflectivity at normal incidence is given by:

$$R(\omega) = \left| \frac{\sqrt{\varepsilon(\omega)} - 1}{\sqrt{\varepsilon(\omega)} + 1} \right|^2 \quad (8.4)$$

where $\varepsilon(\omega)$ is the complex dielectric function.

8.2. Results and Discussion

Optical properties of bulk AlN crystal: The frequency dependent dielectric function of bulk AlN is calculated and compared with the experimental data in the literature (Li *et al.*, 2003; Loughin *et al.*, 1993). The optical response of the hexagonal (*h*-) and wurtzite (*wz*-) forms of bulk AlN investigated at the level of DFT-RPA is shown in Fig.8.1. The imaginary parts of the dielectric function [$\varepsilon_2(\omega)$] are denoted by the blue and green curves for the calculated and experimental data, respectively. For *h*-AlN, the main absorption peak of the calculated spectrum is situated around 8.6 eV, where the absorption phenomenon occurs the most intense. The onset of interband absorption resides near 4.4 eV, which appears slightly higher than the direct band-gap of 3.4 eV (Bacaksiz *et al.*, 2015), where the difference is most probably resulted from further band-to-band transitions with higher energy values. Another feature is the shoulder structure around both 6.8 eV and 7.3 eV. When compared, regarding the main peak position and the line shapes within imaginary dielectric function, the spectrum predicted by DFT-RPA is generally in good agreement with the experimental data (Loughin *et al.*, 1993). However, there is a 0.4 eV discrepancy between the onsets of absorption, as the experimental data indicates an absorption onset around 4.1 eV which could arise from the noise in the experimental spectrum, since the plot does not reflect the most up-to-date measurement techniques.

In a similar manner, Fig.8.1(b) displays $\varepsilon_2(\omega)$ of bulk *wz*-AlN. The onset of absorption is located around 4.2 eV, which is ~ 0.8 eV lower than the experimental value (Li *et al.*, 2003). This can be correlated with the underestimated band-gap at DFT-RPA level. The most significant feature is situated near 7.8 eV as a single peak, where the main peak splits into two for the experimental case. Above 10 eV, further peak features are observed for both spectra, with slight shifts from each other.

In summary, fair agreement with experimental data for both structures is indeed promising in the sense that despite the slight discrepancy within the absorption onset, the two plots match to a good extent especially regarding the most prominent peak of the spectrum. During the following discussions, for the sake of optimizing the computational expense, results of layer and strain dependent optical response calculations are presented

at the level of DFT-RPA, which is sufficient for qualitative comparisons. Nonetheless, for a more accurate description of the dielectric tensor, many-body effects play a significant role in determining the optical properties of 2D materials. Hence, they were employed for monolayer and bilayer h -AlN at the levels of quasiparticle G_0W_0 and excitonic effects within the solution of Bethe-Salpeter equation. The results and comparisons can be found in the final section.

Layer-Dependent Optical Properties of h -AlN: The results obtained from the investigation of the thickness dependent optical properties of h -AlN up to four layers and the correlation with the electronic structure will be presented in this section. Theoretical analysis on AlN nanofilms also indicate that the hexagonal phase is favoured energetically for small thicknesses (up to 12 layers)(Freeman *et al.*, 2006b). The optical response of monolayer, bilayer, three- and four-layered (1L, 2L, 3L, and 4L) h -AlN are analyzed by means of various optical spectra. To the best of our knowledge, related experimental data on the optical properties of single or few-layer h -AlN are not yet available in the literature, hence the results will be evaluated on the basis of theoretical calculations.

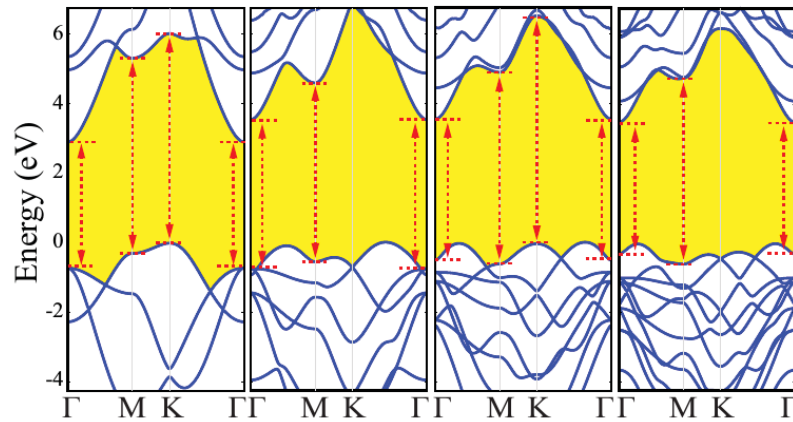


Figure 8.3. Electronic band structures of 1L, 2L, 3L, and 4L h -AlN. Zero level is set to the valence band maximum. Red arrows indicate important band-to-band (direct) transitions.

Although bulk h -AlN is a direct gap insulator, it was recently shown that its layered structure reveals an indirect gap character up to ten layers(Bacaksiz *et al.*, 2015). The differences in the band-splittings of bulk and layered h -AlN were stressed previously, which implies that diversity in the optical spectra should also be expected. In Fig.8.2, the

$\varepsilon_2(\omega)$ and $A(\omega)$ of 1L, 2L, 3L, and 4L h -AlN are plotted in the same graph. Monolayer h -AlN's absorption spectrum is denoted by the black curve, which displays an onset at 3.4 eV. On the other hand, the onsets of 2L, 3L, and 4L AlN appear almost at the same values, around 4.2 eV. This result can be expected from their band structures (Fig.8.3 since monolayer h -AlN reveals a band-gap (E_g) of 2.91 eV, where a prominent direct transition is observed at the Γ point with an energy of 3.65 eV. On the other hand, 2L, 3L, and 4L h -AlN have E_g of ~ 3.50 eV. This outcome is interesting as the layered structures except for monolayer act similarly and possess an onset closer to that of bulk h -AlN (4.5 eV). Moreover, 1L h -AlN exhibits a single distinct absorption peak around 6 eV, which is related with the important primary and secondary transitions at the Γ , M and K points with transition energies in the range of 5.6 to 7.2 eV. On the other hand, 2L h -AlN (blue line) displays rather scattered multi-peaks. The first one appears around 5.4 eV, second near 7.2 eV and third one above 9.4 eV. Next, 3L h -AlN (red line) shows a relatively broadened absorption phenomenon, with step-like features, leading to multi-peaks, occurring in the vicinity of 6.2 eV, 7.0 eV and a broader peak centred at 9 eV. Finally, 4L h -AlN (green line) displays the similar step-like features in its absorption spectrum, with a relatively broadened plateau in between 6.6 and 8.2 eV, followed by a prominent absorption region with highest amplitude around 8.6 eV. It is observed that at higher energies (especially as of 8 eV), $\varepsilon_2(\omega)$ and absorbance spectra display gradually increasing intensities, with the increase in the number of layers. Layer dependent absorbance [$A(\omega)$] which is shown in Fig.8.2(b) reveal that the absorbance increases gradually once the layer number increases, reaching to a maximum of $\sim 40\%$ for four-layered h -AlN, where this is much lower for the monolayer case. As can be deduced from the band structures of layered systems, the extra peaks of interband absorption come into play with contribution of additional layers. Moreover, when the optical spectrum of 4L h -AlN is compared to the one of bulk h -AlN which is shown as an inset of Fig.8.2(a), it is observed that they display similar features especially in between 5.2 to 6.8 eV. However an intense absorption occurs for bulk h -AlN in the range of 6.8-10.8 eV, with much higher amplitude with respect to the 4L h -AlN indicating that more layers are required to attain a bulk-like character.

Once the frequency dependent complex dielectric tensor is calculated, it is possible to obtain and compare various optical properties. Accordingly, the optical conductivity [$Im\sigma(\omega)$], absorption coefficient [$\alpha(\omega)$], and reflectivity spectra [$R(\omega)$] of 1L, 2L, 3L, and 4L h -AlN are calculated as a function of photon energy, $\hbar\omega$ and are exhibited in Fig.8.4. The former two graphs display, similar to the $\varepsilon_2(\omega)$, that the rather substantial absorption is restricted to a range between 4 eV to above 10 eV, predominantly in the

region above 8 eV, for all the systems of concern. Evidently, the peak intensities related to 4L h -AlN are the strongest, due to the well-distinguished broad peak around 9 eV. As for the frequency dependent reflectivity function, for all the systems, it is observed that the reflectance over the visible range and slightly above is generally quite small, which points out to a potentially transparent material.

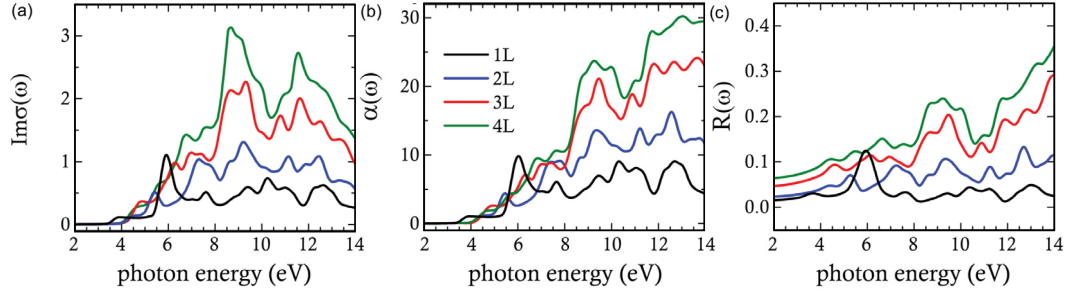


Figure 8.4. (a) Frequency dependent optical conductivity, (b) absorption coefficient and (c) reflectivity of 1L, 2L, 3L, and 4L h -AlN as a function of $\hbar\omega$.

Pointing to prominent optical absorption over the UV-range, layered h -AlN is also a promising material for optoelectronic applications. Considered as a significant input for potential nano-optoelectronic devices to be composed of layered h -AlN, the effective mass values for electron (m_e^*) and hole (m_h^*) are also calculated. The layer dependent m_e^* and m_h^* are presented in Fig.8.5. To obtain m^* , we fit the valence band maximum and conduction band minimum to a parabola, where the inverse of the second order term's coefficient, multiplied by a factor is considered as the m_e^* and m_h^* , respectively. Our results indicate that for 1L, m_e^* is equal to $0.50 m_0$ and decreases slowly as number of layer increases and converges to the bulk value. On the other hand, m_h^* is calculated to be $1.53 m_0$ for monolayer case and decreases dramatically upon increasing number of layers. It could be informative to make a comparison with some other 2D semiconducting systems. When only monolayer case is considered m_e^* is comparable to those of layered BN (Cao *et al.*, 2013) ($m_e^* = m_h^* = 0.54 m_0$) and monolayer MoS₂ (Peelaers and Van de Walle, 2012) ($m_e^* = 0.37$ - $0.38 m_0$ and $m_h^* = 0.44$ - $0.48 m_0$). However, m_h^* is significantly higher than both monolayer BN and MoS₂. The range and variation of effective mass and electronic band-gap suggest that layered h -AlN is a promising candidate material for next generation electronic devices.

Finally, the effect of spin-orbit (SO) coupling on the optoelectronic properties should be considered too, since it can be significant for 2D systems. For instance, despite

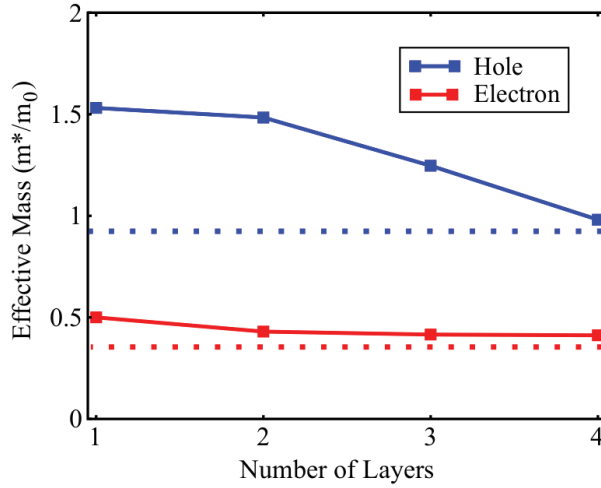


Figure 8.5. The variation of electron (red line) and hole effective mass (blue line) with respect to the number of layers. The bulk values are shown by dashed lines.

the 1 meV SO splitting in silicene(Liu *et al.*, 2011), the SO splitting of germanene is calculated to be 23 meV(Ozcelik *et al.*, 2014). In this sense, SO coupling was also taken into account in our calculations. The SO splitting is calculated to be 8 meV for monolayer *h*-AlN. Its effect on the optical properties was found to be negligible, based on an evaluation of the $\varepsilon_2(\omega)$ of monolayer *h*-AlN.

Strain-Dependent Optical Properties of *h*-AlN: In addition to the layer-dependence, the optical properties of monolayer *h*-AlN are also investigated under the influence of biaxial tensile strain. Theoretical studies on nanofilms of AlN (and also other wurtzite materials) reveals that the the thickness range of stable hexagonal phase depends on strain and can be extended to thicker films by epitaxial tensile strain(Wu *et al.*, 2011). We apply strain at values of 1%, 3%, 5% and 7% since higher stress values can induce instability and are also very difficult to achieve for practical applications, hence are not considered here. Strain can be caused by loading or the underlying substrate, and is a relevant phenomenon for 2D materials due to the rather large tensile strain obtained experimentally. The variation of $\varepsilon_2(\omega)$ of monolayer *h*-AlN with strain is shown in Fig.8.6(a). The first observation reveals that the spectra are globally shifted toward lower photon energies, in a general manner. The gradual shift is almost uniform and increases with the amount of applied strain. In order to understand the origin of the shift and relate with the electronic structure, we also calculated strain dependent band structure of monolayer *h*-AlN

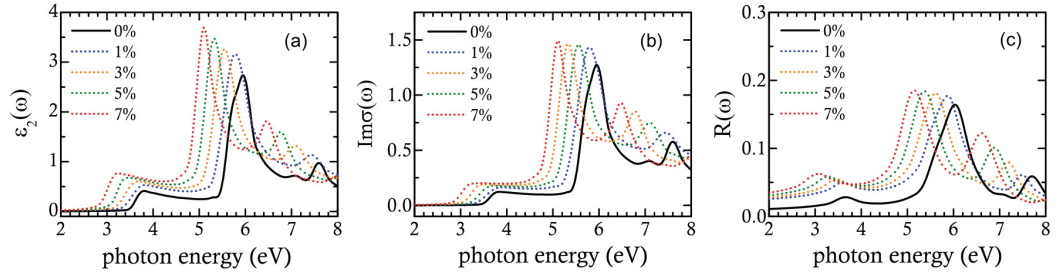


Figure 8.6. (a) Imaginary dielectric function, (b) absorption coefficient and (c) frequency dependent reflectivity of single-layer h -AlN under strain. Black solid curve stands for the unstrained case and dashed lines for strain values of 1%, 3%, 5% and 7%, respectively.

(Fig.8.7. Biaxial strain is naturally expected to alter the electronic properties. More precisely, increasing or decreasing the bond length as well as confinement effects can modify the electronic structure. Our analysis indicates that the E_g values are also reduced monotonically as the strain value is increased. The decrease in E_g can be attributed to the modification of orbitals under strain. Partial density of states analysis shows that except for p_z orbital of Al and N atoms, with increasing strain, the orbitals and the corresponding bands are placed at lower energy both in the valence and conduction bands. More explicitly, the energies of s and p_{xy} orbitals decrease relative to p_z orbitals which is plausible since the s and p_{xy} orbitals are effected by confinement in the direction of strain. On the other hand, the p_z orbitals which are out of plane of the structure are influenced very little. Therefore, the decrease in E_g values under strain can be explained by the difference between in plane and out of plane orbitals.

Next, we analyze the change in the optical spectra quantitatively via a global joint density of states-like spectrum (obtained as $\varepsilon_2(\omega)^2 \cdot \text{photon energy}$). The three quantities yielded by this analysis are the absorption onsets (Onset-I indicates the first step-like increase in the spectrum and Onset-II refers to the value at which the prominent absorption peak kicks-off) and the main peak position.

Regarding the absorption onset values, Onset-I varies from 3.45 to 2.80 eV, upon being subjected to tensile strain. The average difference among the onset values come out as 0.16 eV. Next, it is seen that the Onset-II varies from 5.45 to 4.70 eV, pointing to an average shift of 0.18 eV. Both shifts are toward lower photon energies. The third feature to be discussed in Fig. 8.6(a) and Table 8.1 is the main absorption peak's position;

Table 8.1. Optimized lattice constant, band-gap, absorption onset and absorption peak position values of strained h -AlN

	Lattice constant (Å)	Band-gap (eV)	Onset-I (eV)	Onset-II (eV)	PL peak (eV)
Unstrained	3.13	2.91	3.45	5.45	5.93
1%	3.16	2.8	3.32	5.23	5.82
3%	3.22	2.6	3.22	5.10	5.54
5%	3.28	2.4	3.05	4.89	5.32
7%	3.44	2.1	2.80	4.70	5.10

which is redshifted by approximately 0.24 eV from 1% to 7% strain. The feature most affected by the applied strain is the peak position, followed by the onset values. It is no surprise that in-plane tensile strain tunes the optical properties in such a way that the absorption spectrum is regularly (globally) redshifted as shown in Fig. 8.6(b)-(c), well known for electronic properties and also from some recent work on the optical properties of 2D materials(Shi *et al.*, 2013b). In conclusion, the optical spectra of 2D monolayer h -AlN are also quite sensitive to biaxial tensile strain, as well as its electronic properties, which is promising for the potential optoelectronic applications by strain engineering.

Many-body calculations of the optical properties of monolayer and bilayer h -AlN:

As the prominence of many-body effects in the excited states properties of band-gap materials is well known, the optical absorption spectra of specific cases; monolayer and bilayer h -AlN were also calculated at higher levels of accuracy. The hybrid functionals and non-self consistent quasiparticle G_0W_0 within RPA were used. The electron-hole ($e-h$) interactions taken into account by solving the BSE details of which are given in the methodology part. Results of the comparison between the different methods and number of layers are shown in Fig.8.8. As seen on the upper panel (a), the spectrum of single-layer h -AlN given by the HSE-RPA calculation (orange plot) is globally shifted towards higher frequencies by nearly 1 eV with respect to its PBE-RPA counterpart (black plot). Likewise, the absorption onset value is higher than that of PBE by slightly above 1 eV. The absorption peak position given by HSE appears around 7 eV, which is not surprising since the correction of band-gap by hybrid functionals, thus the optical gap, is a common trend. As exhibited by the red plot, the single-shot G_0W_0 yields a further blueshifted optical response, with a main peak residing around 8 eV. Regarding both the absorption

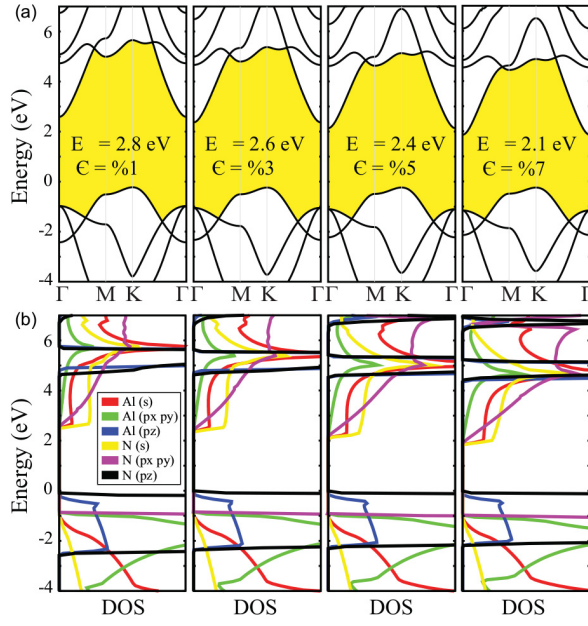


Figure 8.7. (a) Strain dependent band structures indicating the variation of the band-gap values (E) and (b) partial densities of states of monolayer h -AlN.

onset (slightly below 5.5 eV) and peak positions, G_0W_0 method reveals a global blueshift with respect to PBE- and HSE-RPA spectra.

The absorption spectra of monolayer (blue plot) and bilayer (green plot) structures given by single-shot G_0W_0 -BSE calculation are displayed in the lower panel (b) of Fig.8.8. Accordingly, for single-layer h -AlN, two sharp peaks are located at 4.0 and 5.38 eV (also a small shoulder at 5 eV), former being closer to the optically active region. The optical transitions below the G_0W_0 optical gap (green plot with squares) indicate a resonant light-matter coupling present in monolayer AlN with wide electronic gap, arising from the excitonic transitions. Similarly, the BSE spectrum of bilayer AlN displays a major peak at nearly 5 eV and a second non-sharp feature around 6 eV, both below the band-gap yielded by G_0W_0 . Hence, the optical features for both structures are substantially dominated by the excitonic effects, pointing to strongly bound excitons, due to the $e-h$ interactions stemmed from weak screening in wide-gap low-dimensional AlN. Our results for monolayer AlN are in good agreement with those in a recently published work (Fakhrabad *et al.*, 2015) where a bright exciton binding energy was found as 2.05 eV. This is slightly higher than what we have observed; ≈ 1.7 eV, where for bilayer h -AlN it was found to be higher, nearly 2.2 eV, as the band-gap is opened up compared

to the monolayer case. As for the comparison with other 2D materials with significant band-gaps, the binding energies are revealed as nearly 0.8 eV(Vy *et al.*, 2014), close to 1 eV(Qiu *et al.*, 2013) and 2.1 eV(Wirtz *et al.*, 2006) for monolayer phosphorene, MoS₂ and BN, respectively. Moreover, the exciton binding energy of layered AlN is substantially higher than that of its wurtzite structure (1 μm thick film), measured as 80 meV(Li *et al.*, 2003) and AlN films, of 63 meV(Silveira *et al.*, 2004). Evidently, the strongly bound excitons underline that for layered *h*-AlN, $e - h$ effects can be significant to enhance the optical features in the absorption spectrum.

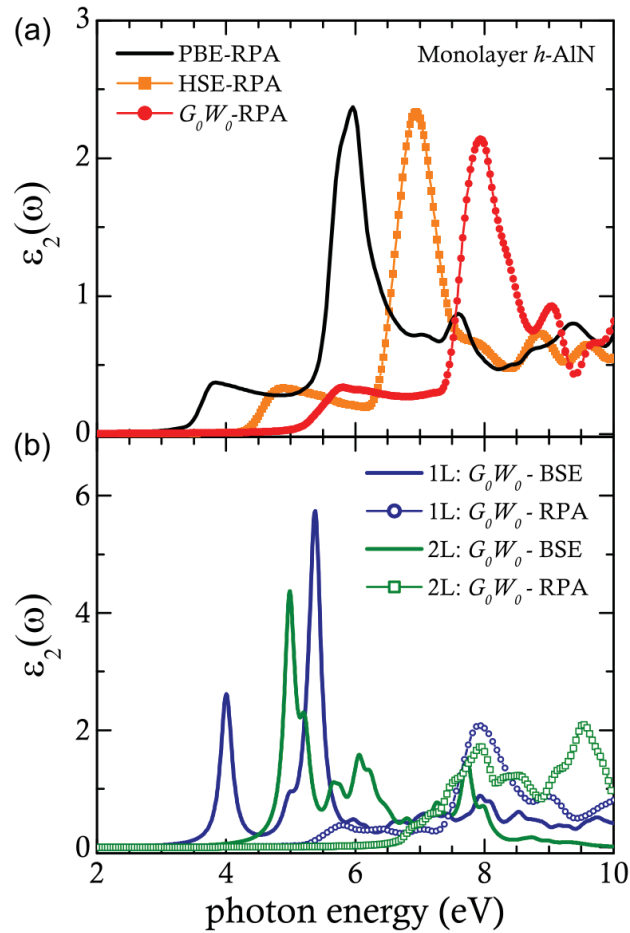


Figure 8.8. Many-body calculations of the optical response of monolayer and bilayer *h*-AlN (a) Comparison of RPA-spectra based on PBE, HSE and G_0W_0 calculations for monolayer *h*-AlN and (b) Optical spectra of mono- and bilayer *h*-AlN with electron-hole interactions taken into account.

8.3. Conclusions

In conclusion, we examined in detail the layer and strain dependent optoelectronic properties of h -AlN starting from its bulk crystal form (Kecik *et al.*, 2015). We calculated the layer dependent absorbance, optical conductivity, absorption coefficient, and frequency dependent reflectivity and investigated their variation with the increasing number of layers. The absorbance was found to increase when more layers were considered. In general, prominent optical absorption was observed to occur within the UV-range, promising for optoelectronic applications aimed for the ultraviolet spectral region. Hence, the layered forms of h -AlN are expected to display rather transparent features in the visible light range. Furthermore, our results indicated that the absorption spectrum is globally redshifted under the applied strain. The electronic properties of layered h -AlN were also computed in order to clarify their relation with the optical spectra. The bandgaps, similarly to the interband absorption onsets, were found to vary with the increasing number of layers and amount of strain. While the many-body corrections to the optical response calculations of h -AlN induced blueshifted spectra in general, evidence of bound excitons were also found for the layered structures of AlN. In summary, it was shown that the optoelectronic properties of layered h -AlN can be controlled and tuned by modifying their structure and applying strain. Since extensive knowledge of the optical properties of layered AlN is prominent for future device applications, the theoretical findings in this work can further enlighten investigations focusing on the design of optoelectronic devices made of 2D h -AlN.

CHAPTER 9

h -AlN-Mg(OH)₂ vdW BILAYER HETEROSTRUCTURE

Beside the single crystal of 2D materials, recently emerging field is their vertically stacked heterostructures (Geim and Grigorieva, 2013). Because of the van der Waals type weak interlayer interaction, the synthesis of heterostructures is not restricted with the lattice matching of the each layers. This provides a wide variety of combinations of layers which exhibit different electronic and optical properties (Lee *et al.*, 2014; Britnell *et al.*, 2012; Fang *et al.*, 2014; Ferrari *et al.*, 2015; Hong *et al.*, 2014; Hunt *et al.*, 2013; Tan and Zhang, 2015).

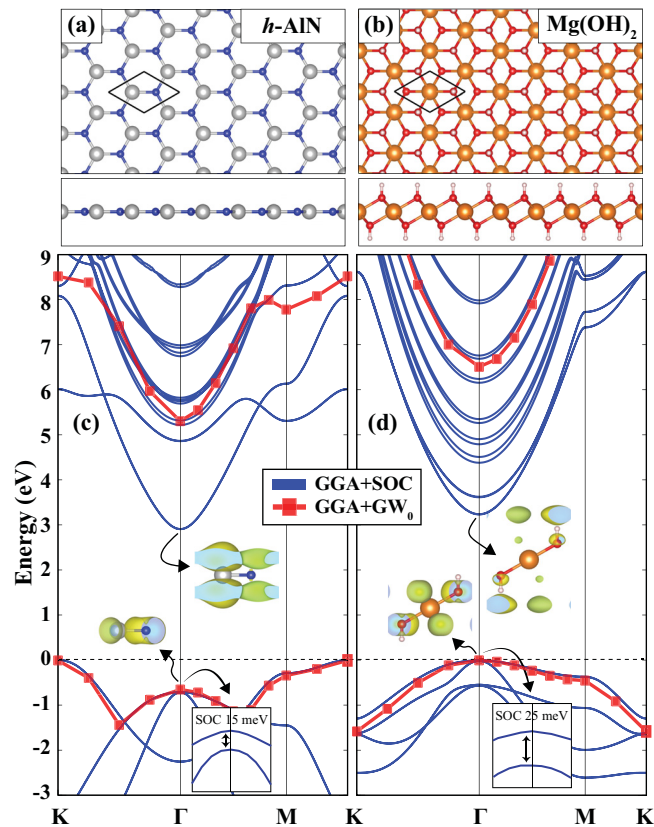


Figure 9.1. (a) and (b) are the structures (top and side view) of monolayer h -AlN and $Mg(OH)_2$, (c) and (d) are the band structures of h -AlN and $Mg(OH)_2$, respectively. The blue and light-red curves with square are for GGA+SOC and GGA+ GW_0 , respectively.

Stable hexagonal crystalline structure of AlN was first theoretically predicted by Sahin *et al.* (Sahin *et al.*, 2009). and experimentally synthesized by Tsipas *et al.* (Tsipas *et al.*, 2013) They found that, differing from its bulk structure which is an insulator, monolayer *h*-AlN is a semiconductor with the indirect band gap where the valence band maximum and conduction band minimum at the K and Γ points, respectively. Almeida *et al.* (De Almeida *et al.*, 2012) investigated properties of defects, such as vacancies, antisites, and impurities, in *h*-AlN. It was reported that N vacancies and Si impurities lead to the breaking of the planar symmetry and cause significant changes in the electronic properties. Shi *et al.* (Shi *et al.*, 2014) calculated the magnetic properties of bare and transition-metal (TM) doped AlN nanosheets by using first-principles calculations. They reported that nonmagnetic *h*-AlN can be magnetized upon a single TM atom. Moreover, the electronic structures of nanoribbon of AlN were investigated by Zheng *et al.* (Zheng *et al.*, 2010) and it is predicted that zig-zag edge nanoribbons have an indirect band gap while armchair edge nanoribbons have a direct band gap, and band gaps of both zig-zag and armchair decrease monotonically with increasing ribbon width. Furthermore, Bacaksiz *et al.* (Bacaksiz *et al.*, 2015) reported that the electronic band structure changes significantly when the number of layer increases and the structure having 10 or more layers exhibits direct bandgap as bulk form. More recently, Kecik *et al.* (Kecik *et al.*, 2015) investigated the optical properties of mono- and few-layer *h*-AlN under strain. They reported that the absorption peaks stand outside the visible-light regime, on the other hand, the applied tensile strain gradually redshifts the optical spectra.

As a constituent of hetero-bilayer, physical properties of $\text{Mg}(\text{OH})_2$ were investigated previously in several studies (Ding *et al.*, 2001; Sideris *et al.*, 2008; Utamapanya *et al.*, 1991). It is a layered metal hydroxide with a wide band gap (Murakami *et al.*, 2011). As a member of the alkaline-earth-metal hydroxides (AEMHs) family, $\text{Ca}(\text{OH})_2$ was predicted to be stable in the bilayer and monolayer forms by Aierken *et al.*? In addition, Torun *et al.* investigated the optical properties of $\text{GaS-Ca}(\text{OH})_2$ bilayer heterostructure by using GW+BSE and reported that in spite of the similarities of electronic structures, the different stacking types have different optical spectra (Torun *et al.*, 2016). Recently, Tsukanov *et al.* investigated the interaction of organic anions with layered double hydroxide nanosheets consist of Mg and Al by using molecular dynamics simulations (Tsukanov and Psakhie, 2016). In addition, very recently, the monolayer $\text{Mg}(\text{OH})_2$ was synthesized and reported that in spite of the optically inactive nature of $\text{Mg}(\text{OH})_2$, the photoluminescence intensity of monolayer MoS_2 was assisted by $\text{Mg}(\text{OH})_2$ and enhanced (Suslu *et al.*, 2016). Most recently, Yagmurcukardes *et al.* investigated the hetero-bilayer of the

Mg(OH)₂ and WS₂(Yagmurcukardes *et al.*, 2016). They reported that the lower energy optical spectrum of the Mg(OH)₂-WS₂ hetero-bilayer is dominated by the excitons originates WS₂ layers. These two studies indicate that the Mg(OH)₂ is a candidate for tuning the optical property of other monolayer materials.

In the present work (Bacaksiz *et al.*, 2017), the heterostructure of two perfectly-matching monolayers of *h*-AlN, a member of III-V binary compounds, and Mg(OH)₂, a member of alkaline-earth-metal hydroxide (AEMH), are considered. The similar lattice constants of the layers provide us to use smaller supercell which is important especially for the calculating the optical properties. We found that the vertically stacked heterostructure possesses excitonic peaks which appear only after the construction of the hetero-bilayer. More significantly, the wave function calculation shows that the first peak of the imaginary part of the dielectric function for the hetero-bilayer originates from spatially indirect exciton where the electron and hole localized at *h*-AlN and Mg(OH)₂, respectively.

Table 9.1. Calculated parameters for monolayer *h*-AlN and Mg(OH)₂ are the lattice constant in the lateral direction, *a*; the final charges of Al, N, Mg, O, and H, ρ_{Al} , ρ_N , ρ_{Mg} , ρ_O , ρ_H , respectively; the work function Φ ; the cohesive energy, E_{coh} ; and the spin-orbit splitting, Δ_{SO} . E_g^{GGA} and $E_g^{GW_0}$ are the energy band gap values within GGA+SOC and GGA+GW₀, respectively.

	<i>a</i> (Å)	ρ_{Al} (e ⁻)	ρ_N (e ⁻)	ρ_{Mg} (e ⁻)	ρ_O (e ⁻)	ρ_H (e ⁻)	Φ (eV)	E_{coh} (eV)	E_g^{GGA} (eV)	Δ_{SO} (meV)	$\Gamma \rightarrow \Gamma$ (eV)	$E_g^{GW_0}$ (eV)
<i>h</i> -AlN	3.13	0.7	7.3	-	-	-	5.12	5.35	2.90	15	3.62	5.37 (<i>K</i> - Γ)
Mg(OH) ₂	3.13	-	-	0.3	7.4	0.4	4.20	4.38	3.23	25	3.23	6.51 (Γ - Γ)

9.1. Computational Details

In addition to the methodology given in Sec. 2.4 the following details are particular for this study. The quasi-particle (QP) energies were calculated within the GW₀ approximation where the single-particle Green function part (G) was iterated and the screened Coulomb interaction part (W) was fixed. On top of GW₀ approximation, the energies of two particle system of quasi-electron and quasi-hole (exciton) were calculated by solving BSE(Hanke and Sham, 1980; Salpeter and Bethe, 1951). To obtain accurate QP states, 320 bands were considered in the GW₀ calculations. Our convergence tests

showed that the $12 \times 12 \times 1$ k-point sampling and the vacuum spacing of $\sim 28 \text{ \AA}$ well approximates the excitonic properties of vdW hetero-bilayer structure. The 8 highest valence bands and lowest conduction bands were considered as a basis for the excitonic states.

9.1.1. Convergence Tests

Theoretical results on optical properties, especially many-body and excitonic effects, strongly depend on computational parameters such as Brillouin Zone sampling and the vacuum spacing between the adjacent layers. The calculation with fine parameters, on the other hand, requires large computational resource and time. Therefore, we performed calculations to examine the convergence of the frequency dependent imaginary dielectric function with respect to k-point sampling and the vacuum spacing.

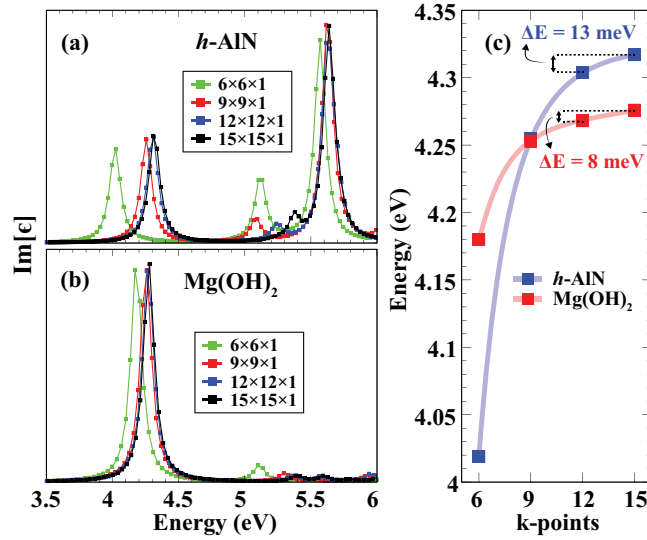


Figure 9.2. The results of the k-point sampling tests: (a) and (b) The imaginary part of the dielectric functions of the monolayer $h\text{-AlN}$ and $\text{Mg}(\text{OH})_2$ for different k-point samplings, respectively. (c) The first exciton peak positions are shown as the blue and red squares for the monolayer $h\text{-AlN}$ and $\text{Mg}(\text{OH})_2$, respectively.

The imaginary part of the dielectric function for the monolayer $h\text{-AlN}$ and $\text{Mg}(\text{OH})_2$ with respect to k-point sampling are shown in Fig. 9.2 (a) and (b), respectively. When the number of k-points increases, the spectrum of both monolayers are blue-shifted and

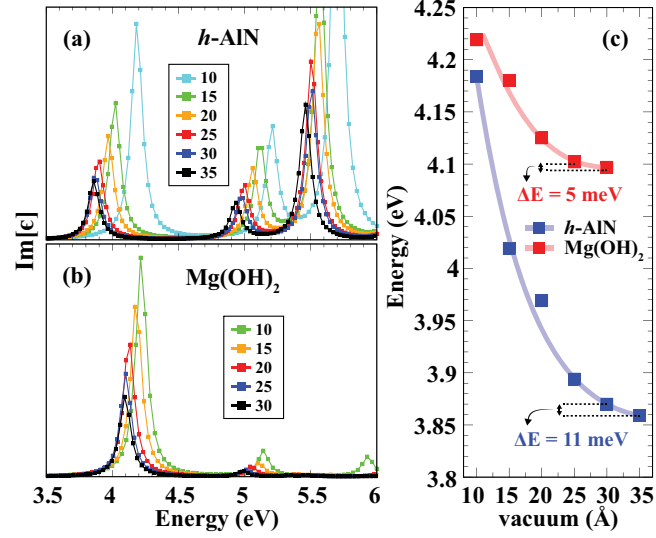


Figure 9.3. The results of vacuum spacing tests: (a) and (b) The imaginary part of the dielectric functions of the monolayer $h\text{-AlN}$ and $\text{Mg}(\text{OH})_2$ for different vacuum spacing values, respectively. (c) The first exciton peak positions are shown. The blue and red curves correspond to the monolayer $h\text{-AlN}$ and $\text{Mg}(\text{OH})_2$, respectively.

rapidly converges by the $12 \times 12 \times 1$ sampling (see Fig. 9.2 (c)). Therefore, using $12 \times 12 \times 1$ for optical properties of monolayer $h\text{-AlN}$ and $\text{Mg}(\text{OH})_2$, provides reliable results.

As shown in Fig. 9.3 (a) and (b), the effect of the vacuum spacing is also evident that the peak positions of both monolayers are red-shifted. For the $h\text{-AlN}$, the curves of 30 and 35 Å vacuum spacing values are almost the same. For $\text{Mg}(\text{OH})_2$, the curve does not change significantly when the vacuum spacing increases from 25 to 30 Å. Moreover, as shown in Fig. 9.3 (c), the difference between the first exciton energies of 30 and 35 Å vacuum spacing values is 11 meV for the monolayer $h\text{-AlN}$. The smaller energy difference of 5 meV is obtained between 25 and 30 Å vacuum spacing values for the monolayer $\text{Mg}(\text{OH})_2$. It is clearly seen that, the vacuum spacing of 30 and 25 Å are sufficient for the monolayers $h\text{-AlN}$ and $\text{Mg}(\text{OH})_2$, respectively. Therefore, when we consider the hetero-bilayer, using the vacuum spacing of ~ 28 Å for optical properties provides reliable results. After having convergence tests, the best parameter set of $12 \times 12 \times 1$ kpoint and 28 Å vacuum spacing are used in our calculations.

9.1.2. Methodology for Determination of Excitonic Wave Functions

For a deeper understanding of the origin of excitonic states and determination of their wave functions of the vdW hetero-bilayer, three lowest exciton wave functions were calculated by using BerkeleyGW package(Deslippe *et al.*, 2012) on top of QuantumEspresso code(Giannozzi *et al.*, 2009). The eigenvalues and the eigenfunctions in the independent particle picture were obtained by using PBE form of GGA for exchange and correlation. The quasi-particle energies were calculated within the GW approximation. We employed an energy cutoff of 160 Ry for the PBE calculations. For the computation of the dielectric matrix, we used 1987 conduction bands and G-vectors with energy up to 17 Ry, whereas the self-energy operator was computed using 1987 conduction bands and a G-vector cutoff of 17 and 160 Ry for the screened and bare Coulomb matrices, respectively. To sample the BZ we employed a $6 \times 6 \times 1$ k-point grid for the PBE and GW calculations, whereas for the solution of the BSE, we used a $18 \times 18 \times 3$ k-point grid with linearly interpolated GW quasi-particles energies. The 8 lowest conduction bands and 8 topmost valence bands were included to solve the BSE. After obtaining the excitonic states, the probability of localization of the electron is calculated for each excitonic level when the hole is fixed to a specific point. The result are given in Fig. 9.7 (b).

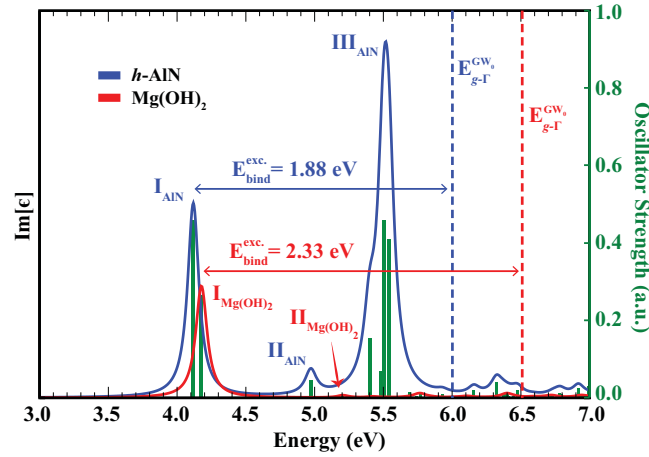


Figure 9.4. The imaginary part of the dielectric function of h -AlN (blue curve) and $\text{Mg}(\text{OH})_2$ (red curve) with oscillator strength of excitonic states (vertical green lines). The first, second and third excitons are labeled as I, II, III with the subscript of the corresponding individual layer, respectively. The quasi-particle band gap of h -AlN (blue dashed) and $\text{Mg}(\text{OH})_2$ (red dashed) at Γ and exciton binding energies ($E_{bind}^{exc.}$) are given.

9.2. Single Layer h -AlN and $\text{Mg}(\text{OH})_2$

Before analysis of bilayer heterostructure of h -AlN and $\text{Mg}(\text{OH})_2$, the monolayer constituents are discussed. Firstly, the monolayer structure of h -AlN (see Fig. 9.1(a)) belongs to space group $P6_3/mmc$ with the lattice constant 3.13 \AA which is consistent with that of few-layer hexagonal AlN that reported by Tsipas and the co-workers (Tsipas *et al.*, 2013). In Table 9.1, the number of valance electrons of the isolated single atom and of the one in crystal are given. It is seen that Al donates 2.3 of $3.0 e^-$ to N which indicates that the bond between Al and N have strong ionic character. The work function is found to be 5.12 eV. As shown in Fig. 9.1(c), h -AlN has an indirect band gap of 2.9 eV where the valance band maximum (VBM) and the conduction band minimum (CBM) are at the Γ and K points, respectively. GW_0 band gap is calculated to be 5.30 eV. In addition, differing from similar TMDs, the spin-orbit (SO) splitting at the Γ point is quite small (15 meV) (Mak *et al.*, 2010).

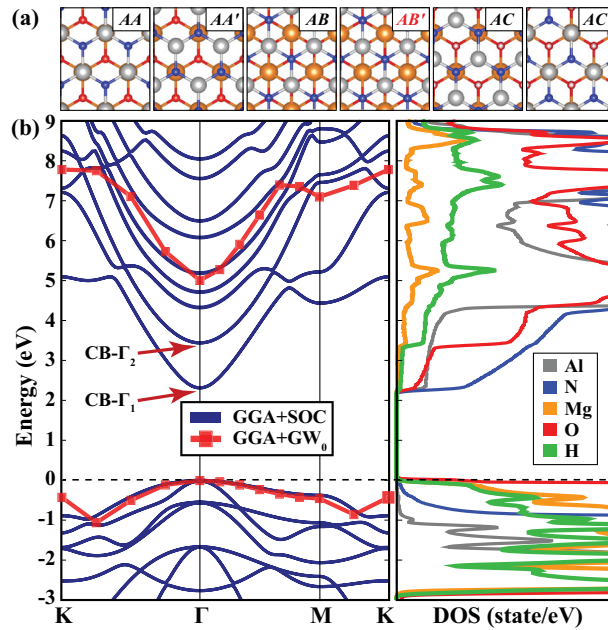


Figure 9.5. (a) Top view of six different stacking orders, (b) Electronic band dispersion (left panel) and the partial density of state (right panel) of AB' stacking order. The $\text{CB-}\Gamma_1$ and $\text{CB-}\Gamma_2$ label the first and second lowest levels of the CB at Γ point, respectively.

Structural and electronic properties of monolayer $\text{Mg}(\text{OH})_2$ which is another building-block of hetero-bilayer are also presented in Figs. 9.1(b) and (d). The lattice parameter

of Mg(OH) which belongs to $P\bar{3}m1$ space group is found to be 3.13 Å. Therefore, it perfectly matches to h -AlN. Upon the formation of this crystalline structure In this structure: (i) Mg donates almost all valance electrons, 1.8 of 2.0 e^- , and (ii) H donates 0.6 of 1.0 e^- to O atom. The work function is calculated to be 4.20 eV. Mg(OH)₂ has direct band gap of 3.23 eV, 6.51 within GGA and GGA+GW₀, respectively. The wide GW₀ band gap is close to the value which is previously obtained(Suslu *et al.*, 2016). The SO splitting at the Γ is 25 meV which is slightly larger than that of h -AlN (15 meV). This small difference can be understood from the difference between the atomic radius of N and O atoms.

In Fig. 9.4, the energy dependency of the imaginary part of the dielectric function of pristine h -AlN and Mg(OH)₂ are shown. We name the peaks as I, II, and III (first, second and third, respectively) with the subscript that specify the corresponding individual layer. The I_{AlN} appears at 4.12 eV with the exciton binding energy of 1.88 eV. The II_{AlN} and III_{AlN} appear at 4.97 and 5.4 eV, respectively. The III_{AlN} consists of 4 exciton levels. The $I_{Mg(OH)_2}$ and $II_{Mg(OH)_2}$ appear at 4.18 and 5.20 eV, respectively. The excitonic binding energy of the $I_{Mg(OH)_2}$ is found to be 2.33 eV. The peaks of the h -AlN are larger than those of Mg(OH)₂. The reason is that all the peaks shown in Fig. 9.4 originate from the excitation at the Γ , hence the overlapping of electron and hole states are larger for the h -AlN which is clearly seen at the charge density of band edges in Fig. 9.1. In addition, the excitonic binding energies are larger compared to the bulk materials. Such binding energies were previously reported and discussed(Cudazzo *et al.*, 2016; Pishtshev *et al.*, 2014; Wirtz *et al.*, 2006).

9.3. Bilayer Heterostructure

In this section, we give an analysis of structural, electronic and optical properties of bilayer heterostructure of vertically stacked monolayer h -AlN and Mg(OH)₂.

Determination of Stacking Type: First of all, to determine energetically favorable structure, six different stacking orders are considered. As shown in Fig. 9.5(a), possible stacking orders are: AA (Al on Mg, N on H), AA' (N on Mg, Al on H), AB (Al on H, N at the midpoint of three H), AB' (N on H, Al at the midpoint of three H), AC (Al and N on top of midpoint of H triangles and N on Mg), and AC' (switched of Al and N form of AC). The energy difference between different stackings are given in Table 9.2. In general, the hetero-bilayer has three type of properties with respect to localization of Al or N on trigonal H surface of Mg(OH)₂; when N atom is on top of H atom, which means

Table 9.2. The stacking labels are given in the first column. Calculated parameters for bilayer heterostructure of h -AlN and $\text{Mg}(\text{OH})_2$ are; the interlayer distance, d_{L-L} ; the energy difference between the ground state, Δ_E ; the interaction energy between the layers, E_{int} ; and the work function Φ . E_g^{GGA} are the energy band gap values within GGA+SOC.

	d_{L-L} (Å)	Δ_E (meV)	E_{int} (meV)	Φ (eV)	E_g^{GGA} (eV)
AB'	2.13	0	237	4.31	2.30
AA	2.12	6	231	4.32	2.31
AC	2.06	66	171	4.70	2.65
AC'	2.10	76	161	4.69	2.61
AA'	2.75	162	75	4.35	2.14
AB	2.75	164	73	4.29	2.14

the AB' and AA stacking types, the hetero-bilayers possess the lowest energies with highest binding energies. They have also similar band gap of 2.30 and 2.31 eV, respectively. The work functions are found to be 4.31 and 4.32 eV which are very close to each other. Instead of these energetically favorable forms, the minimum interlayer distances are obtained when the Al and N atoms coincide to the midpoint H triangles (AC' and AC'). The band gap and work function values of the AC' and AC' stacking are found to be similar as well. When Al is on top of H, the structures have the highest interlayer distances, highest energy and lowest binding energy. The AA with AB' , AA' with AB , and AC with AC' have similar parameters.

The minimum energy of the hetero-bilayer is obtained when the layers are stacked in the form of AB' stacking which exhibits the maximum interlayer interaction of 237 meV. Interlayer distance, which is defined as the perpendicular distance from surface H atom to the h -AlN plane, is 2.13 Å. The work function of $\text{Mg}(\text{OH})_2$ side is calculated to be 4.31 eV. The VBM and CBM are at Γ as in monolayer $\text{Mg}(\text{OH})_2$, however the band gap values of 2.30 eV within GGA which are significantly low as compared to that of monolayer of h -AlN and $\text{Mg}(\text{OH})_2$. In addition, the AA stacking order is energetically very close to AB' . For both AB' and AA , the layer-layer interaction, interlayer distances, and also band gap values are almost same.

In addition, considering vacuum level positions, formation of a staggered gap, with a mismatch of 1.02 eV at the intimate contact point of monolayers is predicted. Moreover, Since the minimum energy difference between the VB and CB is at Γ point

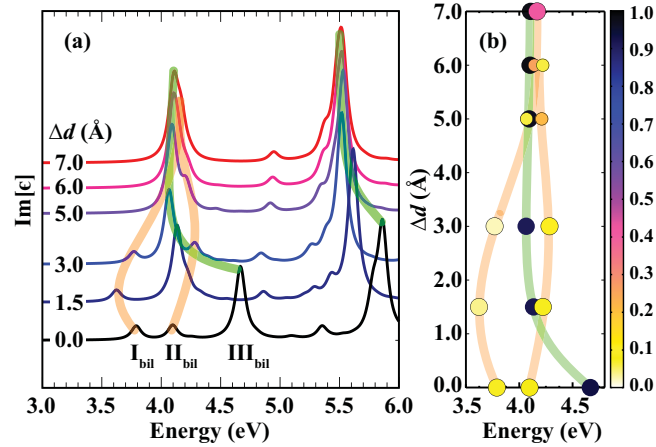


Figure 9.6. (a) The imaginary part of the dielectric functions of the AB' stacked hetero-bilayer are shown for different interlayer distances starting from ground state distance of 2.13 \AA . Δd refers to interlayer distance while the ground state distance is set to 0 and labeled as 0.0 \AA . The lowest three exciton peaks are labeled as I_{bil} , II_{bil} , and III_{bil} . (b) The distance dependent oscillator strengths of lowest three excitons are shown.

(see Fig. 9.5 (b)), the lower energy optical activity takes place at this high symmetry point of Brillouin Zone. Such a contact between two atomically-flat surfaces forms an ultra-clean Type-II heterojunction.

Origin of Excitonic States of Bilayer Heterostructure: In this part, the origin of the prominent excitonic peaks in the $\text{AlN}/\text{Mg}(\text{OH})_2$ hetero-bilayer structure, which corresponds to the AB' stacking, are investigated in details. There are two effects that determine characteristic properties of exciton in two-dimensional materials: the dielectric screening and the structural confinement. In general, when the crystal structure of a usual semiconductor is reduced from 3D to 2D, the dielectric screening between electron and hole takes place only inside layer. Therefore, as a consequence of the dimensional reduction, the screening effect on electron-hole pair is lower for 2D crystals as compared to the bulk.

In Fig. 9.6, we show interlayer-spacing-dependent excitonic properties to investigate the origin and evolution of the excitons by tracking their peak positions and corresponding oscillator strengths in the energy spectrum.

As shown in Fig. 9.6 (a), starting from the interlayer spacing of 6.0 \AA (equilibrium distance is set to 0 \AA), the first peak of the isolated $\text{Mg}(\text{OH})_2$ splits into two different peaks

due to the broken symmetry of the top and bottom surface charge densities. It is seen that the first peak of the bilayer structure, \mathbf{I}_{bil} , appears at the lower energy level than the first peak of both individual h -AlN and $\text{Mg}(\text{OH})_2$. As calculated in the previous section, the VBM and CBM electronic states are mainly formed by the O and N, respectively. Therefore, the first peak of the bilayer heterostructure, \mathbf{I}_{bil} , corresponds to a spatially indirect exciton in which the electron localizes at the N of h -AlN and the hole is at O of $\text{Mg}(\text{OH})_2$. As shown in Fig. 9.6 (b), the reduction in the oscillator strength of \mathbf{I}_{bil} (minimum of all) at around 3.0 Å, reveals that electronic state of $\text{Mg}(\text{OH})_2$ at the intimate contact surface overlaps with h -AlN layer as the distance decreases. However, at the optimum interlayer distance, other $\text{Mg}(\text{OH})_2$ -originated exciton state evolves into the second peak of the heterostructure labeled as \mathbf{II}_{bil} . Apparently, the electronic state of \mathbf{II}_{bil} exciton peak originates from the outer surface state of $\text{Mg}(\text{OH})_2$.

On the other hand, the origin and interlayer-spacing-dependence of \mathbf{III}_{bil} , differs from those of \mathbf{I}_{bil} and \mathbf{II}_{bil} . Firstly, in Fig. 9.6, it is evident that by decreasing interlayer spacing the first excitonic peak of h -AlN crystal gradually evolves into third state of hetero-bilayer, labeled as \mathbf{III}_{bil} . It is seen from Figs. 9.6 (a) and (b) that the shape and the oscillator strength of the \mathbf{III}_{bil} do not change significantly. Therefore, one can conclude that the characteristic properties of the \mathbf{III}_{bil} are almost same with the first excitonic state of h -AlN monolayer crystal. When the distance decrease under 4.0 Å, a significant charge distribution appears on the O atom. It appears that the screening on the h -AlN increases when the $\text{Mg}(\text{OH})_2$ layers become closer. Therefore as a consequence of decrease in exciton binding energy corresponding peak shows a significant blue shift.

For a deeper understanding of nature of excitonic states of the vdW $\text{Mg}(\text{OH})_2/h$ -AlN heterostructure we also investigate the band decomposed charge densities and excitonic wave functions. In Fig. 9.7 (a), the interlayer-spacing-dependent band decomposed charge densities of the first and second lowest levels of the CB at Γ point are shown. The lowest and second lowest levels are labeled as $\text{CB-}\Gamma_1$ and $\text{CB-}\Gamma_2$, respectively. The changes in the charge densities of these two levels contain remarkable informations about the evolution of the electrons involved in the states \mathbf{I}_{bil} , \mathbf{II}_{bil} , and \mathbf{III}_{bil} .

Firstly, when the distance is 6.0 Å, the charge density shown in $\text{CB-}\Gamma_2$ part of the Fig. 9.7 (a) corresponds to the charge density at the CBM of individual $\text{Mg}(\text{OH})_2$. It is seen that this density appears mostly on O atoms and also at the surfaces of the $\text{Mg}(\text{OH})_2$. As the interlayer distance decreases, the charge density vanishes at the inner surface and increases at the outer surface. On the other hand, the density shown in the $\text{CB-}\Gamma_1$ for the interlayer distance of 6.0 Å corresponds to the charge density at the CBM of individual

h -AlN. As the distance decreases, charge changes negligibly at the vicinity of h -AlN but an additional charge density appears on inner O atom when the distance is less than 4.0 Å. It appears that when the layers approach each other, the inner surface electron of the Mg(OH)₂ is transferred to the h -AlN and the outer surface electron states of the Mg(OH)₂ remains at its original position.

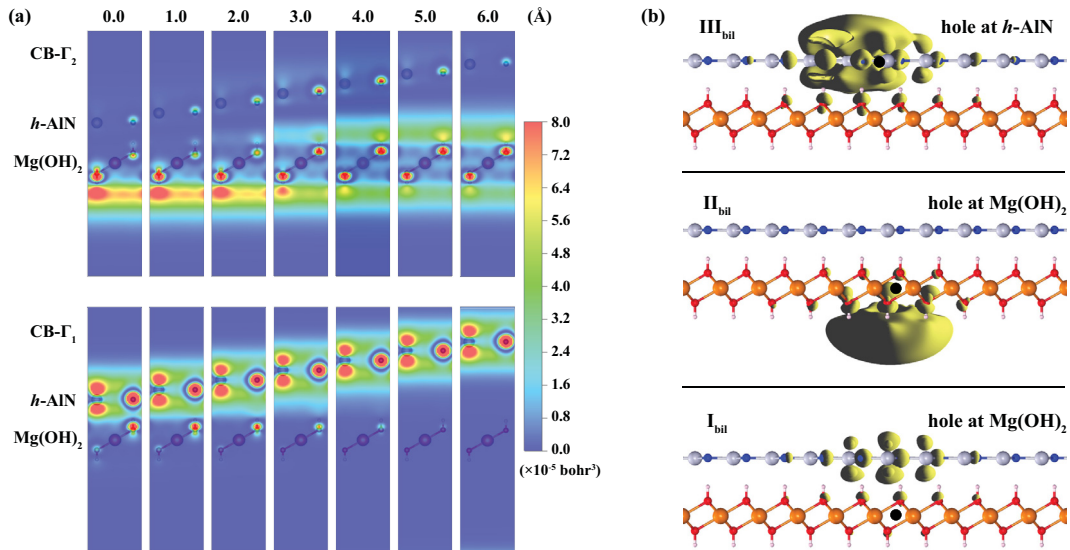


Figure 9.7. (a) Layer-layer distance dependent band decomposed charge densities at the Γ point for the lowest two bands ($\text{CB-}\Gamma_1$ and $\text{CB-}\Gamma_2$) are presented. The numbers on the upper part of the figure are distances between the layers in the unit of Å. The optimized layer-layer distance is set to 0.0 Å. (b) shows the wave function of the lowest three excitons which are labeled as I_{bil} , II_{bil} , and III_{bil} . The methodology for the determination of excitonic wave functions is given in part 9.1.2.

Furthermore, we also calculate the real space exciton localizations by using the methodology given in Appendix 9.1.2. The wave functions of the I_{bil} , II_{bil} , and III_{bil} are shown in Fig. 9.7 (b) where the yellow regions correspond to electrons and the black points stand for holes. As shown in the lower panel, it is evident that the I_{bil} is the spatially indirect exciton in which the electron and hole localize on the h -AlN and Mg(OH)₂, respectively. The II_{bil} localizes at the outer side of the Mg(OH)₂ as shown in middle panel of the Fig. 9.7 (b). It seems that the II_{bil} is not affected by the h -AlN. The III_{bil} shown in upper panel of the Fig. 9.7 (b) stays mostly on the h -AlN. A small portion of the III_{bil} appears on the hydroxide regions of the Mg(OH)₂.

9.4. Conclusions

In this study (Bacaksiz *et al.*, 2017), structural, electronic, and optical properties of the recently synthesized novel 2D materials of h -AlN and $\text{Mg}(\text{OH})_2$ and their bilayer heterostructure are investigated by performing DFT calculation. The excitonic states are also calculated by solving BSE over the GW_0 approximation on top of DFT. Our investigation revealed that: (i) the individual monolayer of the h -AlN and $\text{Mg}(\text{OH})_2$ can form a vertically stacked hetero-bilayer, (ii) when the hetero-bilayer formed, although the inter-layer interaction is weak novel exciton states appear, (iii) while h -AlN-states have weak spacing dependence, $\text{Mg}(\text{OH})_2$ states are strongly affected by the presence of a neighboring layer, (iv) exponential increase in screening of $\text{Mg}(\text{OH})_2$ on h -AlN-states was also predicted, (v) while the first exciton peak is a spatially indirect one, the second and third exciton states are spatially direct states.

Although the constituents have limited optical activity, the heterostructure shows unexpected optical properties. In particular, h -AlN- $\text{Mg}(\text{OH})_2$ hetero-bilayer exhibits spatially indirect excitons which is important for the optoelectronic application, especially based on photoexcited electron collecting.

CHAPTER 10

CONCLUSION

In the present thesis, an overview of light matter interaction including the specific issues of the two-dimensional materials such as changing in the dielectric environment and structural confinement effects was given. In addition, the basics of the density functional theory, GW approximation for the many-body effects and Bethe-Salpeter equation for the excitonic properties were also explained. The application of these theoretical methods were also given as several studies which were recently published as original scientific articles.

First of all, the structural and electronic properties of single-layer, bilayer, few-layer, and bulk form of h -AlN. The study revealed (Bacaksiz *et al.*, 2015) that as well as weak van der Waals (vdW) interactions, ionic character of the interlayer interactions plays an important role in the electronic properties of multilayered h -AlN. Therefore, while the number of layer is less than 10, h -AlN has an indirect band gap, otherwise it has direct band gap as the bulk form. In addition, upon dimensional reduction from bulk to bilayer energy the band gap decreases like as was found for h -BN and TMDs.

Secondly, we focused on structural and electronic properties of half- and fully-hydrogenated monolayers of PbI_2 (Bacaksiz and Sahin, 2016). We found that the T-phase is energetically more favorable than H-phase and it is an indirect semiconductor. This investigation revealed that the chemical functionalization by both half- and full-hydrogenation cause reconstruction in the structure of monolayer PbI_2 and lead to significant reduction in the band gap of the structure.

Third of all, the structural, electronic, and mechanical properties of the recently synthesized ultra-thin ZnSe were investigated. The investigation revealed that the monolayer ZnSe is dynamically stable and possesses angle dependent elastic parameters such as in-plane stiffness and Poisson ratio (Bacaksiz *et al.*, 2017).

In addition, as the fourth work, we concentrated on the monolayer and bilayer forms of hexagonal SnS_2 . It was found that from the calculated absorbance or reflectivity spectra, the optical signatures which allows one to characterize the structural phase or the stacking order of the SnS_2 layers were sought. We also investigate the effects of an applied perpendicular electric field, charging, and loading pressure on the characteristic properties of bilayer SnS_2 (Bacaksiz *et al.*, 2016).

Moreover, the layer and strain dependent optical properties of the recently h -AlN were investigated (Kecik *et al.*, 2015). The absorbance was found to increase when more layers were considered. The results also indicated that the absorption spectrum is globally redshifted under the applied strain. While the many-body corrections to the optical response calculations of h -AlN induced blueshifted spectra in general, evidence of bound excitons were also found for the layered structures of AlN.

Last of all, we investigated the excitonic properties of the hetero-bilayer of two perfectly-matching monolayers, h -AlN and $\text{Mg}(\text{OH})_2$ (Bacaksiz *et al.*, 2017). It was found that the vertically stacked heterostructure possesses excitonic peaks which appear only after the construction of the hetero-bilayer. More significantly, the wave function calculation showed that the first peak of the imaginary part of the dielectric function for the hetero-bilayer originates from spatially indirect exciton where the electron and hole localized at h -AlN and $\text{Mg}(\text{OH})_2$, respectively.

To summarize, due to different physical properties which are not observed in their bulk form, 2D material are center of attention more than a decade. In this respect, as we showed in our resent above mentioned works, the theoretical investigations are essential for elucidating physical insights of the observation, for fast and cheap characterization, and for also reliable prediction of possible ultra-thin materials. However, differing from the basic DFT method, the performing DFT-based optical property calculation and additional GW and BSE procedures need more rigorous study and also more computational resource resulting that the field is still in its early stage. Therefore, this thesis show that DFT and beyond-DFT are powerful methods for prediction of mechanical, electronic, and especially optical properties of 2D materials.

REFERENCES

- Adivarahan, V., W. H. Sun, A. Chitnis, M. Shatalov, S. Wu, H. P. Maruska, and M. A. Khan (2004). 250 nm algan light-emitting diodes. *Applied Physics Letters* 85(12), 2175–2177.
- Ahn, J.-H., M.-J. Lee, H. Heo, J. H. Sung, K. Kim, H. Hwang, and M.-H. Jo (2015). Deterministic two-dimensional polymorphism growth of hexagonal n-type SnS_2 and orthorhombic p-type SnS crystals. *Nano Letters* 15(6), 3703–3708.
- Aierken, Y., H. Sahin, F. Iyikanat, S. Horzum, A. Suslu, B. Chen, R. T. Senger, S. Tongay, and F. M. Peeters (2015, Jun). Portlandite crystal: Bulk, bilayer, and monolayer structures. *Phys. Rev. B* 91, 245413.
- Akasaki, I. and H. Amano (1997). Crystal growth and conductivity control of group iii nitride semiconductors and their application to short wavelength light emitters. *Japanese Journal of Applied Physics Part 1-Regular Papers Brief Communications & Review Papers* 36(9A), 5393–5408.
- Albrecht, S., L. Reining, R. Del Sole, and G. Onida (1998, May). Ab initio calculation of excitonic effects in the optical spectra of semiconductors. *Phys. Rev. Lett.* 80, 4510–4513.
- Alfè, D. (2009). Phon: A program to calculate phonons using the small displacement method. *Computer Physics Communications* 180(12), 2622 – 2633. 40 YEARS OF CPC: A celebratory issue focused on quality software for high performance, grid and novel computing architectures.
- Bacaksiz, C., S. Cahangirov, A. Rubio, R. T. Senger, F. M. Peeters, and H. Sahin (2016, Mar). Bilayer SnS_2 : Tunable stacking sequence by charging and loading pressure. *Phys. Rev. B* 93, 125403.
- Bacaksiz, C., A. Dominguez, A. Rubio, R. T. Senger, and H. Sahin (2017, Feb). $h\text{-AlN-Mg(OH)}_2$. *Phys. Rev. B* 95, 075423.
- Bacaksiz, C. and H. Sahin (2016). Single layer PbI_2 : hydrogenation-driven reconstructions. *RSC Advances* 6(92), 89708–89714.
- Bacaksiz, C., H. Sahin, H. D. Ozaydin, S. Horzum, R. T. Senger, and F. M. Peeters (2015, Feb). Hexagonal AlN : Dimensional-crossover-driven band-gap transition. *Phys. Rev. B* 91, 085430.
- Bacaksiz, C., R. Senger, and H. Sahin (2017). Ultra-thin ZnSe : Anisotropic and flexible crystal structure. *Applied Surface Science* 409, 426 – 430.

- Bader, R. and A. I. Molecules (1990). A quantum theory. *Clarendon: Oxford, UK*.
- Baskin, Y. and L. Meyer (1955, Oct). Lattice constants of graphite at low temperatures. *Phys. Rev.* 100, 544–544.
- Bechstedt, F., L. Matthes, P. Gori, and O. Pulci (2012). Infrared absorbance of silicene and germanene. *Applied Physics Letters* 100(26), 261906.
- Becke, A. D. (1988, Sep). Density-functional exchange-energy approximation with correct asymptotic behavior. *Phys. Rev. A* 38, 3098–3100.
- Bohm, D. and D. Pines (1951, Jun). A collective description of electron interactions. i. magnetic interactions. *Phys. Rev.* 82, 625–634.
- Born, M. and R. Oppenheimer (1927). Zur quantentheorie der molekeln. *Annalen der Physik* 389(20), 457–484.
- Bouchkour, Z., P. Tristant, E. Thune, C. Dublanche-Tixier, C. Jaoul, and R. Guinebretille (2011). Aluminum nitride nano-dots prepared by plasma enhanced chemical vapor deposition on si(111). *Surface and Coatings Technology* 205, S586 – S591. PSE 2010 Special Issue.
- Britnell, L., R. V. Gorbachev, R. Jalil, B. D. Belle, F. Schedin, A. Mishchenko, T. Georgiou, M. I. Katsnelson, L. Eaves, S. V. Morozov, N. M. R. Peres, J. Leist, A. K. Geim, K. S. Novoselov, and L. A. Ponomarenko (2012). Field-effect tunneling transistor based on vertical graphene heterostructures. *Science* 335(6071), 947–950.
- Bučko, Tomáš and Hafner, J., S. Lebègue, and J. G. Ángyán (2010). Improved description of the structure of molecular and layered crystals: Ab initio dft calculations with van der waals corrections. *The Journal of Physical Chemistry A* 114(43), 11814–11824. PMID: 20923175.
- Butler, S. Z., S. M. Hollen, L. Cao, Y. Cui, J. A. Gupta, H. R. Guti rrez, T. F. Heinz, S. S. Hong, J. Huang, A. F. Ismach, E. Johnston-Halperin, M. Kuno, V. V. Plashnitsa, R. D. Robinson, R. S. Ruoff, S. Salahuddin, J. Shan, L. Shi, M. G. Spencer, M. Terrones, W. Windl, and J. E. Goldberger (2013). Progress, challenges, and opportunities in two-dimensional materials beyond graphene. *ACS Nano* 7(4), 2898–2926. PMID: 23464873.
- Cabana, L., B. Ballesteros, E. Batista, C. Magen, R. Arenal, J. Oro-Sole, R. Rurali, and G. Tobias (2014). Synthesis of pbi 2 single-layered inorganic nanotubes encapsulated within carbon nanotubes. *Advanced Materials* 26(13), 2016–2021.
- Cabria, I., M. J. Lopez, and J. A. Alonso (2006). Density functional calculations of hydrogen adsorption on boron nanotubes and boron sheets. *Nanotechnology* 17(3), 778–785.

- Cahangirov, S., M. Topsakal, E. Aktürk, H. Şahin, and S. Ciraci (2009, Jun). Two- and one-dimensional honeycomb structures of silicon and germanium. *Phys. Rev. Lett.* 102, 236804.
- Çakır, D., H. Sahin, and F. m. c. M. Peeters (2014, Nov). Tuning of the electronic and optical properties of single-layer black phosphorus by strain. *Phys. Rev. B* 90, 205421.
- Cao, T., G. Wang, W. Han, H. Ye, C. Zhu, J. Shi, Q. Niu, P. Tan, E. Wang, B. Liu, and J. Feng (2012, Jun). Valley-selective circular dichroism of monolayer molybdenum disulphide. *Nature Communications* 3, 887 EP –. Article.
- Cao, X. K., B. Clubine, J. H. Edgar, J. Y. Lin, and H. X. Jiang (2013). Two-dimensional excitons in three-dimensional hexagonal boron nitride. *Applied Physics Letters* 103(19).
- Casiraghi, C., A. Hartschuh, E. Lidorikis, H. Qian, H. Harutyunyan, T. Gokus, K. S. Novoselov, and A. C. Ferrari (2007). Rayleigh imaging of graphene and graphene layers. *Nano Letters* 7(9), 2711–2717.
- Chao, J., Z. Xie, X. Duan, Y. Dong, Z. Wang, J. Xu, B. Liang, B. Shan, J. Ye, D. Chen, and G. Shen (2012). Visible-light-driven photocatalytic and photoelectrochemical properties of porous SnS_x ($x=1,2$) architectures. *Crystengcomm* 14(9), 3163–3168.
- Cheiwchanchamngij, T. and W. R. L. Lambrecht (2012, May). Quasiparticle band structure calculation of monolayer, bilayer, and bulk MoS_2 . *Phys. Rev. B* 85, 205302.
- Chen, P., Y. Su, H. Liu, and Y. Wang (2013). Interconnected tin disulfide nanosheets grown on graphene for lithium storage and photocatalytic applications. *Acs Applied Materials & Interfaces* 5(22), 12073–12082.
- Chen, Q., R. Song, C. Chen, and X. Chen (2013). Tunable band gap of AlN , GaN nanoribbons and AlN/GaN nanoribbon heterojunctions: A first-principle study. *Solid State Communications* 172, 24 – 28.
- Chen, X., F. Tian, C. Persson, W. Duan, and N.-x. Chen (2013). Interlayer interactions in graphites. *Scientific Reports* 3.
- Cheng, R., D. Li, H. Zhou, C. Wang, A. Yin, S. Jiang, Y. Liu, Y. Chen, Y. Huang, and X. Duan (2014). Electroluminescence and photocurrent generation from atomically sharp $\text{WSe}_2/\text{MoS}_2$ heterojunction p-n diodes. *Nano Letters* 14(10), 5590–5597. PMID: 25157588.
- Chernikov, A., T. C. Berkelbach, H. M. Hill, A. Rigosi, Y. Li, O. B. Aslan, D. R. Reichman, M. S. Hybertsen, and T. F. Heinz (2014, Aug). Exciton binding energy and nonhydrogenic rydberg series in monolayer WS_2 . *Phys. Rev. Lett.* 113, 076802.

- Chhowalla, M., H. S. Shin, G. Eda, L.-J. Li, K. P. Loh, and H. Zhang (2013). The chemistry of two-dimensional layered transition metal dichalcogenide nanosheets. *Nature chemistry* 5(4), 263–275.
- Choi, S., Z. Shaolin, and W. Yang (2014). Layer-number-dependent work function of mos₂ nanoflakes. *Journal of the Korean Physical Society* 64(10), 1550–1555.
- Christensen, N. E. and I. Gorczyca (1994, Aug). Optical and structural properties of iii-v nitrides under pressure. *Phys. Rev. B* 50, 4397–4415.
- Chung, D. D. L. (2002). Review graphite. *Journal of Materials Science* 37(8), 1475–1489.
- Coleman, J. N., M. Lotya, A. O’Neill, S. D. Bergin, P. J. King, U. Khan, K. Young, A. Gaucher, S. De, R. J. Smith, I. V. Shvets, S. K. Arora, G. Stanton, H.-Y. Kim, K. Lee, G. T. Kim, G. S. Duesberg, T. Hallam, J. J. Boland, J. J. Wang, J. F. Donegan, J. C. Grunlan, G. Moriarty, A. Shmeliov, R. J. Nicholls, J. M. Perkins, E. M. Grievson, K. Theuwissen, D. W. McComb, P. D. Nellist, and V. Nicolosi (2011). Two-dimensional nanosheets produced by liquid exfoliation of layered materials. *Science* 331(6017), 568–571.
- Cudazzo, P., L. Sponza, C. Giorgetti, L. Reining, F. Sottile, and M. Gatti (2016). Exciton band structure in two-dimensional materials. *Physical Review Letters* 116(6).
- Dàvila, M. E., L. Xian, S. Cahangirov, A. Rubio, and G. L. Lay (2014). Germanene: a novel two-dimensional germanium allotrope akin to graphene and silicene. *New Journal of Physics* 16(9), 095002.
- De, D., J. Manongdo, S. See, V. Zhang, A. Guloy, and H. Peng (2013). High on/off ratio field effect transistors based on exfoliated crystalline sns₂ nano-membranes. *Nanotechnology* 24(2).
- De Almeida, E., F. de Brito Mota, C. M. de Castilho, A. Kakanakova-Georgieva, and G. K. Gueorguiev (2012). Defects in hexagonal-aln sheets by first-principles calculations. *The European Physical Journal B-Condensed Matter and Complex Systems* 85(1), 1–9.
- de Almeida, E. F., F. de Brito Mota, C. M. C. de Castilho, A. Kakanakova-Georgieva, and G. K. Gueorguiev (2012). Defects in hexagonal-aln sheets by first-principles calculations. *The European Physical Journal B* 85(1), 48.
- Debbichi, L., O. Eriksson, and S. Lebègue (2014, May). Electronic structure of two-dimensional transition metal dichalcogenide bilayers from ab initio theory. *Phys. Rev. B* 89, 205311.
- Delawski, E. and B. A. Parkinson (1992). Layer-by-layer etching of 2-dimensional metal

- chalcogenides with the atomic force microscope. *Journal of the American Chemical Society* 114(5), 1661–1667.
- Deslippe, J., G. Samsonidze, D. A. Strubbe, M. Jain, M. L. Cohen, and S. G. Louie (2012). Berkeleygw: A massively parallel computer package for the calculation of the quasiparticle and optical properties of materials and nanostructures. *Computer Physics Communications* 183(6), 1269–1289.
- Ding, Y., G. T. Zhang, H. Wu, B. Hai, L. B. Wang, and Y. T. Qian (2001). Nanoscale magnesium hydroxide and magnesium oxide powders: Control over size, shape, and structure via hydrothermal synthesis. *Chemistry of Materials* 13(2), 435–440.
- Du, X.-J., Z. Chen, J. Zhang, C.-S. Yao, and C. Chen (2012). First-principles studies on stabilities and electronic properties of aln nanostructures. *Superlattices and Microstructures* 52(4), 662 – 668.
- Duan, J. H., S. G. Yang, H. W. Liu, J. F. Gong, H. B. Huang, X. N. Zhao, R. Zhang, and Y. W. Du (2005). Preparation and characterization of straight and zigzag aln nanowires. *The Journal of Physical Chemistry B* 109(9), 3701–3703. PMID: 16851410.
- Eda, G., H. Yamaguchi, D. Voiry, T. Fujita, M. Chen, and M. Chhowalla (2011). Photoluminescence from chemically exfoliated mos₂. *Nano Letters* 11(12), 5111–5116.
- Ehrenreich, H. and M. H. Cohen (1959, Aug). Self-consistent field approach to the many-electron problem. *Phys. Rev.* 115, 786–790.
- Elias, D. C., R. R. Nair, T. M. G. Mohiuddin, S. V. Morozov, P. Blake, M. P. Halsall, A. C. Ferrari, D. W. Boukhvalov, M. I. Katsnelson, A. K. Geim, and K. S. Novoselov (2009). Control of graphene's properties by reversible hydrogenation: Evidence for graphane. *Science* 323(5914), 610–613.
- Fakhrabad, D. V., N. Shahtahmasebi, and M. Ashhadi (2015). Optical excitations and quasiparticle energies in the mn monolayer honeycomb structure. *Superlattices and Microstructures* 79, 38–44.
- Fang, H., C. Battaglia, C. Carraro, S. Nemsak, B. Ozdol, J. S. Kang, H. A. Bechtel, S. B. Desai, F. Kronast, A. A. Unal, G. Conti, C. Conlon, G. K. Palsson, M. C. Martin, A. M. Minor, C. S. Fadley, E. Yablonovitch, R. Maboudian, and A. Javey (2014). Strong interlayer coupling in van der waals heterostructures built from single-layer chalcogenides. *Proceedings of the National Academy of Sciences of the United States of America* 111(17), 6198–6202.
- Farahani, M., T. S. Ahmadi, and A. Seif (2009). A dft study of the nuclear magnetic response of the zigzag aln-bn and bn-aln nanotube junctions. *Journal of Molecular Structure: THEOCHEM* 913(1), 126 – 130.

- Feng, L.-p., J. Su, and Z.-t. Liu (2014). Effect of vacancies on structural, electronic and optical properties of monolayer mos₂: A first-principles study. *Journal of Alloys and Compounds* 613, 122–127.
- Fermi, E. (1927). Un metodo statistico per la determinazione di alcune priorieta dell'atome. *Rend. Accad. Naz. Lincei* 6(602-607), 32.
- Ferrari, A. C., F. Bonaccorso, V. Fal'ko, K. S. Novoselov, S. Roche, P. Boggild, S. Borini, F. H. L. Koppens, V. Palermo, N. Pugno, J. A. Garrido, R. Sordan, A. Bianco, L. Ballerini, M. Prato, E. Lidorikis, J. Kivioja, C. Marinelli, T. Ryhaenen, A. Morpurgo, J. N. Coleman, V. Nicolosi, L. Colombo, A. Fert, M. Garcia-Hernandez, A. Bachtold, G. F. Schneider, F. Guinea, C. Dekker, M. Barbone, Z. Sun, C. Galiotis, A. N. Grigorenko, G. Konstantatos, A. Kis, M. Katsnelson, L. Vandersypen, A. Loiseau, V. Morandi, D. Neumaier, E. Treossi, V. Pellegrini, M. Polini, A. Tredicucci, G. M. Williams, B. H. Hong, J.-H. Ahn, J. M. Kim, H. Zirath, B. J. van Wees, H. van der Zant, L. Occhipinti, A. Di Matteo, I. A. Kinloch, T. Seyller, E. Quesnel, X. Feng, K. Teo, N. Rupesinghe, P. Hakonen, S. R. T. Neil, Q. Tannock, T. Loefwander, and J. Kinaret (2015). Science and technology roadmap for graphene, related two-dimensional crystals, and hybrid systems. *Nanoscale* 7(11), 4598–4810.
- Feynman, R. P. (1939, Aug). Forces in molecules. *Phys. Rev.* 56, 340–343.
- Flores, M. Z. S., P. A. S. Autreto, S. B. Legoas, and D. S. Galvao (2009). Graphene to graphane: a theoretical study. *Nanotechnology* 20(46).
- Fotouhi, B., A. Katty, and O. Gorochov (1985). Photoelectrochemical and corrosion study of n-type ssnse. *Journal of the Electrochemical Society* 132(9), 2181–2184.
- Fox, M. (2002). Optical properties of solids.
- Freeman, C. L., F. Claeysens, N. L. Allan, and J. H. Harding (2006a, Feb). Graphitic nanofilms as precursors to wurtzite films: Theory. *Phys. Rev. Lett.* 96, 066102.
- Freeman, C. L., F. Claeysens, N. L. Allan, and J. H. Harding (2006b). Graphitic nanofilms as precursors to wurtzite films: Theory. *Physical Review Letters* 96(6).
- Fuchs, F., J. Furthmüller, F. Bechstedt, M. Shishkin, and G. Kresse (2007, Sep). Quasi-particle band structure based on a generalized kohn-sham scheme. *Phys. Rev. B* 76, 115109.
- Furchi, M. M., A. Pospischil, F. Libisch, J. BurgdÄ¶rfer, and T. Mueller (2014). Photovoltaic effect in an electrically tunable van der waals heterojunction. *Nano Letters* 14(8), 4785–4791. PMID: 25057817.
- Gao, Y., W. Ren, T. Ma, Z. Liu, Y. Zhang, W.-B. Liu, L.-P. Ma, X. Ma, and H.-M. Cheng (2013). Repeated and controlled growth of monolayer, bilayer and few-layer

- hexagonal boron nitride on pt foils. *Acs Nano* 7(6), 5199–5206.
- Geim, A. K. and I. V. Grigorieva (2013). Van der waals heterostructures. *Nature* 499(7459), 419–425.
- Giannozzi, P., S. Baroni, N. Bonini, M. Calandra, R. Car, C. Cavazzoni, D. Ceresoli, G. L. Chiarotti, M. Cococcioni, I. Dabo, A. D. Corso, S. de Gironcoli, S. Fabris, G. Fratesi, R. Gebauer, U. Gerstmann, C. Gougoussis, A. Kokalj, M. Lazzeri, L. Martin-Samos, N. Marzari, F. Mauri, R. Mazzarello, S. Paolini, A. Pasquarello, L. Paulatto, C. Sbraccia, S. Scandolo, G. Sclauzero, A. P. Seitsonen, A. Smogunov, P. Umari, and R. M. Wentzcovitch (2009). Quantum espresso: a modular and open-source software project for quantum simulations of materials. *Journal of Physics: Condensed Matter* 21(39), 395502.
- Goh, W., G. Patriarche, P. Bonanno, S. Gautier, T. Moudakir, M. Abid, G. Orsal, A. Sirenko, Z.-H. Cai, A. Martinez, A. Ramdane, L. L. Gratiet, D. Troadec, A. Soltani, and A. Ougazzaden (2011). Structural and optical properties of nanodots, nanowires, and multi-quantum wells of iii-nitride grown by movpe nano-selective area growth. *Journal of Crystal Growth* 315(1), 160 – 163. 15th International Conference on Metalorganic Vapor Phase Epitaxy (ICMOVPE-XV).
- Gokus, T., R. R. Nair, A. Bonetti, M. Boehmler, A. Lombardo, K. S. Novoselov, A. K. Geim, A. C. Ferrari, and A. Hartschuh (2009). Making graphene luminescent by oxygen plasma treatment. *Acs Nano* 3(12), 3963–3968.
- Gong, Y., J. Lin, X. Wang, G. Shi, S. Lei, Z. Lin, X. Zou, G. Ye, R. Vajtai, B. I. Yakobson, H. Terrones, M. Terrones, B. Tay, J. Lou, S. T. Pantelides, Z. Liu, W. Zhou, and P. M. Ajayan (2014, Dec). Vertical and in-plane heterostructures from ws₂/mos₂ monolayers. *Nat Mater* 13(12), 1135–1142. Article.
- Gonze, X., B. Amadon, P.-M. Anglade, J.-M. Beuken, F. Bottin, P. Boulanger, F. Bruneval, D. Caliste, R. Caracas, M. Ct, T. Deutsch, L. Genovese, P. Ghosez, M. Giantomassi, S. Goedecker, D. Hamann, P. Hermet, F. Jollet, G. Jomard, S. Leroux, M. Mancini, S. Mazevet, M. Oliveira, G. Onida, Y. Pouillon, T. Rangel, G.-M. Rignanese, D. Sangalli, R. Shaltaf, M. Torrent, M. Verstraete, G. Zerah, and J. Zwanziger (2009). Abinit: First-principles approach to material and nanosystem properties. *Computer Physics Communications* 180(12), 2582 – 2615. 40 {YEARS} {OF} CPC: A celebratory issue focused on quality software for high performance, grid and novel computing architectures.
- Gordon, R. A., D. Yang, E. D. Crozier, D. T. Jiang, and R. F. Frindt (2002, Mar). Structures of exfoliated single layers of ws₂, mos₂, and mose₂ in aqueous suspension. *Phys. Rev. B* 65, 125407.
- Green, M. A., A. Ho-Baillie, and H. J. Snaith (2014). The emergence of perovskite solar cells. *Nature Photonics* 8(7), 506–514.

- Grimme, S. (2006). Semiempirical gga-type density functional constructed with a long-range dispersion correction. *Journal of Computational Chemistry* 27(15), 1787–1799.
- Guo, Y., K. Shoyama, W. Sato, Y. Matsuo, K. Inoue, K. Harano, C. Liu, H. Tanaka, and E. Nakamura (2015). Chemical pathways connecting lead(ii) iodide and perovskite via polymeric plumbate(ii) fiber. *Journal of the American Chemical Society* 137(50), 15907–15914.
- Gutiérrez, H. R., N. Perea-López, A. L. Elías, A. Berkdemir, B. Wang, R. Lv, F. López-Urías, V. H. Crespi, H. Terrones, and M. Terrones (2013). Extraordinary room-temperature photoluminescence in triangular ws₂ monolayers. *Nano Letters* 13(8), 3447–3454. PMID: 23194096.
- Guzmán-Verri, G. G. and L. C. Lew Yan Voon (2007, Aug). Electronic structure of silicon-based nanostructures. *Phys. Rev. B* 76, 075131.
- Han, J., M. H. Crawford, R. J. Shul, J. J. Figiel, M. Banas, L. Zhang, Y. K. Song, H. Zhou, and A. V. Nurmikko (1998). Algan/gan quantum well ultraviolet light emitting diodes. *Applied Physics Letters* 73(12), 1688–1690.
- Hanke, W. and L. J. Sham (1980). Many-particle effects in the optical-spectrum of a semiconductor. *Physical Review B* 21(10), 4656–4673.
- He, J., K. Hummer, and C. Franchini (2014). Stacking effects on the electronic and optical properties of bilayer transition metal dichalcogenides mos₂, mose₂, ws₂, and wse₂. *Physical Review B* 89(7).
- He, K., N. Kumar, L. Zhao, Z. Wang, K. F. Mak, H. Zhao, and J. Shan (2014, Jul). Tightly bound excitons in monolayer wse₂. *Phys. Rev. Lett.* 113, 026803.
- Hedin, L. (1965, Aug). New method for calculating the one-particle green's function with application to the electron-gas problem. *Phys. Rev.* 139, A796–A823.
- Hellmann, H. (1939). Einführung in die quantumchemie (leipzig: Franz deutsche 1937); r. p feynman. *Phys Rev* 56, 340.
- Henkelman, G., A. Arnaldsson, and H. Jónsson (2006). A fast and robust algorithm for bader decomposition of charge density. *Computational Materials Science* 36(3), 354 – 360.
- Heyd, J. and G. E. Scuseria (2004a). Assessment and validation of a screened coulomb hybrid density functional. *Journal of Chemical Physics* 120(16), 7274–7280.
- Heyd, J. and G. E. Scuseria (2004b). Efficient hybrid density functional calculations in solids: Assessment of the heyd-scuseria-ernzerhof screened coulomb hybrid functional. *Journal of Chemical Physics* 121(3), 1187–1192.

- Heyd, J., G. E. Scuseria, and M. Ernzerhof (2003). Hybrid functionals based on a screened coulomb potential. *The Journal of Chemical Physics* 118(18), 8207–8215.
- Hirayama, H. (2005). Quaternary inorganic-based high-efficiency ultraviolet light-emitting diodes. *Journal of Applied Physics* 97(9).
- Hohenberg, P. and W. Kohn (1964, Nov). Inhomogeneous electron gas. *Phys. Rev.* 136, B864–B871.
- Hong, X., J. Kim, S.-F. Shi, Y. Zhang, C. Jin, Y. Sun, S. Tongay, J. Wu, Y. Zhang, and F. Wang (2014). Ultrafast charge transfer in atomically thin mos₂/ws₂ heterostructures. *Nature Nanotechnology* 9(9), 682–686.
- Horzum, S., D. Çakır, J. Suh, S. Tongay, Y.-S. Huang, C.-H. Ho, J. Wu, H. Sahin, and F. M. Peeters (2014, Apr). Formation and stability of point defects in monolayer rhenium disulfide. *Phys. Rev. B* 89, 155433.
- Houssa, M., E. Scalise, K. Sankaran, G. Pourtois, V. V. Afanas'ev, and A. Stesmans (2011). Electronic properties of hydrogenated silicene and germanene. *Applied Physics Letters* 98(22).
- Huang, Y., E. Sutter, J. T. Sadowski, M. Cotlet, O. L. A. Monti, D. A. Rucke, M. R. Neupane, D. Wickramaratne, R. K. Lake, B. A. Parkinson, and P. Sutter (2014). Tin disulfide—an emerging layered metal dichalcogenide semiconductor: Materials properties and device characteristics. *Acs Nano* 8(10), 10743–10755.
- Huang, Z. X., Y. Wang, J. I. Wong, and H. Y. Yang (2015). Free standing sn₂ nanosheets on 3d graphene foam: an outstanding hybrid nanostructure anode for li-ion batteries. *2d Materials* 2(2).
- Hultman, L., S. Benhenda, G. Radnoczi, J. E. Sundgren, J. E. Greene, and I. Petrov (1992). Interfacial reactions in single-crystal-tin(100)/al/polycrystalline-tin multilayer thin-films. *Thin Solid Films* 215(2), 152–161.
- Hunt, B., J. D. Sanchez-Yamagishi, A. F. Young, M. Yankowitz, B. J. LeRoy, K. Watanabe, T. Taniguchi, P. Moon, M. Koshino, P. Jarillo-Herrero, and R. C. Ashoori (2013). Massive dirac fermions and hofstadter butterfly in a van der waals heterostructure. *Science* 340(6139), 1427–1430.
- Huo, N., J. Kang, Z. Wei, S.-S. Li, J. Li, and S.-H. Wei (2014). Novel and enhanced optoelectronic performances of multilayer mos₂-ws₂ heterostructure transistors. *Advanced Functional Materials* 24(44), 7025–7031.
- Hybertsen, M. S. and S. G. Louie (1986). Electron correlation in semiconductors and insulators - band-gaps and quasi-particle energies. *Physical Review B* 34(8), 5390–5413.

- Şahin, H., S. Cahangirov, M. Topsakal, E. Bekaroglu, E. Akturk, R. T. Senger, and S. Ciraci (2009, Oct). Monolayer honeycomb structures of group-iv elements and iii-v binary compounds: First-principles calculations. *Phys. Rev. B* 80, 155453.
- Ithurria, S., G. Bousquet, and B. Dubertret (2011). Continuous transition from 3d to 1d confinement observed during the formation of cdse nanoplatelets. *Journal of the American Chemical Society* 133(9), 3070–3077.
- Ithurria, S. and B. Dubertret (2008). Quasi 2d colloidal cdse platelets with thicknesses controlled at the atomic level. *Journal of the American Chemical Society* 130(49), 16504–+.
- Ithurria, S., M. D. Tessier, B. Mahler, R. P. S. M. Lobo, B. Dubertret, and A. L. Efros (2011). Colloidal nanoplatelets with two-dimensional electronic structure. *Nature Materials* 10(12), 936–941.
- Jeng, J.-Y., Y.-F. Chiang, M.-H. Lee, S.-R. Peng, T.-F. Guo, P. Chen, and T.-C. Wen (2013). Ch₃nh₃pb₃ perovskite/fullerene planar-heterojunction hybrid solar cells. *Advanced Materials* 25(27), 3727–3732.
- Jiang, Z., C. Wang, G. Du, Y. J. Zhong, and J. Z. Jiang (2012). In situ synthesis of sns₂@graphene nanocomposites for rechargeable lithium batteries. *Journal of Materials Chemistry* 22(19), 9494–9496.
- Jones, A. M., H. Yu, N. J. Ghimire, S. Wu, G. Aivazian, J. S. Ross, B. Zhao, J. Yan, D. G. Mandrus, D. Xiao, W. Yao, and X. Xu (2013, Sep). Optical generation of excitonic valley coherence in monolayer wse₂. *Nat Nano* 8(9), 634–638. Letter.
- Joshi, P. D., D. S. Joag, C. S. Rout, and D. J. Late (2015). Photosensitive field emission study of sns₂ nanosheets. *Journal of Vacuum Science & Technology B* 33(3).
- Kang, J., S. Tongay, J. Zhou, J. Li, and J. Wu (2013). Band offsets and heterostructures of two-dimensional semiconductors. *Applied Physics Letters* 102(1), 012111.
- Kara, A., H. Enriquez, A. P. Seitsonen, L. L. Y. Voon, S. Vizzini, B. Aufray, and H. Oughaddou (2012). A review on silicene-new candidate for electronics. *Surface science reports* 67(1), 1–18.
- Kecik, D., C. Bacaksiz, R. T. Senger, and E. Durgun (2015). Layer- and strain-dependent optoelectronic properties of hexagonal aln. *Physical Review B* 92(16).
- Khan, A., K. Balakrishnan, and T. Katona (2008). Ultraviolet light-emitting diodes based on group three nitrides. *Nature Photonics* 2(2), 77–84.
- Kim, K. K., A. Hsu, X. Jia, S. M. Kim, Y. Shi, M. Hofmann, D. Nezich, J. F. Rodriguez-Nieva, M. Dresselhaus, T. Palacios, and J. Kong (2012). Synthesis of monolayer

- hexagonal boron nitride on cu foil using chemical vapor deposition. *Nano Letters* 12(1), 161–166. PMID: 22111957.
- Kim, T.-J., C. Kirn, D. Son, M. Choi, and B. Park (2007). Novel sns₂-nanosheet anodes for lithium-ion batteries. *Journal of Power Sources* 167(2), 529–535.
- Kohn, W. and L. J. Sham (1965, Nov). Self-consistent equations including exchange and correlation effects. *Phys. Rev.* 140, A1133–A1138.
- Komsa, H.-P. and A. V. Krasheninnikov (2013, Aug). Electronic structures and optical properties of realistic transition metal dichalcogenide heterostructures from first principles. *Phys. Rev. B* 88, 085318.
- Kresse, G. and J. Furthmüller (1996a). Efficiency of ab-initio total energy calculations for metals and semiconductors using a plane-wave basis set. *Computational Materials Science* 6(1), 15 – 50.
- Kresse, G. and J. Furthmüller (1996b, Oct). Efficient iterative schemes for ab initio total-energy calculations using a plane-wave basis set. *Phys. Rev. B* 54, 11169–11186.
- Kresse, G. and J. Hafner (1993, Jan). Ab initio. *Phys. Rev. B* 47, 558–561.
- Kresse, G. and J. Hafner (1994, May). Ab initio. *Phys. Rev. B* 49, 14251–14269.
- Latini, S., T. Olsen, and K. S. Thygesen (2015, Dec). Excitons in van der waals heterostructures: The important role of dielectric screening. *Phys. Rev. B* 92, 245123.
- Lee, C.-H., G.-H. Lee, A. M. van der Zande, W. Chen, Y. Li, M. Han, X. Cui, G. Arefe, C. Nuckolls, T. F. Heinz, J. Guo, J. Hone, and P. Kim (2014, Sep). Atomically thin p-n junctions with van der waals heterointerfaces. *Nat Nano* 9, 676 – 681. Article.
- Lee, M. M., J. Teuscher, T. Miyasaka, T. N. Murakami, and H. J. Snaith (2012). Efficient hybrid solar cells based on meso-superstructured organometal halide perovskites. *Science* 338(6107), 643–647.
- Lei, F., Y. Sun, K. Liu, S. Gao, L. Liang, B. Pan, and Y. Xie (2014). Oxygen vacancies confined in ultrathin indium oxide porous sheets for promoted visible-light water splitting. *Journal of the American Chemical Society* 136(19), 6826–6829.
- Li, J., K. B. Nam, M. L. Nakarmi, J. Y. Lin, H. X. Jiang, P. Carrier, and S. H. Wei (2003). Band structure and fundamental optical transitions in wurtzite aln. *Applied Physics Letters* 83(25), 5163–5165.
- Li, L., P. Li, N. Lu, J. Dai, and X. C. Zeng (2015). Simulation evidence of hexagonal-to-tetragonal znse structure transition: A monolayer material with a wide-range tunable direct bandgap. *Advanced Science* 2(12).

- Li, Y., A. Chernikov, X. Zhang, A. Rigosi, H. M. Hill, A. M. van der Zande, D. A. Chenet, E.-M. Shih, J. Hone, and T. F. Heinz (2014, Nov). Measurement of the optical dielectric function of monolayer transition-metal dichalcogenides: MoS_2 , MoSe_2 , WS_2 , and WSe_2 . *Phys. Rev. B* 90, 205422.
- Li, Y., J. Xiang, F. Qian, S. Gradečak, Y. Wu, H. Yan, D. A. Blom, and C. M. Lieber (2006). Dopant-free gan/aln/algan radial nanowire heterostructures as high electron mobility transistors. *Nano Letters* 6(7), 1468–1473. PMID: 16834431.
- Li, Z. and X. Peng (2011). Size/shape-controlled synthesis of colloidal cdse quantum disks: Ligand and temperature effects. *Journal of the American Chemical Society* 133(17), 6578–6586.
- Liu, C.-C., H. Jiang, and Y. Yao (2011). Low-energy effective hamiltonian involving spin-orbit coupling in silicene and two-dimensional germanium and tin. *Physical Review B* 84(19).
- Liu, H., J. Gao, and J. Zhao (2013). Silicene on substrates: A way to preserve or tune its electronic properties. *The Journal of Physical Chemistry C* 117(20), 10353–10359.
- Liu, M., X. Yin, E. Ulin-Avila, B. Geng, T. Zentgraf, L. Ju, F. Wang, and X. Zhang (2011). A graphene-based broadband optical modulator. *Nature* 474(7349), 64–67.
- Liu, Z., J. Z. Liu, Y. Cheng, Z. Li, L. Wang, and Q. Zheng (2012). Interlayer binding energy of graphite: A mesoscopic determination from deformation. *Physical Review B* 85(20).
- Loughin, S., R. H. French, W. Y. Ching, Y. N. Xu, and G. A. Slack (1993). Electronic-structure of aluminum nitride - theory and experiment. *Applied Physics Letters* 63(9), 1182–1184.
- Ma, D., H. Zhou, J. Zhang, and Y. Qian (2008). Controlled synthesis and possible formation mechanism of leaf-shaped SnS_2 nanocrystals. *Materials Chemistry and Physics* 111(2-3), 391–395.
- Ma, J., D. Lei, L. Mei, X. Duan, Q. Li, T. Wang, and W. Zheng (2012). Plate-like SnS_2 nanostructures: Hydrothermal preparation, growth mechanism and excellent electrochemical properties. *Crystengcomm* 14(3), 832–836.
- Mak, K. F., K. He, J. Shan, and T. F. Heinz (2012). Control of valley polarization in monolayer MoS_2 by optical helicity. *Nature Nanotechnology* 7(8), 494–498.
- Mak, K. F., C. Lee, J. Hone, J. Shan, and T. F. Heinz (2010, Sep). Atomically thin MoS_2 : A new direct-gap semiconductor. *Phys. Rev. Lett.* 105, 136805.
- Mak, K. F., M. Y. Sfeir, Y. Wu, C. H. Lui, J. A. Misewich, and T. F. Heinz (2008, Nov).

- Measurement of the optical conductivity of graphene. *Phys. Rev. Lett.* *101*, 196405.
- Mak, K. F., J. Shan, and T. F. Heinz (2010). Electronic structure of few-layer graphene: Experimental demonstration of strong dependence on stacking sequence. *Physical Review Letters* *104*(17).
- Manna, L., D. J. Milliron, A. Meisel, E. C. Scher, and A. P. Alivisatos (2003). Controlled growth of tetrapod-branched inorganic nanocrystals. *Nature Materials* *2*(6), 382–385.
- Marini, A., P. García-González, and A. Rubio (2006, Apr). First-principles description of correlation effects in layered materials. *Phys. Rev. Lett.* *96*, 136404.
- Marini, A., C. Hogan, M. Gr \tilde{A} $\frac{1}{4}$ ning, and D. Varsano (2009). yambo: An ab initio tool for excited state calculations. *Computer Physics Communications* *180*(8), 1392 – 1403.
- Martin, R. M. (2004). *Electronic structure: basic theory and practical methods*. Cambridge university press.
- Matthes, L., P. Gori, O. Pulci, and F. Bechstedt (2013, Jan). Universal infrared absorbance of two-dimensional honeycomb group-iv crystals. *Phys. Rev. B* *87*, 035438.
- Miwa, K. and A. Fukumoto (1993, Sep). First-principles calculation of the structural, electronic, and vibrational properties of gallium nitride and aluminum nitride. *Phys. Rev. B* *48*, 7897–7902.
- Molina-Sánchez, A., D. Sangalli, K. Hummer, A. Marini, and L. Wirtz (2013, Jul). Effect of spin-orbit interaction on the optical spectra of single-layer, double-layer, and bulk mos₂. *Phys. Rev. B* *88*, 045412.
- Monkhorst, H. J. and J. D. Pack (1976). Special points for brillouin-zone integrations. *Physical Review B* *13*(12), 5188–5192.
- Morkoç, H., S. Strite, G. B. Gao, M. E. Lin, B. Sverdlov, and M. Burns (1994). Large-band-gap sic, iii-v nitride, and ii-vi znse-based semiconductor device technologies. *Journal of Applied Physics* *76*(3), 1363–1398.
- Murakami, T., T. Honjo, and T. Kuji (2011). Dos calculation analysis of new transparent conductor mg(oh)₂-c. *Materials Transactions* *52*(8), 1689–1692.
- Murray, C. B., D. J. Norris, and M. G. Bawendi (1993). Synthesis and characterization of nearly monodisperse cde (e = s, se, te) semiconductor nanocrystallites. *Journal of the American Chemical Society* *115*(19), 8706–8715.
- Nair, R. R., P. Blake, A. N. Grigorenko, K. S. Novoselov, T. J. Booth, T. Stauber, N. M. R. Peres, and A. K. Geim (2008). Fine structure constant defines visual transparency of graphene. *Science* *320*(5881), 1308–1308.

- Ni, Z., Q. Liu, K. Tang, J. Zheng, J. Zhou, R. Qin, Z. Gao, D. Yu, and J. Lu (2012). Tunable bandgap in silicene and germanene. *Nano Letters* 12(1), 113–118. PMID: 22050667.
- Nishida, T. and N. Kobayashi (1999). 346 nm emission from algalan multi-quantum-well light emitting diode. *Physica Status Solidi a-Applied Research* 176(1), 45–48.
- Novoselov, K., D. Jiang, F. Schedin, T. Booth, V. Khotkevich, S. Morozov, and A. Geim (2005). Two-dimensional atomic crystals. *Proceedings of the National Academy of Sciences of the United States of America* 102(30), 10451–10453.
- Novoselov, K. S., A. K. Geim, S. V. Morozov, D. Jiang, Y. Zhang, S. V. Dubonos, I. V. Grigorieva, and A. A. Firsov (2004). Electric field effect in atomically thin carbon films. *Science* 306(5696), 666–669.
- Onida, G., L. Reining, and A. Rubio (2002, Jun). Electronic excitations: density-functional versus many-body green's-function approaches. *Rev. Mod. Phys.* 74, 601–659.
- Ozcelik, V. O., E. Durgun, and S. Ciraci (2014). New phases of germanene. *Journal of Physical Chemistry Letters* 5(15), 2694–2699.
- Padilha, J. E., H. Peelaers, A. Janotti, and C. G. Van de Walle (2014). Nature and evolution of the band-edge states in mos2: From monolayer to bulk. *Physical Review B* 90(20).
- Paier, J., M. Marsman, K. Hummer, G. Kresse, I. C. Gerber, and J. G. Angyan (2006). Screened hybrid density functionals applied to solids. *Journal of Chemical Physics* 124(15).
- Palummo, M., M. Bernardi, and J. C. Grossman (2015). Exciton radiative lifetimes in two-dimensional transition metal dichalcogenides. *Nano Letters* 15(5), 2794–2800. PMID: 25798735.
- Pan, H. (2014). Electronic and magnetic properties of vanadium dichalcogenides monolayers tuned by hydrogenation. *Journal of Physical Chemistry C* 118(24), 13248–13253.
- Pan, T. S., D. De, J. Manongdo, A. M. Guloy, V. G. Hadjiev, Y. Lin, and H. B. Peng (2013). Field effect transistors with layered two-dimensional sns2-xsex conduction channels: Effects of selenium substitution. *Applied Physics Letters* 103(9).
- Panda, S. K., A. Antonakos, E. Liarokapis, S. Bhattacharya, and S. Chaudhuri (2007). Optical properties of nanocrystalline sns2 thin films. *Materials Research Bulletin* 42(3), 576–583.

- Park, H., H. Chung, and W. Kim (2013). Synthesis of ultrathin wurtzite znse nanosheets. *Materials Letters* 99, 172–175.
- Parkinson, B. (1990). Layer-by-layer nanometer scale etching of 2-dimensional substrates using the scanning tunneling microscope. *Journal of the American Chemical Society* 112(21), 7498–7502.
- Parkinson, B. A. (1988). Dye sensitization of vanderwaals surfaces of sns2 photoanodes. *Langmuir* 4(4), 967–976.
- Paszkowicz, W., J. Pelka, M. Knapp, T. Szyszko, and S. Podsiadlo (2002). Lattice parameters and anisotropic thermal expansion of hexagonal boron nitride in the 10–297.5Å k temperature range. *Applied Physics A* 75(3), 431–435.
- Peelaers, H. and C. G. Van de Walle (2012). Effects of strain on band structure and effective masses in mos2. *Physical Review B* 86(24).
- Peng, X. G., L. Manna, W. D. Yang, J. Wickham, E. Scher, A. Kadavanich, and A. P. Alivisatos (2000). Shape control of cdse nanocrystals. *Nature* 404(6773), 59–61.
- Perdew, J. P. and K. Burke (1996). Comparison shopping for a gradient-corrected density functional. *International journal of quantum chemistry* 57(3), 309–319.
- Perdew, J. P., K. Burke, and M. Ernzerhof (1996, Oct). Generalized gradient approximation made simple. *Phys. Rev. Lett.* 77, 3865–3868.
- Perdew, J. P., K. Burke, and M. Ernzerhof (1997). Generalized gradient approximation made simple [phys. rev. lett. 77, 3865 (1996)]. *Phys. Rev. Lett* 78(7), 1396.
- Perdew, J. P. and Y. Wang (1992, Jun). Accurate and simple analytic representation of the electron-gas correlation energy. *Phys. Rev. B* 45, 13244–13249.
- Pishtshev, A., S. Z. Karazhanov, and M. Klopov (2014). Excitons in mg(oh)(2) and ca(oh)(2) from ab initio calculations. *Solid State Communications* 193, 11–15.
- Ponce, F. A. and D. P. Bour (1997). Nitride-based semiconductors for blue and green light-emitting devices. *Nature* 386(6623), 351–359.
- Qiu, D. Y., F. H. da Jornada, and S. G. Louie (2013, Nov). Optical spectrum of mos₂: Many-body effects and diversity of exciton states. *Phys. Rev. Lett.* 111, 216805.
- Qu, B., C. Ma, G. Ji, C. Xu, J. Xu, Y. S. Meng, T. Wang, and J. Y. Lee (2014). Layered sns2-reduced graphene oxide composite - a high-capacity, high-rate, and long-cycle life sodium-ion battery anode material. *Advanced Materials* 26(23), 3854–3859.
- Ramasubramaniam, A. (2012, Sep). Large excitonic effects in monolayers of molybde-

num and tungsten dichalcogenides. *Phys. Rev. B* 86, 115409.

- Rivera, P., J. R. Schaibley, A. M. Jones, J. S. Ross, S. Wu, G. Aivazian, P. Klement, K. Seyler, G. Clark, N. J. Ghimire, J. Yan, D. G. Mandrus, W. Yao, and X. Xu (2015, Feb). Observation of long-lived interlayer excitons in monolayer mose2-wse2 heterostructures. *Nature Communications* 6, 6242 EP –. Article.
- Rohlfing, M. and S. G. Louie (1998, Sep). Electron-hole excitations in semiconductors and insulators. *Phys. Rev. Lett.* 81, 2312–2315.
- Rohlfing, M. and S. G. Louie (2000, Aug). Electron-hole excitations and optical spectra from first principles. *Phys. Rev. B* 62, 4927–4944.
- Ross, J. S., P. Klement, A. M. Jones, N. J. Ghimire, J. Yan, M. G., T. Taniguchi, K. Watanabe, K. Kitamura, W. Yao, D. H. Cobden, and X. Xu (2014, Apr). Electrically tunable excitonic light-emitting diodes based on monolayer wse2 p-n junctions. *Nat Nano* 9(4), 268–272. Letter.
- Rozzi, C. A., D. Varsano, A. Marini, E. K. U. Gross, and A. Rubio (2006, May). Exact coulomb cutoff technique for supercell calculations. *Phys. Rev. B* 73, 205119.
- Sahin, H., C. Ataca, and S. Ciraci (2010). Electronic and magnetic properties of graphane nanoribbons. *Physical Review B* 81(20).
- Sahin, H. and S. Ciraci (2011). Structural, mechanical, and electronic properties of defect-patterned graphene nanomeshes from first principles. *Physical Review B* 84(3).
- Sahin, H. and S. Ciraci (2012). Chlorine adsorption on graphene: Chlorographene. *Journal of Physical Chemistry C* 116(45), 24075–24083.
- Sahin, H., J. Sivek, S. Li, B. Partoens, and F. M. Peeters (2013, Jul). Stone-wales defects in silicene: Formation, stability, and reactivity of defect sites. *Phys. Rev. B* 88, 045434.
- Sahin, H., S. Tongay, S. Horzum, W. Fan, J. Zhou, J. Li, J. Wu, and F. M. Peeters (2013, Apr). Anomalous raman spectra and thickness-dependent electronic properties of wse₂. *Phys. Rev. B* 87, 165409.
- Salpeter, E. E. and H. A. Bethe (1951, Dec). A relativistic equation for bound-state problems. *Phys. Rev.* 84, 1232–1242.
- Schlaf, R., D. Louder, O. Lang, C. Pettenkofer, W. Jaegermann, K. W. Nebesny, P. A. Lee, B. A. Parkinson, and N. R. Armstrong (1995). Molecular-beam epitaxy growth of thin-films of sns2 and snse2 on cleaved mica and the basal planes of single-crystal layered semiconductors - reflection high-energy electron-diffraction, low-energy-electron diffraction, photoemission, and scanning-tunneling-microscopy atomic-force

- microscopy characterization. *Journal of Vacuum Science and Technology a-Vacuum Surfaces and Films* 13(3), 1761–1767.
- Seixas, L., A. S. Rodin, A. Carvalho, and A. H. Castro Neto (2015, Mar). Exciton binding energies and luminescence of phosphorene under pressure. *Phys. Rev. B* 91, 115437.
- Seo, J.-W., J.-t. Jang, S.-W. Park, C. Kim, B. Park, and J. Cheon (2008). Two-dimensional SnS_2 nanoplates with extraordinary high discharge capacity for lithium ion batteries. *Advanced Materials* 20(22), 4269–4273.
- Shi, C., H. Qin, Y. Zhang, J. Hu, and L. Ju (2014). Magnetic properties of transition metal doped aln nanosheet: First-principle studies. *Journal of Applied Physics* 115(5), 053907.
- Shi, H., H. Pan, Y.-W. Zhang, and B. I. Yakobson (2013a, Apr). Quasiparticle band structures and optical properties of strained monolayer MoS_2 and WS_2 . *Phys. Rev. B* 87, 155304.
- Shi, H., H. Pan, Y.-W. Zhang, and B. I. Yakobson (2013b). Strong ferromagnetism in hydrogenated monolayer MoS_2 tuned by strain. *Physical Review B* 88(20).
- Shi, Y., C. Hamsen, X. Jia, K. K. Kim, A. Reina, M. Hofmann, A. L. Hsu, K. Zhang, H. Li, Z.-Y. Juang, *et al.* (2010). Synthesis of few-layer hexagonal boron nitride thin film by chemical vapor deposition. *Nano letters* 10(10), 4134–4139.
- Shishkin, M. and G. Kresse (2006, Jul). Implementation and performance of the frequency-dependent *gw* method within the paw framework. *Phys. Rev. B* 74, 035101.
- Shishkin, M. and G. Kresse (2007, Jun). Self-consistent *gw* calculations for semiconductors and insulators. *Phys. Rev. B* 75, 235102.
- Shishkin, M., M. Marsman, and G. Kresse (2007, Dec). Accurate quasiparticle spectra from self-consistent *gw* calculations with vertex corrections. *Phys. Rev. Lett.* 99, 246403.
- Sideris, P. J., U. G. Nielsen, Z. Gan, and C. P. Grey (2008). Mg/al ordering in layered double hydroxides revealed by multinuclear nmr spectroscopy. *Science* 321(5885), 113–117.
- Silveira, E., J. A. F. Jr., M. Kneissl, D. W. Treat, N. M. Johnson, G. A. Slack, and L. J. Schowalter (2004). Near-bandedge cathodoluminescence of an aln homoepitaxial film. *Applied Physics Letters* 84(18), 3501–3503.
- Slack, G. A., R. A. Tanzilli, R. O. Pohl, and J. W. Vandersande (1987). The intrinsic thermal-conductivity of aln. *Journal of Physics and Chemistry of Solids* 48(7), 641–647.

- Sofo, J. O., A. S. Chaudhari, and G. D. Barber (2007). Graphane: A two-dimensional hydrocarbon. *Physical Review B* 75(15).
- Son, J. S., X.-D. Wen, J. Joo, J. Chae, S.-i. Baek, K. Park, J. H. Kim, K. An, J. H. Yu, S. G. Kwon, *et al.* (2009). Large-scale soft colloidal template synthesis of 1.4 nm thick cdse nanosheets. *Angewandte Chemie* 121(37), 6993–6996.
- Song, H. S., S. L. Li, L. Gao, Y. Xu, K. Ueno, J. Tang, Y. B. Cheng, and K. Tsukagoshi (2013). High-performance top-gated monolayer sns2 field-effect transistors and their integrated logic circuits. *Nanoscale* 5(20), 9666–9670.
- Song, X., J. Hu, and H. Zeng (2013). Two-dimensional semiconductors: recent progress and future perspectives. *Journal of Materials Chemistry C* 1(17), 2952–2969.
- Splendiani, A., L. Sun, Y. Zhang, T. Li, J. Kim, C.-Y. Chim, G. Galli, and F. Wang (2010). Emerging photoluminescence in monolayer mos2. *Nano Letters* 10(4), 1271–1275. PMID: 20229981.
- Srivastava, A., M. Sidler, A. V. Allain, D. S. Lembke, A. Kis, and A. Imamoglu (2015, Feb). Valley zeeman effect in elementary optical excitations of monolayer wse2. *Nat Phys* 11(2), 141–147. Letter.
- Su, G., V. G. Hadjiev, P. E. Loya, J. Zhang, S. Lei, S. Maharjan, P. Dong, P. M. Ajayan, J. Lou, and H. Peng (2015). Chemical vapor deposition of thin crystals of layered semiconductor sns2 for fast photodetection application. *Nano Letters* 15(1), 506–513.
- Sun, D., Z.-K. Wu, C. Divin, X. Li, C. Berger, W. A. de Heer, P. N. First, and T. B. Norris (2008, Oct). Ultrafast relaxation of excited dirac fermions in epitaxial graphene using optical differential transmission spectroscopy. *Phys. Rev. Lett.* 101, 157402.
- Sun, Y., H. Cheng, S. Gao, Z. Sun, Q. Liu, Q. Liu, F. Lei, T. Yao, J. He, S. Wei, and Y. Xie (2012). Freestanding tin disulfide single-layers realizing efficient visible-light water splitting. *Angewandte Chemie-International Edition* 51(35), 8727–8731.
- Sun, Y., Q. Liu, S. Gao, H. Cheng, F. Lei, Z. Sun, Y. Jiang, H. Su, S. Wei, and Y. Xie (2013). Pits confined in ultrathin cerium(iv) oxide for studying catalytic centers in carbon monoxide oxidation. *Nature Communications* 4.
- Sun, Y., Z. Sun, S. Gao, H. Cheng, Q. Liu, J. Piao, T. Yao, C. Wu, S. Hu, S. Wei, and Y. Xie (2012). Fabrication of flexible and freestanding zinc chalcogenide single layers. *Nature Communications* 3.
- Suslu, A., K. Wu, H. Sahin, B. Chen, S. Yang, H. Cai, T. Aoki, S. Horzum, J. Kang, F. M. Peeters, and S. Tongay (2016, Feb). Unusual dimensionality effects and surface charge density in 2d mg(oh)2. *Scientific Reports* 6, 20525 EP –. Article.

- Tan, C. and H. Zhang (2015). Two-dimensional transition metal dichalcogenide nanosheet-based composites. *Chemical Society Reviews* 44(9), 2713–2731.
- Tan, Z.-K., R. S. Moghaddam, M. L. Lai, P. Docampo, R. Higler, F. Deschler, M. Price, A. Sadhanala, L. M. Pazos, D. Credgington, F. Hanusch, T. Bein, H. J. Snaith, and R. H. Friend (2014). Bright light-emitting diodes based on organometal halide perovskite. *Nature Nanotechnology* 9(9), 687–692.
- Tang, Y., H. Cong, F. Li, and H.-M. Cheng (2007). Synthesis and photoluminescent property of aln nanobelt array. *Diamond and Related Materials* 16(3), 537 – 541.
- Thomas, L. H. (1927). The calculation of atomic fields. In *Mathematical Proceedings of the Cambridge Philosophical Society*, Volume 23, pp. 542–548. Cambridge Univ Press.
- Tong, C.-J., H. Zhang, Y.-N. Zhang, H. Liu, and L.-M. Liu (2014). New manifold two-dimensional single-layer structures of zinc-blende compounds. *Journal of Materials Chemistry A* 2(42), 17971–17978.
- Tongay, S., W. Fan, J. Kang, J. Park, U. Koldemir, J. Suh, D. S. Narang, K. Liu, J. Ji, J. Li, R. Sinclair, and J. Wu (2014). Tuning interlayer coupling in large-area heterostructures with cvd-grown mos₂ and ws₂ monolayers. *Nano Letters* 14(6), 3185–3190. PMID: 24845201.
- Tongay, S., H. Sahin, C. Ko, A. Luce, W. Fan, K. Liu, J. Zhou, Y.-S. Huang, C.-H. Ho, J. Yan, D. F. Ogletree, S. Aloni, J. Ji, S. Li, J. Li, F. M. Peeters, and J. Wu (2014, Feb). Monolayer behaviour in bulk res₂ due to electronic and vibrational decoupling. *Nature Communications* 5, 3252 EP –. Article.
- Tongay, S., J. Suh, C. Ataca, W. Fan, A. Luce, J. S. Kang, J. Liu, C. Ko, R. Raghunathanan, J. Zhou, F. Ogletree, J. Li, J. C. Grossman, and J. Wu (2013, Sep). Defects activated photoluminescence in two-dimensional semiconductors: interplay between bound, charged, and free excitons. *Scientific Reports* 3, 2657 EP –. Article.
- Tongay, S., J. Zhou, C. Ataca, K. Lo, T. S. Matthews, J. Li, J. C. Grossman, and J. Wu (2012). Thermally driven crossover from indirect toward direct bandgap in 2d semiconductors: Mose₂ versus mos₂. *Nano Letters* 12(11), 5576–5580. PMID: 23098085.
- Tonndorf, P., R. Schmidt, P. Böttger, X. Zhang, J. Börner, A. Liebig, M. Albrecht, C. Kloc, O. Gordan, D. R. T. Zahn, S. M. de Vasconcellos, and R. Bratschitsch (2013, Feb). Photoluminescence emission and raman response of monolayer mos₂, mose₂, and wse₂. *Opt. Express* 21(4), 4908–4916.
- Torun, E., H. Sahin, and F. M. Peeters (2016, Feb). Optical properties of gas-ca(oh)₂ bilayer heterostructure. *Phys. Rev. B* 93, 075111.

- Toulouse, A. S., B. P. Isaacoff, G. Shi, M. Matuchova, E. Kioupakis, and R. Merlin (2015). Frenkel-like-wannier-mott excitons in few-layer pbi₂. *Physical Review B* 91(16).
- Tsipas, P., S. Kassavetis, D. Tsoutsou, E. Xenogiannopoulou, E. Golias, S. Giamini, C. Grazianetti, D. Chiappe, A. Molle, M. Fanciulli, *et al.* (2013). Evidence for graphite-like hexagonal aln nanosheets epitaxially grown on single crystal ag (111). *Applied Physics Letters* 103(25), 251605.
- Tsukanov, A. A. and S. G. Psakhie (2016). Energy and structure of bonds in the interaction of organic anions with layered double hydroxide nanosheets: A molecular dynamics study. *Scientific Reports* 6.
- Ueno, M., A. Onodera, O. Shimomura, and K. Takemura (1992). X-ray-observation of the structural phase-transition of aluminum nitride under high-pressure. *Physical Review B* 45(17), 10123–10126.
- Ugeda, M. M., A. J. Bradley, S.-F. Shi, F. H. da Jornada, Y. Zhang, D. Y. Qiu, W. Ruan, S.-K. Mo, Z. Hussain, Z.-X. Shen, F. Wang, S. G. Louie, and M. F. Crommie (2014, Dec). Giant bandgap renormalization and excitonic effects in a monolayer transition metal dichalcogenide semiconductor. *Nat Mater* 13(12), 1091–1095. Letter.
- Utamapanya, S., K. J. Klabunde, and J. R. Schlup (1991). Nanoscale metal-oxide particles clusters as chemical reagents - synthesis and properties of ultrahigh surface-area magnesium-hydroxide and magnesium-oxide. *Chemistry of Materials* 3(1), 175–181.
- Virkar, A. V., T. B. Jackson, and R. A. Cutler (1989). Thermodynamic and kinetic effects of oxygen removal on the thermal-conductivity of aluminum nitride. *Journal of the American Ceramic Society* 72(11), 2031–2042.
- Voon, L. C. L. Y., E. Sandberg, R. S. Aga, and A. A. Farajian (2010). Hydrogen compounds of group-iv nanosheets. *Applied Physics Letters* 97(16).
- Vurgaftman, I., J. R. Meyer, and L. R. Ram-Mohan (2001). Band parameters for iii-v compound semiconductors and their alloys. *Journal of Applied Physics* 89(11), 5815–5875.
- Vy, T., R. Soklaski, Y. Liang, and L. Yang (2014). Layer-controlled band gap and anisotropic excitons in few-layer black phosphorus. *Physical Review B* 89(23).
- Wang, F., Y. Zhang, C. Tian, C. Girit, A. Zettl, M. Crommie, and Y. R. Shen (2008). Gate-variable optical transitions in graphene. *Science* 320(5873), 206–209.
- Wang, Q., Q. Sun, P. Jena, and Y. Kawazoe (2009). Potential of aln nanostructures as hydrogen storage materials. *ACS Nano* 3(3), 621–626. PMID: 19256516.

- Wang, Q. H., K. Kalantar-Zadeh, A. Kis, J. N. Coleman, and M. S. Strano (2012). Electronics and optoelectronics of two-dimensional transition metal dichalcogenides. *Nature nanotechnology* 7(11), 699.
- Wang, X.-Q., H.-D. Li, and J.-T. Wang (2012). Induced ferromagnetism in one-side semi-hydrogenated silicene and germanene. *Physical Chemistry Chemical Physics* 14(9), 3031–3036.
- Watanabe, K., T. Taniguchi, and H. Kanda (2004). Direct-bandgap properties and evidence for ultraviolet lasing of hexagonal boron nitride single crystal. *Nature Materials* 3(6), 404–409.
- Wei, R., J. Hu, T. Zhou, X. Zhou, J. Liu, and J. Li (2014). Ultrathin SnS_2 nanosheets with exposed 001 facets and enhanced photocatalytic properties. *Acta Materialia* 66, 163–171.
- Weimer, A. W., G. A. Cochran, G. A. Eisman, J. P. Henley, B. D. Hook, L. K. Mills, T. A. Guiton, A. K. Knudsen, N. R. Nicholas, J. E. Volmering, and W. G. Moore (1994). Rapid process for manufacturing aluminum nitride powder. *Journal of the American Ceramic Society* 77(1), 3–18.
- Wirtz, L., A. Marini, and A. Rubio (2006). Excitons in boron nitride nanotubes: Dimensionality effects. *Physical Review Letters* 96(12).
- Withers, F., O. Del Pozo-Zamudio, A. Mishchenko, A. P. Rooney, A. Gholinia, K. Watanabe, T. Taniguchi, S. J. Haigh, A. K. Geim, A. I. Tartakovskii, and K. S. Novoselov (2015, Mar). Light-emitting diodes by band-structure engineering in van der waals heterostructures. *Nat Mater* 14(3), 301–306. Letter.
- Wu, D., M. G. Lagally, and F. Liu (2011). Stabilizing graphitic thin films of wurtzite materials by epitaxial strain. *Physical Review Letters* 107(23).
- Wu, Q., Z. Hu, X. Wang, Y. Chen, and Y. Lu (2003). Synthesis and optical characterization of aluminum nitride nanobelts. *The Journal of Physical Chemistry B* 107(36), 9726–9729.
- Wu, Q., Z. Hu, X. Wang, Y. Hu, Y. Tian, and Y. Chen (2004). A simple route to aligned AlN nanowires. *Diamond and Related Materials* 13(1), 38 – 41.
- Xia, C., Y. Peng, H. Zhang, T. Wang, S. Wei, and Y. Jia (2014). The characteristics of n- and p-type dopants in SnS_2 monolayer nanosheets. *Physical Chemistry Chemical Physics* 16(36), 19674–19680.
- Xia, J., D. Zhu, L. Wang, B. Huang, X. Huang, and X.-M. Meng (2015). Large-scale growth of two-dimensional SnS_2 crystals driven by screw dislocations and application to photodetectors. *Advanced Functional Materials* 25(27), 4255–4261.

- Xia, Q., H. Xia, and A. L. Ruoff (1993). Pressure-induced rock-salt phase of aluminum nitride - a metastable structure at ambient condition. *Journal of Applied Physics* 73(12), 8198–8200.
- Yagmurcukardes, M., R. T. Senger, F. M. Peeters, and H. Sahin (2016). Mechanical properties of monolayer gas and gase crystals. *Physical Review B* 94(24).
- Yagmurcukardes, M., E. Torun, R. T. Senger, F. M. Peeters, and H. Sahin (2016). Mg(OH)₂-ws₂ van der Waals heterobilayer: Electric field tunable band-gap crossover. *Physical Review B* 94(19).
- Yang, K., S. Cahangirov, A. Cantarero, A. Rubio, and R. D'Agosta (2014, Mar). Thermoelectric properties of atomically thin silicene and germanene nanostructures. *Phys. Rev. B* 89, 125403.
- Yang, L., J. Deslippe, C.-H. Park, M. L. Cohen, and S. G. Louie (2009, Oct). Excitonic effects on the optical response of graphene and bilayer graphene. *Phys. Rev. Lett.* 103, 186802.
- Ye, Z., T. Cao, K. O'Brien, H. Zhu, X. Yin, Y. Wang, S. G. Louie, and X. Zhang (2014, Sep). Probing excitonic dark states in single-layer tungsten disulphide. *Nature* 513(7517), 214–218. Letter.
- Yeh, C.-Y., Z. W. Lu, S. Froyen, and A. Zunger (1992a, May). Predictions and systematizations of the zinc-blende-wurtzite structural energies in binary octet compounds. *Phys. Rev. B* 45, 12130–12133.
- Yeh, C.-Y., Z. W. Lu, S. Froyen, and A. Zunger (1992b, Oct). Zinc-blende-wurtzite polytypism in semiconductors. *Phys. Rev. B* 46, 10086–10097.
- Yin, Y. and A. P. Alivisatos (2005). Colloidal nanocrystal synthesis and the organic-inorganic interface. *Nature* 437(7059), 664–670.
- Yin, Z., H. Li, H. Li, L. Jiang, Y. Shi, Y. Sun, G. Lu, Q. Zhang, X. Chen, and H. Zhang (2012). Single-layer MoS₂ phototransistors. *ACS Nano* 6(1), 74–80. PMID: 22165908.
- Yoffe, A. D. (1993). Low-dimensional systems - quantum-size effects and electronic-properties of semiconductor microcrystallites (zero-dimensional systems) and some quasi-2-dimensional systems. *Advances in Physics* 42(2), 173–266.
- Yu, L., Y. Lv, X. Zhang, Y. Zhang, R. Zou, and F. Zhang (2011). Vapor-liquid-solid growth route to AlN nanowires on Au-coated Si substrate by direct nitridation of Al powder. *Journal of Crystal Growth* 334(1), 57 – 61.
- Yu, Y.-J., Y. Zhao, S. Ryu, L. E. Brus, K. S. Kim, and P. Kim (2009). Tuning the graphene

- work function by electric field effect. *Nano Letters* 9(10), 3430–3434.
- Zeng, H., J. Dai, W. Yao, D. Xiao, and X. Cui (2012, Aug). Valley polarization in mos₂ monolayers by optical pumping. *Nat Nano* 7(8), 490–493.
- Zhai, C., N. Du, H. Zhang, and D. Yang (2011). Large-scale synthesis of ultrathin hexagonal tin disulfide nanosheets with highly reversible lithium storage. *Chemical Communications* 47(4), 1270–1272.
- Zhang, X., Q. Liu, L. Meng, H. Wang, W. Bi, Y. Peng, T. Yao, S. Wei, and Y. Xie (2013). In-plane coassembly route to atomically thick inorganic-organic hybrid nanosheets. *Acs Nano* 7(2), 1682–1688.
- Zhang, X., J. Zhang, J. Zhao, B. Pan, M. Kong, J. Chen, and Y. Xie (2012). Half-metallic ferromagnetism in synthetic co₉se₈ nanosheets with atomic thickness. *Journal of the American Chemical Society* 134(29), 11908–11911.
- Zhao, Q., H. Zhang, X. Xu, Z. Wang, J. Xu, D. Yu, G. Li, F. Su, *et al.* (2005). Optical properties of highly ordered aln nanowire arrays grown on sapphire substrate. *Applied Physics Letters* 86(19), 193101–193101.
- Zheng, F.-L., J.-M. Zhang, Y. Zhang, and V. Ji (2010). First-principles study of the perfect and vacancy defect aln nanoribbon. *Physica B: Condensed Matter* 405(17), 3775 – 3781.
- Zhou, J., B. G. Sumpter, P. R. C. Kent, and J. Huang (2015). A novel and functional single-layer sheet of znse. *Acs Applied Materials & Interfaces* 7(3), 1458–1464.
- Zhou, J., M. M. Wu, X. Zhou, and Q. Sun (2009). Tuning electronic and magnetic properties of graphene by surface modification. *Applied Physics Letters* 95(10).
- Zhou, M., W. Duan, Y. Chen, and A. Du (2015). Single layer lead iodide: computational exploration of structural, electronic and optical properties, strain induced band modulation and the role of spin-orbital-coupling. *Nanoscale* 7(37), 15168–15174.
- Zhou, T., W. K. Pang, C. Zhang, J. Yang, Z. Chen, H. K. Liu, and Z. Guo (2014). Enhanced sodium-ion battery performance by structural phase transition from two-dimensional hexagonal-sns₂ to orthorhombic-sns. *Acs Nano* 8(8), 8323–8333.
- Zhuang, H. L. and R. G. Hennig (2012). Electronic structures of single-layer boron pnictides. *Applied Physics Letters* 101(15), 153109.
- Zhuang, H. L. and R. G. Hennig (2013). Theoretical perspective of photocatalytic properties of single-layer sns₂. *Physical Review B* 88(11).
- Zhuang, H. L., A. K. Singh, and R. G. Hennig (2013). Computational discovery of single-

layer iii-v materials. *Physical Review B* 87(16).

Zhuo, L., Y. Wu, L. Wang, Y. Yu, X. Zhang, and F. Zhao (2012). One-step hydrothermal synthesis of $\text{SnS}_2/\text{graphene}$ composites as anode material for highly efficient rechargeable lithium ion batteries. *Rsc Advances* 2(12), 5084–5087.

VITA

Date and Place of Birth: 05.03.1982, Balıkesir-TURKEY

EDUCATION

2011 - 2017 Doctor of Philosophy in Department of Physics

Graduate School of Engineering and Sciences, İzmir Institute of Technology,
İzmir -Turkey

Thesis Title: Optical Properties of Ultra-thin Materials

Supervisor: Prof. Dr. R. Tuğrul SENGER

2008 - 2011 Master of Science in Physics

Graduate School of Engineering and Sciences, İzmir Institute of Technology
İzmir -Turkey

Thesis Title: Excitonic Luminescence In Spherical Core-multi-shell Quantum Dot
Structures

Supervisor: Prof. Dr. R. Tuğrul SENGER

2003 - 2008 Bachelor of Physics

Department of Physics, Faculty of Science, İzmir Institute of Technology
İzmir - Turkey

SELECTED PUBLICATIONS

Bacaksiz, C., Sahin, H., Ozaydin, H. D., Horzum, S., Senger, R. T., and Peeters, F. M. (2015). "Hexagonal AlN: Dimensional-crossover-driven band-gap transition". Physical Review B, 91(8), 085430.

Bacaksiz, C., Cahangirov, S., Rubio, A., Senger, R. T., Peeters, F. M., and Sahin, H. (2016). "Bilayer SnS 2: Tunable stacking sequence by charging and loading pressure". Physical Review B, 93(12), 125403.

Bacaksiz, C., Dominguez, A., Rubio, A., Senger, R. T., and Sahin, H. (2017). "h-AlN-Mg (OH) 2 van der Waals bilayer heterostructure: Tuning the excitonic characteristics.". Physical Review B, 95(7), 075423.